

**A COMPUTATIONAL MODEL FOR TILTING PAD JOURNAL BEARINGS:  
ACCOUNTING FOR THERMALLY INDUCED PAD DEFORMATIONS AND  
IMPROVING A FEEDING GROOVE THERMAL MIXING MODEL**

A Thesis

by

**BEHZAD ABDOLLAHI**

Submitted to the Office of Graduate and Professional Studies of  
Texas A&M University  
in partial fulfillment of the requirements for the degree of

**MASTER OF SCIENCE**

Chair of Committee,	Luis San Andrés
Committee Members,	Dara Childs
	Theofanis Strouboulis
Head of Department,	Andreas A. Polycarpou

December 2017

Major Subject: Mechanical Engineering

Copyright 2017 Behzad Abdollahi

## ABSTRACT

Analysis of tilting pad journal bearings (TPJBs) has reached great complexity as 3D computational fluid dynamics models are coupled to finite element structural models for the pads, journal and bearing housing and account for fluid-solid interactions. The aim is to reach great levels of confidence (accuracy) in prediction of bearing performance without resorting to (expensive and time consuming) testing.

The thesis includes a thermo-elasto-hydrodynamic (TEHD) model that accounts for the pads structure mechanical deformation and includes pivot elastic displacements, both due to pressure and temperature changes. Note that in operation with a high shaft speed and/or under a heavy load, pad surface deformations due to both hydrodynamic pressure and thermally induced strains change the pad curvature and could increase its machined preload. These surface deformations affect the operating film thickness, thus influencing the bearing performance.

A theoretical analysis along with physically sound assumptions derives a simple equation for prediction of the thermally induced deformation as a function of the temperature difference between the inner and back surfaces, both circumferentially averaged. The simple equation delivers results in agreement with a FE structure model for a number of typical bearing pads.

This thesis also introduces a model for the mixing of flow and thermal energy at a feeding groove and sets the temperature of the lubricant entering a pad leading edge. Accurate knowledge of this temperature (and inlet oil viscosity) and the flow rate entering a pad largely determine the temperature rise along the pad lubricated surface as well as the shear drag power loss, and ultimately the load capacity.

The archival literature reveal the benefits and shortcomings of a commonly used hot oil carry over thermal mixing model. The novel thermal mixing model acts to deliver

improved temperature predictions in conditions that limit the conventional model applications. An important modification is the ability to impose the actual supply flow, specifically when the bearing is operating in an over-flooded or reduced flow condition. In addition, the flow balance in the new model accounts for the groove side leakage flow (discharging out of the bearing) and the churning (recirculating) oil in the grooves. An empirical groove efficiency parameter regulates the temperature of above-mentioned flows in an effort to represent direct and conventional lubricant feeding arrangements as well as end-seal configurations.

Predicted static and dynamic force performance of two TPJBs are compared against test data in Refs. [1–5]. The performance parameters include journal eccentricity, pad surface temperature rise, flow rates in a feeding groove, fluid film thickness, hydrodynamic film pressure, bearing complex dynamic stiffnesses, as well as bearing (synchronous) stiffnesses, damping, and virtual mass coefficients. Performance predictions with and without including the thermally induced deformation of the pads, and using either the novel or the conventional thermal mixing models, are shown to demonstrate the improvement.

## **DEDICATION**

*For my parents,*

*Bijan Abdollahi and Rafat Rangchi*

## **ACKNOWLEDGMENTS**

I wholeheartedly express my gratitude to Dr. Luis San Andrés for giving me the opportunity to work at the Turbomachinery Laboratory. His extensive knowledge and meticulous attention to details along with his supervision, guidance, and teaching have been invaluable during my time as his student and research assistant. My experience at the Turbomachinery Laboratory has definitely taught me priceless interpersonal and professional skills.

Furthermore, I thank Dr. Dara Childs for being an exceptional professor in rotordynamics as well as my committee member. I also thank Dr. Theofanis Strouboulis for serving in my committee. I sincerely appreciate my colleagues at the Turbomachinery Laboratory for their support and encouragement.

## **CONTRIBUTORS AND FUNDING SOURCES**

### **Contributors**

This work was supervised by a thesis committee consisting of Professor Luis San Andrés [advisor] and Professor Dara Childs of the Department of Mechanical Engineering and Professor Theofanis Strouboulis of the Department of Aerospace Engineering. All work for the thesis was completed independently by the student.

### **Funding Sources**

This work was made possible in part by Texas A&M University Turbomachinery Research Consortium (TRC) under Grant Numbers TRC-B&C-01-17 and TRC-B&C-04-16. Its contents are solely the responsibility of the authors and do not necessarily represent the official views of the Turbomachinery Research Consortium (TRC).

## NOMENCLATURE

$C_b$	Bearing radial clearance [m]
$C_p$	Pad radial clearance [m]
$C'_b$	Estimated hot bearing radial clearance [m]
$C'_p$	Estimated hot pad radial clearance [m]
$C_{xx}, C_{yy}$	Bearing direct damping coefficients in horizontal and vertical directions [N·s/m]
$C_{xy}, C_{yx}$	Bearing cross coupled damping coefficients [N·s/m]
$C_{gr}$	Groove mixing coefficient [-]
$c_p$	Lubricant specific heat [J/kg °K]
$D$	Shaft diameter [m]
$E$	Material elastic modulus [N/m <sup>2</sup> ]
$e$	Journal eccentricity [m]
$G$	Material shear modulus [N/m]
$h$	Heat transfer coefficient [W/m <sup>2</sup> °K]
$H_{(\theta,z)}$	Fluid film thickness [m]
$K_{xx}, K_{yy}$	Bearing direct stiffness coefficients [N/m]
$K_{xy}, K_{yx}$	Bearing cross coupled stiffness coefficients [N/m]
$L$	Bearing length [m]
$N$	Journal rotational speed [RPM], $N = \Omega\pi/30$
$n$	Number of the grooves, usually same as the number of the pads
$m$	Bearing preload [-], $m = 1 - C_b/C_p$
$p$	Hydrodynamic pressure of the film [Pa]
$Q$	Lubricant flow [LPM]
$R_b$	Bearing radius [m]
$R_{back}$	Pad outer surface radius [m], $R_{back} = R_s + t + C_p$

$R_h$	Housing inner radius [m]
$R_p$	Pad inner surface radius [m], $R_p = R_s + C_p$
$R_s$	Shaft outer radius [m]
$T$	Fluid film temperature (cross-film average) [°K]
$\bar{T}_{(r)}$	Circumferentially averaged temperature in a pad [°K]
$T_{ref}$	Reference (cold) temperature [°K]
$T'_{(r,\theta)}$	Temperature field in a pad as a function of radius and angle [°K]
$T_p$	Average pad inner surface temperature [°K]
$T_{back}$	Average pad back surface temperature [°K]
$T_{gr}$	Temperature of the churning lubricant in the groove [°K]
$T_{sump}$	Oil sump temperature [°K]
$T_{sup}$	Supply (inlet) oil temperature [°K]
$t$	Pad thickness [m]
$U, W$	Bulk flow velocities in circumferential and axial directions [m/s]
$u$	Pad thermal deformation along radial direction [m]
$v$	Pad thermal deformation along circumferential direction [m]
$W$	Static load [N]
$W/(LD)$	Specific load [Pa]
$\Delta R_h$	Housing thermal expansion [m]
$\Delta R_s$	Shaft thermal expansion [m]
$\Delta \bar{T}$	Circumferentially averaged temperature rise in a pad [°K]
$\beta_{piv}$	Pad tilt angle [rad]
$\eta_{piv}$	Pad transverse displacement [m]
$\xi_{piv}$	Pad radial displacement [m]
$\theta_{pad}$	Pad arc length [rad]



$\theta_{piv}$	Angle from pad pivot to pad leading edge [rad]
$\theta_p$	Pivot angular position starting from $-x$ axis [rad]
$\kappa_x, \kappa_z$	Bulk flow turbulence shear parameters $\kappa_x = \kappa_z = 12$ for laminar flow.
$\kappa_J$	Bulk flow turbulence shear parameters $\kappa_J = \frac{\kappa_x + \kappa_z}{2}$
$\Phi$	Thermal energy (heat) flow by means of fluid motion [W]
$\Phi'$	Heat transfer between fluid film and bounding solids [W/m <sup>2</sup> ]
$\psi$	Attitude Angle [deg]
$\Omega$	Shaft angular speed [rad/s]
$\omega$	Excitation frequency [rad/s]
$\sigma_r, \sigma_{\hat{\theta}}$	Normal strain in pad local coordinate [-]
$\tau_{r\hat{\theta}}$	Shear stress in pad local coordinate [-]
$\epsilon_r, \epsilon_{\hat{\theta}}$	Normal strain in pad local coordinate [-]
$\gamma_{r\hat{\theta}}$	Shear strain in pad local coordinate [-]
$\mu$	Lubricant viscosity [mPa·s]

## Subscripts

<i>back</i>	Pad back (outer) surface
<i>gr</i>	Feeding groove region
<i>h</i>	Housing
<i>LE</i>	Leading Edge
<i>piv</i>	Pivot
<i>RF</i>	Reverse Flow
<i>s</i>	Shaft
<i>sump</i>	Region enclosed by back of the pad and bearing housing
<i>SL</i>	Side leakage
<i>sup</i>	Supply (inlet) oil

*TE* Trailing Edge

### **Coordinate Systems**

$(x, y, z)$  Cartesian coordinates, origin at bearing center

$(r, \theta, z)$  Cylindrical coordinates, origin at bearing center

$(r, \hat{\theta})$  Pad local polar coordinates, origin at pivot location on pad inner surface

### **Abbreviations**

EHD Elastohydrodynamic

ID Inner Diameter

OD Outer Diameter

LBP Load between Pads

LOP Load on Pad

TPJB Tilting Pad Journal Bearing

TEHD Thermoelastohydrodynamic, includes pressure and thermally induced deformations

THD Thermohydrodynamic

RHS, LHS Right and left hand side

## TABLE OF CONTENTS

	Page
1 INTRODUCTION . . . . .	1
2 OBJECTIVE . . . . .	6
3 REVIEW OF PAST WORK . . . . .	8
3.1 Pressure and thermally induced pad deformations . . . . .	9
3.2 Lubricant mixing in a feed groove region . . . . .	14
3.3 Literature review closure . . . . .	20
4 DESCRIPTION OF THE PREDICTION MODEL . . . . .	22
4.1 Reynolds equation . . . . .	22
4.2 Bulk flow energy transport equation . . . . .	23
4.3 Temperature distribution in a pad . . . . .	25
4.4 Lubricant mixing at a feed groove . . . . .	28
4.5 Elastic pad thermally induced deformation . . . . .	39
4.6 Shaft expansion and housing expansion . . . . .	46
4.7 Hot clearance estimation . . . . .	47
5 COMPARISON OF PREDICTIONS AGAINST TEST DATA . . . . .	50
5.1 Large TPJB operating at a high surface speed and heavy load . . . . .	50
5.2 Spherical seat TPJB under heavy specific load and high speed . . . . .	65
6 CONCLUSION . . . . .	86
REFERENCES . . . . .	89
APPENDIX A THERMAL STRESSES . . . . .	95
APPENDIX B XLTPJB® GRAPHICAL USER INTERFACE . . . . .	99

## LIST OF FIGURES

FIGURE		Page
1	Schematic view of a 4 pad load between pad (LOP) tilting pad journal bearing components and coordinate system. . . . .	1
2	Thermally induced deformation of a shaft (journal) and a pad. . . . .	2
3	<i>a</i> : A lubricant feed groove region bounded by adjacent pads in a TPJB with a single orifice. <i>b</i> : Heat fluxes and lubricant flows across the boundaries of the groove region. . . . .	3
4	A heavily loaded TPJB operating with a high journal eccentricity. . . . .	5
5	Geometry of one tilting pad and nomenclature. . . . .	22
6	Heat fluxes ( $\Phi$ ) entering and leaving a bearing pad through its surfaces. . . . .	25
7	Thermal model accounting for the heat transfer between the film, pad and journal as well as heat transfer between the pad and surrounding lubricant. . . . .	26
8	Example of two dimensional temperature rise distribution in the pads and the mean film temperature of a TPJB operating at a shaft speed of 16,000 RPM and under a specific load of 2.9 MPa. (Temperature rise from an oil supply at 49 °C) . . . . .	28
9	<i>Left</i> : schematic view of a heavily loaded TPJB operating at a large journal eccentricity. <i>Right</i> : a hydraulic network that allocates the supply flow for each feed groove. . . . .	30
10	Predicted fractions of total supply flow ( $\alpha_i$ ) allocated to each groove for a 4 and a 5 pad TPJB with details in Tables 1 and 4. (Dashed red lines specify an even distribution at zero load) . . . . .	34
11	Mixing in a feed groove region of hot oil leaving an upstream pad ( $Q_{TE}^{i-1}$ ) with a cold supply flow ( $Q_{sup}^i$ ). Including side leakage flow ( $Q_{SL}^i$ ) and groove recirculating flow ( $Q_{gr}^i$ ) as well as heat transfer with the bounding pads ( $\Phi'_{TE}, \Phi'_{LE}$ ). . . . .	35

12	Groove control volume including fluid streams (solid arrows), and heat flows (hollow arrows). <i>Left</i> : heat flows from <i>hot</i> upstream oil ( $\Phi_{TE,SL}$ ) and the <i>cold</i> supply oil ( $\Phi_{sup,SL}$ ) to oil stream that discharges from the groove. <i>Right</i> : heat flows from <i>hot</i> upstream oil ( $\Phi_{TE,gr}$ ) and the <i>cold</i> supply oil ( $\Phi_{sup,gr}$ ) to the oil stream that recirculates within the groove. . . . .	37
13	Definition of a pad local coordinate system and deformations ( $u, v$ ) along radial and circumferential directions. . . . .	41
14	Definition of an assumed cantilevered beam to approximate pad warping along the axial direction. . . . .	45
15	Pad inner surface thermally induced deformation. Comparison of results from the current analytical method (right) versus 3D FEM (right). Reference geometry taken from Ref. [3] . . . . .	46
16	<i>Left</i> : Circumcenter of a pad, <i>Right</i> : Thermal deformation of a pad, includes the effects of thermal expansion and warping. . . . .	48
17	Schematic view of a five-pad TPJB in Ref. [1]. . . . .	52
18	Pads' surface temperature rise versus circumferential location. Predictions from current and old mixing models compared against test data in Ref. [1]. (Spray Bar, Flooded, $T_{sup}=50^{\circ}\text{C}$ , $N=3000$ RPM, $W/(LD)=2.5$ MPa, and $C_{gr}=0.2$ ) . . . . .	53
19	Pads' surface temperature rise versus circumferential location for two supply flow rates (210 L/min and 420 L/min). Predictions compared against test data in Ref. [1]. (Spray Bar, Flooded, $T_{sup}=50^{\circ}\text{C}$ , $N=3000$ RPM, $W/(LD)=1$ MPa, $C_{gr}=0.2$ ) . . . . .	55
20	Pads' surface temperature rise versus angle for operation at three shaft speeds. (Spray Bar, Flooded, $T_{sup}=50^{\circ}\text{C}$ , $N=1500, 3000, 4500$ RPM, $W/(LD)=2.5$ MPa, $C_{gr}=0.2$ , and $\lambda=0.8$ ) . . . . .	56
21	TEHD and THD predictions for mid-plane film pressure compared against test data in Ref. [1]. Star symbol (★) shows the location of minimum film thickness. ( $N=3000$ RPM, $W/(LD)=2.5$ MPa) . . . . .	57
22	Predicted pads' inner surface deformation along the radial direction. Positive magnitude denotes (outward) expansion, while negative magnitude denotes (inward) contraction. ( $N=3000$ RPM, $W/(LD)=2.5$ MPa) . . . . .	58

23	TEHD and THD predictions for mid-plane film thickness compared against test data in Ref. [1]. Star symbol (★) shows the location of peak pressure. ( $N=3000$ RPM, $W/(LD)=2.5$ MPa) . . . . .	59
24	Predicted and measured film pressure at the circumferential location of peak pressure ( $\theta=62^\circ$ , see Figure 21). TEHD and THD predictions compared against test data in Ref. [1]. ( $N=3000$ RPM, $W/(LD)=2.5$ ) . . . . .	60
25	Predicted and measured film thickness in the circumferential location of the minimum film thickness ( $\theta=74^\circ$ , see Figure 23). Measured results in Ref. [1]. ( $N=3000$ RPM, $W/(LD)=2.5$ MPa) . . . . .	61
26	Direct stiffness coefficients ( $K_{yy}$ , $K_{xx}$ ) versus specific load for operation at two shaft speeds. TEHD prediction and test data in Ref. [2]. (Synchronous excitation; <i>Left</i> : $N=1500$ RPM, <i>Right</i> : $N=3000$ RPM) . . . . .	63
27	Direct damping coefficients ( $C_{yy}$ , $C_{xx}$ ) for operation at two shaft speeds. Prediction and test data from Ref. [2]. (Synchronous excitation; <i>Left</i> : $N=1500$ RPM, <i>Right</i> : $N=3000$ RPM) . . . . .	64
28	Schematic view of a four-pad TPJB in Ref. [4] . . . . .	67
29	Pads' surface temperature rise versus circumferential location. Predictions compared against test data in Ref. [3]. (Spray Bar, Evacuated, $T_{sup}=49^\circ\text{C}$ , $N=7,000$ RPM, $W/(LD)=2.9, 2.1, 0.7$ MPa, and $C_{gr}=0.6$ ) . . . . .	68
30	Pads' surface temperature rise versus circumferential location. Predictions compared against test data in Ref. [3]. (Spray Bar, Evacuated, $T_{sup}=49^\circ\text{C}$ , $N=16,000$ RPM, $W/(LD)=2.9, 2.1, 0.7$ MPa, and $C_{gr}=0.6$ ) . . . . .	69
31	Maximum inner surface temperature on pad 2 versus shaft speed at operation with three specific loads. Current predictions and test data in Ref. [4]. ( $W/(LD)=2.9, 2.1, 0.7$ MPa, $C_{gr}=0.6$ ) . . . . .	71
32	Predicted flow rate versus shaft speed at operation with three specific loads. Constant flow rate in tests [4] for spray-bar with evacuated housing. ( $W/(LD)=2.9, 2.1, 0.7$ MPa) . . . . .	72
33	Pads' surface temperature rise versus circumferential location for three lubricant delivery methods. Predictions compared against test data in Ref. [3]. (SBB=Spray Bar Blocker, LEG=Leading Edge Groove, SO=Single Orifice, $T_{sup}=49^\circ\text{C}$ , $N=16,000$ RPM, $W/(LD)=2.9$ MPa) . . . . .	73

34	Journal eccentricities ( $-e_y, e_x$ ) versus rotor speed and operation with three specific loads. Predictions and test data in Ref. [4]. . . . .	75
35	Predicted hot clearance in $x, y$ coordinate system compared to test data in Ref. [4]. ( $W/(LD)=2.9$ MPa; <i>Left: <math>N=7000</math>, Right: <math>N=16000</math></i> ) . . . . .	76
36	Estimated hot bearing clearance versus rotor speed before a shutdown for the bearing in Ref. [4]. Predictions only include thermal deformations. ( $W/(LD)=2.9$ MPa) . . . . .	76
37	Predicted hot pad preload versus shaft speed for an operation under a specific load of 2.9 MPa . . . . .	77
38	Imaginary (left) and Real (right) parts of bearing complex dynamic stiffness versus excitation frequency for operation at three specific loads. TEHD and THD predictions compared to measurements in Ref. [5] for operation of $N=7000$ , and $W/(LD)=0.7, 2.1$ , and 2.9 MPa . . . . .	79
39	Imaginary (left) and Real (right) parts of bearing complex dynamic stiffness versus excitation frequency for operation at various specific loads. TEHD and THD predictions compared to measurements in Ref. [5] for operation of $N=16000$ , and $W/(LD)=0.7, 2.1$ , and 2.9 MPa . . . . .	80
40	Direct stiffness coefficients ( $K_{yy}, K_{xx}$ ) versus specific load for operation at four shaft speeds. TEHD and THD prediction and test data in Ref. [5] . . . . .	82
41	Direct damping coefficients ( $C_{yy}, C_{xx}$ ) versus specific load for operation at four shaft speeds. TEHD and THD prediction and test data in Ref. [5] . . . . .	84
42	Direct virtual mass coefficients ( $M_{yy}, M_{xx}$ ) versus specific load for operation at four shaft speeds. TEHD and THD prediction and test data in Ref. [5] . . . . .	85
43	Thermally induced stress along the circumferential and radial direction for a test pad in Ref. [4]. . . . .	97
44	Comparison of thermal strain with and without considering thermally induced stress along the circumferential and radial direction for a test pad in Ref. [4]. . . . .	98
45	Pad inner surface deformation along the radial direction versus pad local angle ( $\hat{\theta}$ ). Current method results compared to 2D FEM for a test pad in Ref. [4]. . . . .	98

46	XLTPJB® graphical user interface (GUI) parameter input form. . . . .	101
47	Schematic view of a 4 pad TPJB and description of its components. . . . .	102
48	Geometry and material characteristics of a pad with a liner. . . . .	106



## LIST OF TABLES

TABLE	Page
1	Characteristics of a test TPJB. From Hagemann et al. [1] . . . . . 51
2	Flow rates [L/min] in the feeding grooves of the bearing in Ref. [1]. Predictions from current model and simple (early) model. (Spray Bar, Flooded, $N=3000$ RPM, and $W/(LD)=2.5$ MPa, $\lambda=0.9$ , $C_{gr}=0.2$ ) . . . . . 53
3	TEHD and THD predictions for journal eccentricity in the load direction ( $-e_y$ ) for four specific loads. ( $N=3000$ RPM, $C_{gr}=0.2$ ) . . . . . 57
4	Characteristics of a TPJB tested by Coghlan and Childs [4] . . . . . 66
5	Flow rates [L/min] in the feeding grooves of the bearing in Ref. [3]. Predictions from current model and simple (early) model. (Spray Bar, Evacuated, $W/(LD)=0.7$ MPa, $N=7000$ RPM, $C_{gr}=0.6$ , $\lambda=0.8$ ) . . . . . 69
6	Flow rates [L/min] in the feeding grooves of the bearing in Ref. [3]. Predictions from current model and simple (early) model. (Spray Bar, Evacuated, $W/(LD)=2.9$ MPa, $N=16000$ RPM, $C_{gr}=0.6$ , $\lambda=0.8$ ) . . . . . 70
7	Recommended approximate range of groove efficiency parameter ( $C_{gr}$ ) for various lubrication methods. Symbol ★ marks the $C_{gr}$ magnitudes discussed in this thesis. . . . . 87

## 1 INTRODUCTION

A tilting pad journal bearing (TPJB) is a reliable type of fluid-film bearing for support of rotating machinery due to its minimal destabilizing forces and lower shear power loss when compared to a rigid surface bearing [6]. A TPJB, as shown in Figure 1, consists of usually three to six pads, each supported by a pivot. There is a thin lubricant film between the pads and the spinning journal. During operation, each pad tilts about its pivot and forms a convergent wedge between the pad inner surface and the shaft. The journal surface drags the viscous fluid film into the wedge to generate a hydrodynamic pressure field that enables the bearing to carry an applied load ( $W$ ).

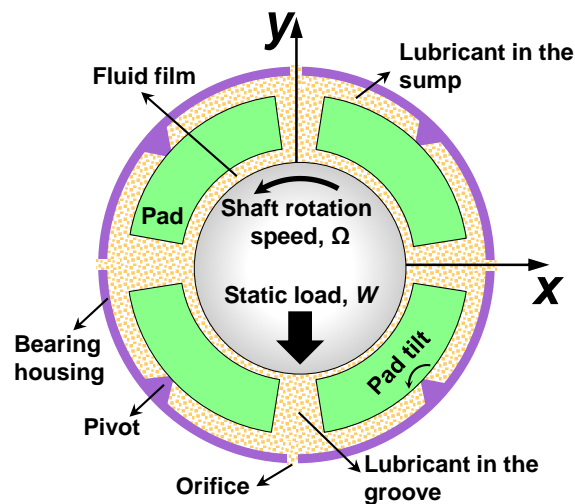


**Figure 1: Schematic view of a 4 pad load between pad (LOP) tilting pad journal bearing components and coordinate system.**

The load carrying capacity of a bearing depends on the fluid viscosity, which in itself is a strong function of the film temperature that increases due to the fluid shear drag power loss. The elastic deformation of the bearing elements (i.e. pads, shaft, and housing) due to both hydrodynamic pressure and temperature reshapes the operating film thickness,

particularly at a high speed operation<sup>1</sup> or under a heavy load<sup>2</sup>. The modified film thickness in turn alters the pressure and temperature fields in the film, and ultimately the dynamic force properties of the bearing (i.e., its stiffness and damping coefficients) [8, 9].

The temperature rise of the fluid film and the bounding solids during operation of a TPJB, as shown in Figure 2, deforms the bearing elements (i.e., shaft, pads, and housing). As described in Refs. [8–12], a fraction of the dissipated heat in the fluid film flows through the pad inner surface towards its back surface and also towards its sides which are surrounded by a cold lubricant. The radial temperature gradient stretches the pad inner surface more than its back surface and unwraps the thermally expanded pad. The change in the pad curvature, along with the variation in the shaft and housing diameters, typically increase the machined preload<sup>3</sup> of a TPJB [10–14].

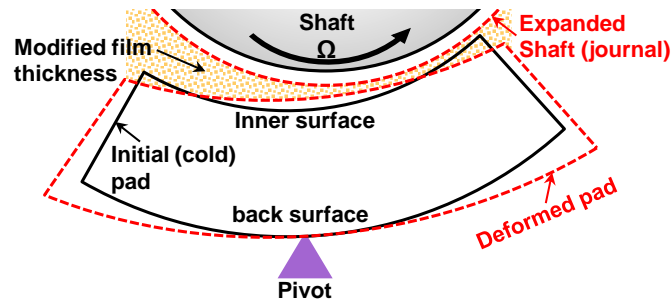


**Figure 2: Thermally induced deformation of a shaft (journal) and a pad.**

Figure 3 shows a conventional (single orifice<sup>4</sup>) feed groove in a TPJB. This region is comprised of an orifice supplying cold (fresh) lubricant at supply temperature ( $T_{sup}$ ) into the groove, an upstream pad discharging warm lubricant into the groove along with a layer

<sup>1</sup>Shaft surface speed =  $R_s\Omega$ , where  $R_s$  is the shaft radius and  $\Omega$  is the shaft angular speed. The recommended design limit is 91.5 m/s (300 ft/sec) [7].

<sup>2</sup>Specific (unit) load =  $W/(LD) > 2.1$  MPa (300 psi), where  $W$  is the static load,  $L$  and  $D$  are the length and the diameter of the bearing, respectively [7].

<sup>3</sup>The bearing preload ( $m$ ) is defined as  $m = (C_p - C_b)/C_p$ , where the pad clearance ( $C_p = R_p - R_s$ ) is the gap between pad and shaft radii, and the bearing clearance ( $C_b = R_b - R_s$ ) is the difference between both bearing and shaft radii.

<sup>4</sup>Note that modern high performance TPJBs utilize direct lubrication methods such as a spray bar, leading edge groove, or spray bar blocker.

of hot oil (at temperature  $T_{TE}$ ) attached to the journal surface, and a downstream pad that demands a certain amount of lubricant to fill its clearance. The flow within the groove is highly recirculating (churning).

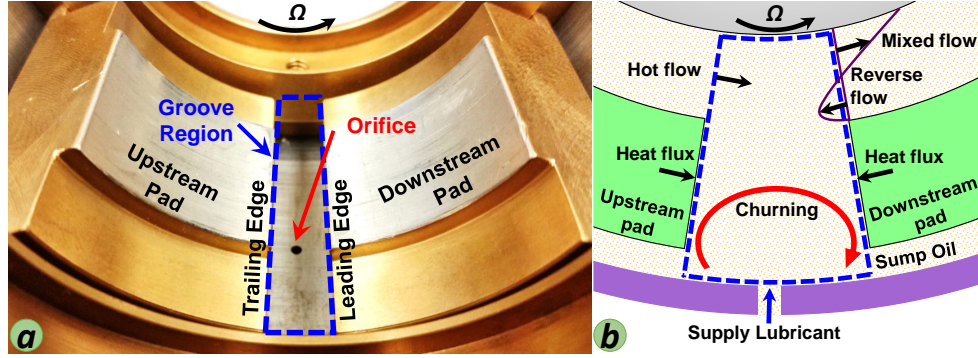


**Figure 3:** *a:* A lubricant feed groove region bounded by adjacent pads in a TPJB with a single orifice. *b:* Heat fluxes and lubricant flows across the boundaries of the groove region.

Mixing of hot and cold flows along with thermal energy exchanges in the lubricant feed groove region set both the temperature and flow rate of the fluid entering the leading edge of a downstream pad [15]. The flow rate and temperature of the fluid at a pad leading edge largely determine the film temperature rise along the lubricated pad surface and the temperature field within the pad, both of which ultimately govern the pad and journal thermally induced deformations.

In spite of the intricate nature of the flows in the feed groove region, various authors (Refs. [8, 16, 17]) developed simple yet physically sound models for the fluid mixing in this region. Bulk or lumped parameter thermal mixing models (adopted from Ref. [16]), apply the conservation of mass and thermal energy in the groove region through a *thermal mixing coefficient* or *hot oil carry over factor* ( $0 < \lambda < 1$ ).  $\lambda$  is the fraction of the trailing edge flow upstream of a groove that mixes with supply (cold) lubricant and reaches the downstream pad (see Eq. (1)). The temperature and flow rate balances determine the leading edge temperature ( $T_{LE}$ ) and flow rate ( $Q_{LE}$ ) as a weighted average of those from

the upstream pad trailing edge ( $Q_{TE}, T_{TE}$ ), and the (cold) supply flow ( $Q_{sup}, T_{sup}$ ) that is,

$$Q_{sup} = Q_{LE} - \lambda Q_{TE} \quad (1a)$$

$$T_{LE} Q_{LE} = Q_{sup} T_{sup} + (\lambda Q_{TE}) T_{LE} \quad (1b)$$

This simple concept, adapted by virtually all prediction tools, is not accurate for bearings operating under certain extreme conditions, see Ref. [18]. Some recent works [1, 18–20] report models for the fluid mixing in the feed groove region that diminish the influence of empirical coefficients. The following lists several physical phenomena within the groove region that are not accounted for by a simple thermal mixing flow model.

Figure 3-b shows the heat fluxes and fluid flows across the boundaries for a single orifice lubricant feed (conventional) supply. The cold supply flow mixes with the churning oil in the groove region before reaching the (upstream) hot oil layer attached to the spinning shaft. Meanwhile, the adjacent pads exchange heat with the oil in the groove via the bounding side walls. The fluid film entering a pad adds the shear drag flow (dragged by the spinning journal) to the pressure driven (reverse) flow. As the applied load increases the pressure driven flow becomes dominant causing a portion of the lubricant at the pad leading edge to flow in a reverse direction and to re-enter the groove. Finally, a portion of the flow exits the groove region axially (side leakage) depending on whether the bearing has end seals (flooded) or not (evacuated).

Figure 4 shows a load-between-pad (LBP) four pad TPJB operating under a heavy specific load ( $W/(LD) > 2.1$  MPa). A high journal eccentricity in the load direction creates a very thin film on the bottom pads while it unloads the upper ones, leaving a large gap between the unloaded pads (③, ④) and the shaft. The groove in between pads ④ and ① receives a large flow ( $Q_{TE}$ ) from the unloaded pad ④, while discharging only a much smaller flow ( $Q_{LE}$ ) to the heavily loaded pad ①. The simple thermal mixing model

(Eq. (1)) assumes that the supply flow ( $Q_{sup}$ ) always enters the groove; however in this condition, since ( $\lambda Q_{TE} > Q_{LE}$ ) the model sets the supply flow rate ( $Q_{sup}$ ) to zero. Ettles [8] defines boundaries for a ratio of upstream flow to downstream flow that prevents a negative supply flow. Suh and Palazzolo [13] also modify the early mixing model (Eq. (1)) to bypass the flow rate balance (Eq. (1a)) in this situation.

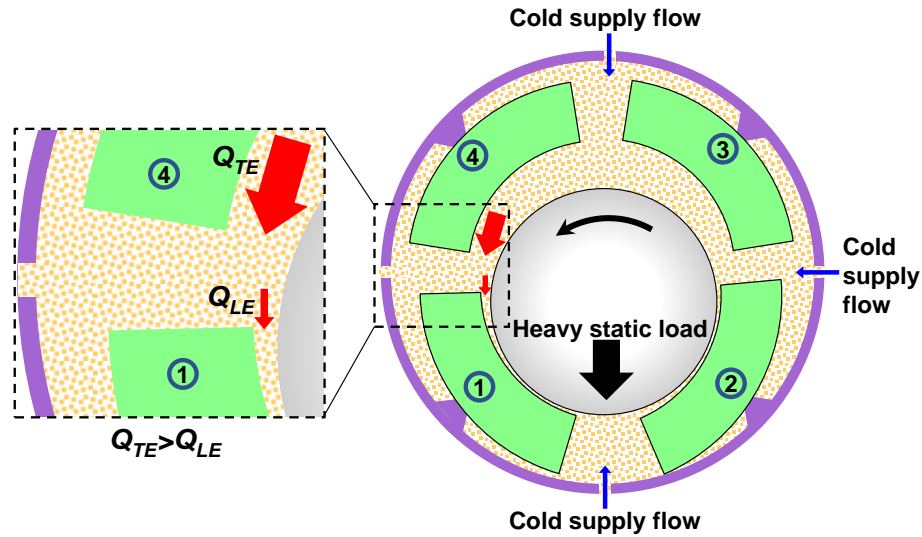


**Figure 4: A heavily loaded TPJB operating with a high journal eccentricity.**

Brito et al. [18] observe experimentally that in a two groove plain journal bearing hot oil flows out through one of the feed orifices (hot oil reflux) when the groove region is in the vicinity of the load direction. However, a similar phenomena (hot oil reflux) is not likely in TPJBs. Directly lubricated TPJBs operate with no end seals or wide open seals (evacuated housing) [21], and the excess upstream oil leaves the groove region axially (side leakage)[7]. For either a flooded or an evacuated bearing configuration, including the side leakage flow in the groove lubricant mixing model improves the temperature prediction (as in Ref. [20]).

## 2 OBJECTIVE

The objective of this work is to improve the prediction of TPJB flow and force performance while minimizing model complexity and computational time. The present thesis extends earlier analyses in Refs. [22–24] to couple the film pressure generation to the thermally induced deformation of the bearing elements (pads, shaft, and housing). This study also improves the lubricant thermal mixing model in a feed groove region.

The author performed the following tasks in a thermo-elasto-hydrodynamic (TEHD) analysis:

- Extend an existing predictive thermo-hydrodynamic (THD) bulk flow model, developed by San Andrés and Tao [22, 24], to account for the 2D temperature field in the bearing pads. The temperature in the solids (pads) is found by solving the governing (Laplace) equation with appropriate heat convection boundary conditions. A finite difference scheme is implemented for the solution.
- Analyze typical bearing pads subject to thermal gradients and use a commercial finite element (FE) software to calculate pad deformation fields. Subsequently, utilize theoretical analysis along with physically sound assumptions to deliver simple formulas for prediction of a thermally induced pad elastic deformation. The deformation is a function of the temperature difference across the pad, from the pad inner surface to its back surface, both circumferentially averaged. The proposed analytical method delivers results in agreement with the FE model for a number of practical cases.
- Modify the simple model for lubricant flow and thermal mixing in a supply groove region. The flow model accounts for the reverse flow and also side leakage flow. The lubricant thermal mixing model includes (1) heat flow due to inlet and outlet

lubricant flows in the groove region, (2) heat convection to the pads and bearing housing, and (3) the lubricant churning flow in the groove.

- Finally, the predictions for static load (i.e., distribution of pressure, temperature, and thickness in the fluid film, and journal eccentricity) and rotordynamic force coefficients are benchmarked against recent test data in Refs. [1–5]. The measurements refer to journal operation with a high surface speed (up to 85 m/s) and bearings supporting a heavy specific load (up to 2.9 MPa) which cause a significant mechanical deformation in the bearing elements. Note that Refs. [1–5] provide abundant test data for a wide range of operating conditions hence they are important to evaluate the novel thermal mixing model.



### 3 REVIEW OF PAST WORK

In 2013, San Andrés and Tao [22] develop a TPJB analysis and computational program (XLTPJB®) based on a thermohydrodynamic (THD) bulk flow model for fluid energy transport and hydrodynamic pressure field generation. The model accounts for a pad pivot stiffness and also temporal fluid inertia effects in the film. The program predicts bearing static performance parameters along with frequency reduced complex stiffness coefficients and frequency independent rotordynamic coefficients ( $[K, C, M]$  model). A parametric study for a 4 pad LBP TPJB with a diameter of 101.6 mm, operating with a shaft speed between 6 kRPM and 10 kRPM (surface speed of  $\Omega R_s = 53$  m/s), and under a specific load ( $W/(LD)$ ) up to 1.9 MPa shows that when the pivot is stiffer than the film, pivot flexibility has only a slight influence on the bearing force coefficients ( $[K, C, M]$ ). Nevertheless, a pivot that is equal or more flexible than the fluid film governs the bearing direct stiffnesses. Generally, including pivot flexibility in the model improves the predictions of dynamic force coefficient, in particular the damping coefficients.

Subsequently, San Andrés and Li [23] extend the above model to account for the pressure induced mechanical deformation on each bearing pad. A three dimensional finite element pad structural model couples to the film pressure generation. The hydrodynamic pressure field determines the pad deformation which modifies the film thickness. The predictions are compared to test data in Ref. [25] for a 3 pad LBP TPJB with a diameter of 101.6 mm and 3 pad thickness configurations, operating with a shaft speed between 6 kRPM and 12 kRPM ( $\Omega R_s = 64$  m/s), and under a specific load ( $W/(LD)$ ) between 0.2 MPa and 1.7 MPa. The comparisons show that the predicted static load parameters generally agree with the test data, except for the predicted maximum pressure and maximum temperature which are underestimated by up to 40%. Also, accounting for the pressure induced pad deformation reduces by up to 20% the predicted bearing stiffness and damp-

ing coefficients. However, the lower predicted stiffnesses agree less with the test data, in particular for the upper bound of shaft speed (12 kRPM).

The next sections scrutinize the influence of (a) pressure and thermally induced pad deformations and (b) the mixing of the lubricant in a feed groove on the prediction of TPJB static performance and rotordynamic coefficients.

### 3.1 Pressure and thermally induced pad deformations

Early works that study the influence of elastic deformations on TPJBs performance [8, 12, 26–28] model the pad as a 1D elastic beam subject to both a temperature gradient across the pad thickness and a hydrodynamic pressure distribution on its surface.

In 1980, Ettles [8] was among the first to include pad elastic deformations (using a beam model) in TPJB analysis. The author assumes that a large portion of the mechanical power loss is carried away by the flowing lubricant, while the rest is conducted through the pads (75%) and the journal (25%). This heat flow determines the temperature difference across the pad thickness that produces a thermally induced deformation. Predictions are compared to test data for a 4 pad LBP TPJB with a diameter of 119.85 mm, operating with a shaft speed up to 5kRPM (surface speed of  $\Omega R_s = 31$  m/s), and under a specific load between 30 kPa and 505 kPa. Accounting for pad elastic deformations improves the bearing damping predictions (reduces them) about 10% for  $W/(LD) = 30$  kPa and up to 40% for  $W/(LD) = 505$  kPa. However, predicted bearing stiffnesses only slightly improve (no more than 15%).

In 1992, Brockwell and Dmochowski [12] in a more detailed THD analysis adopt the beam model from Ref. [8] to investigate elastic deformation effects. The analysis accounts for cross-film viscosity variations and a 2D temperature field in a pad. The beam model accounts for bending moment, shear forces, and temperature gradient across the pad. Brockwell and Dmochowski verify their predictions against test data for a 5 pad T-

PJB with a shaft diameter of 0.076 m, operating with a shaft speed between 5 kRPM and 9 kRPM ( $\Omega R_s = 36$  m/s), and under a single specific load of 1.9 MPa. Accounting for the radial expansion of the bearing elements (shaft, pad, and housing) significantly improves (reduces) the eccentricity predictions. The elastic deformation in the above bearing is dominated by the thermal growth of the elements, amplified by an increase in shaft speed to reduce uniformly the film thickness on the loaded pads. On the other hand, for a large bearing with 500 mm diameter and relatively thin pads (25.4 mm thickness), pressure induced pad deformations prevail in the distorted pad shape. The authors define an ‘operational preload’ as a function of pad surface deformations and variations of shaft and housing diameter. An increase in shaft speed or the applied load raises the bearing operational preload.

In the early 1980’s, detailed numerical solutions were already employed to predict the temperature and pressure fields in a bearing. A group of researchers at the University of Poitiers [10, 11, 29–31] contributed remarkably to the advancement of 2D numerical models to account for pressure and thermally induced pad deformations in TPJB analysis.

In 1990, Fillon et al. [10] point out that even though a deformed pad surface alters the film thickness, the thermal expansion of the bearing elements has a more significant effect on the overall bearing performance through reducing the bearing clearance. The authors apply the thermohydrodynamic (THD) model in Refs. [29, 30] to TPJBs. In the model heat transfer field is considered 3D in the fluid film, 3D in the bearing, and 2D in the journal. The authors use FEM to couple the 2D mid-plane deformations of all the bearing components (i.e., pad, shaft, and housing) to the film thickness, thus making a thermoelastohydrodynamic (TEHD) analysis. Two years later (1992), Fillon et al. [11] measure temperatures of the pads, shaft, and housing in a 4 pad LPB TPJB with a diameter of 100 mm and two pad preload configurations (0.47 and 0.68), operating with a shaft speed up to 4 kRPM ( $\Omega R_s = 21$  m/s) and under a specific load up to 1.4 MPa. The thermally induced

pad deformation is 5 to 10 times greater than the pressure induced deformation. Including the deformations of the pad, shaft, and housing improves the predicted pad inner surface temperature up to 10 °C, reduces the minimum film thickness by 25%, and increases the maximum pressure about 35%. Fillon et al. suggest that an increase in the shaft speed is the principal parameter that reduces the bearing clearance. This reduction is up to 50% for a bearing with 0.68 pad preload and 25% for one with 0.47 pad preload.

A more complete analysis of thermally or pressure induced pad deformations requires the pad and pivot to be modeled as 3D FE structures to account for the pad axial deformations. Computationally optimized methods are required to expeditiously solve complex 3D temperature, pressure, and deformation fields. As in Refs. [1, 2, 9, 23, 24], coupling an efficient numerical software with the predictive code helps minimizing the process time.

In 1989, Brugier and Pascal [9] utilize a commercial structural FE software to investigate the 3D pressure and thermally induced pad deformations along with the pivot mechanical deformation. The authors implement the THD model in Ref. [29] to determine 3D thermal fields in the lubricant and within the pads and shaft. Axially-averaged deformations of the most heavily loaded pad(s) modify the film thickness. Brugier and Pascal predict static and dynamic force performance parameters for a 3 pad TPJB with a diameter of 0.75 m, operating with a shaft speed of 1500 RPM ( $\Omega R_s = 59$  m/s) and under a specific load between 1.2 MPa and 4.8 MPa. Including pressure induced pad deformations alone reduces the predicted film temperature, but accounting for thermally induced deformations rectifies the reduction. Compared to THD predictions, TEHD predictions lead to a smaller minimum film thickness, but only a slightly smaller maximum pad surface temperature. For specific loads between 1.2 MPa and 3.6 MPa the average pad deformation is about 14% to 38% of the machined pad clearance. Including the pad and shaft deformation reduces the bearing damping coefficients about 10% to 25%. The TEHD predictions for bearing stiffness coefficients are greater than THD ones for specific loads smaller than

1.9 MPa; after this threshold TEHD stiffnesses become lesser. The authors explain that at loads below 1.9 MPa the thermally induced deformation is dominant and reduces the bearing clearance. For loads higher than 1.9 MPa, however, the pressure induced deformation gains dominance and decreases the bearing stiffness due to pad unwrapping.

In 2013, Hagemann et al. [1] present a series of static load measurements conducted on a 5 pad LBP TPJB with a diameter of 0.5 m, subject to a high surface speed ( $\Omega R_s = 79$  m/s) and a specific load up to 2.5 MPa. The predictive model is based on a 2D Reynolds equation and a 3D temperature field in the fluid film and within the solids. The computational program is coupled with a commercial structural mechanics software in which the pressure and temperature fields elastically deform the pad structure. The authors heed the pad axial arching effects as the previous measurements in Ref. [32] render it critical to calculating an accurate film thickness (instead of axially averaging the pad deformation as in Ref. [9]). Pad axial arching increases the film thickness at the pad edges relative to its mid-plane by up to 25% of the machined pad clearance. Hydrodynamic pressure is accountable for about 40% of the pad axial arching while the rest is caused by thermally induced deformation. Predicted distributions of pressure, temperature, and thickness of the film correlate well with their test data. In spite of an accurate static load prediction, the (synchronous speed) predicted direct stiffnesses are up to 70% and direct damping coefficients up to 40% smaller than the measured ones [2].

Hagemann et al. [1] then compare static load test data versus versus circumferential location to the predictions from the 3D pad deformation model as well as a simple 1D pad deformation model (similar to Refs. [8, 12]). For the bearing above (diameter of 0.5 m), accounting for 3D pad elastic deformation improves the agreement with the test data by  $\sim 50\%$  as per minimum film thickness,  $\sim 27\%$  for maximum pressure, and up to  $20^\circ\text{C}$  (increase) for maximum pad surface temperature. However, the predictions from the two models do not show significant differences for a small size bearing (diameter

of 0.12 m) operating with a surface speed of 75 m/s and under a specific load between 1 MPa to 2.5 MPa. The authors recommend that the design, size, and the operating condition of the bearing determine the choice of an analysis, either simple or complex.

In 2015, Suh and Palazzolo [13] develop a TEHD model that accounts for the 3D temperature field in the fluid film, shaft, and pads along with pressure and thermally induced 3D deformations in both the shaft and bearing pads. Suh and Palazzolo [14] compare predictions to test data from Ref. [33] for a 5 pad TPJB with a diameter of 100 mm, operating with a surface speed between 37 m/s to 85 m/s and under a specific load up to 2.4 MPa. The TEHD model over predicts (synchronous speed) direct stiffness coefficients (within 20%) and under predicts direct damping coefficient (within 30%).

Suh and Palazzolo [14] then compare TEHD and EHD predictions to analyze the thermal effects in TPJBs. The predicted (synchronous speed) bearing direct stiffnesses from the TEHD model are about two times larger than those from the EHD models. The authors attribute this difference to a tighter clearance caused by the thermal expansion of both the shaft and pads, even though the lubricant viscosity drops significantly. The shaft thermal expansion is more than twice the average pad expansion, albeit the pads are hotter. Note that Suh and Palazzolo's model does not account for the bearing housing expansion which, if free to expand outward, can partially negate the expansion of both shaft and the pads. Furthermore, the journal eccentricity and average film thickness from the TEHD analysis are lower than corresponding obtained magnitudes from the EHD analysis. Finally, the authors conduct a pad thickness parametric study for the above bearing and observe that regardless of pad thickness both mechanical and thermal deformations act to increase the pad preload. With a thick pad (18.5 mm), the preload increases predominantly due to thermally induced deformations. With a thin pad (7.4 mm), however, the increase is primarily due to the unwrapping induced by the acting hydrodynamic pressure.

### 3.2 Lubricant mixing in a feed groove region

The majority of methods that evaluate the film temperature at the leading edge of a pad (downstream of a groove) adopt an approximate balance of the thermal energy. In spite of complexity of the flow in a lubricant feed groove region, simplified models arose for arc journal bearings [15] and thrust bearings [34], and were later extended to TPJBs [8]. In addition, modern high performance TPJBs use direct lubrication methods that further make a difference between TPJB feed grooves from plain journal bearings feed grooves. Nevertheless, the various approaches to modeling the fluid mixing at a feeding groove in plain journal bearings helps with understanding this phenomena in TPJBs.

In 1967, Ettles [15] is among the first to develop a THD model for a laminar flow mixing at a rectangular feeding groove. A two-dimensional Navier-Stokes equation determines the temperature and pressure distribution in the groove. The predictions for a typical 40 mm<sup>2</sup> square groove show that the amount of oil that churns in the groove is 30 to 50 times the amount of oil that enters the groove from the upstream film. About 85% of the hot oil adheres to the shaft and travels across the groove to the next (downstream) bearing pad surface. The author notes that the cooling effect of a groove is not significantly dependent on the groove size or the downstream flow Reynolds number<sup>5</sup> (for  $1 < Re < 50$ ). While calculating an accurate heat transfer coefficient for laminar flow in the groove is challenging, in a turbulent flow regime the heat transfer is likely to increase and surface friction might also become appreciable. However, the author suggests that the hot oil carry over would not change significantly for a turbulent flow because of the laminar sublayer attached to the shaft.

More than a decade later, Ettles [8] notes the poor correlation of predictions from hot oil carry over theory [34] and test data for TPJBs, and introduces a groove mixing theory.

---

<sup>5</sup> $Re = (\rho v L) / \mu$ , where  $(\rho, \mu)$  are the lubricant material density and viscosity,  $v$  is the fluid velocity, and  $L$  is a characteristic linear dimension.

The theory assumes the make up flow between the trailing edge and the leading edge of the downstream pad is at supply temperature ( $T_{sup}$ ). This model does not require a mixing coefficient ( $\lambda = 1$  in Eq. (1)). However, the ratio of trailing edge flow to leading edge flow ( $\frac{Q_{TE}}{Q_{LE}}$ ) must remain between 0.1 and 0.9 since for heavily loaded pads it is likely that the upstream flow is larger than the leading edge flow.

In 1983, Mitsu et al. [16] investigate experimentally the effect of oil flow rate on fluid mixing at a feed groove in a plain journal bearing and introduce the mixing model in Eq. (1). The authors vary the supply pressure between 20 kPa and 180 kPa (to change to supply flow rate) for an operation with constant shaft speed of 1750 RPM ( $\Omega R_s = 9$  m/s) and specific load of 0.5 MPa. Mitsu et al. introduce an empirical coefficient ( $\lambda$ ) for the mixing of the lubricant flow with the supply flow prior to reaching the pad inlet. The measurements show that  $\lambda$  is inversely proportional to the supply flow rate and it lessens for an over-flooded condition ( $\lambda \sim 0.3$ ). The authors conclude that a  $\lambda$  between 0.4 and 0.8 provides film temperature predictions that are closely aligned with the test data among various flow rates.

In 1986, Heshmat and Pinkus [17] define a function for the thermal mixing coefficient ( $\lambda$ ) using the measured flow and temperature magnitudes in the feed groove of a plain journal bearing. The authors use a transparent bushing to observe the groove flow with a journal diameter of 138.1 mm, operating with a shaft speed of 1800 RPM ( $\Omega R_s = 14$  m/s) and under a specific load of 690 kPa. Most of the flow in the oil groove is highly recirculating (churning) and has little effect on the fluid flow (and therefore heat flow) that enters the groove from the upstream pad or discharges to the downstream pad. Hence, mixing of hot flow and cold flow is limited to a control volume with dimensions of the same order as a thin film attached to the journal. The measured mixing coefficient ( $\lambda$ ) is mainly dependent on surface speed and supply temperature, without a significant dependency on bearing load or type of the oil. Heshmat and Pinkus define a quadratic function for  $\lambda$  using



three empirical constants based on the test data. The function provides  $\lambda$  for a range of operating conditions, but is only appropriate within a limited (measured) range of supply oil temperature and journal surface speed .

In 2012, He et al. [21] investigate the applicability of the model in Ref. [16] (Eq. (1)) to directly lubricated bearings in a TEHD analysis. In industrial practice,  $0.7 < \lambda < 1$  for conventional flooded bearings, and  $0.3 < \lambda < 0.7$  for directly lubricated and evacuated bearings. The authors set a lower limit for a pad leading edge temperature from Eq. (1) defined by a cool oil insertion model in which (contrary to Eq. (1a)),  $Q_{sup}$  is known and determines the trailing edge flow ( $Q_{TE}$ ), and there is no mixing coefficient,

$$T_{LE}Q_{LE} = (Q_{LE} - Q_{sup})T_{LE} + Q_{sup}T_{sup} \quad (2)$$

where the supply flow ( $Q_{sup}$ ) for each groove is set as the measured total supply flow rate divided by the number of grooves. The above equation represents a situation where all the available supply oil cools the minimum amount of hot oil in the most efficient way. The authors then compare TEHD predictions to test data for three directly lubricated bearings (spray bar and leading edge groove). The test bearings have a common diameter of 0.1016 m, operating with a shaft speed ranging from 4 kRPM to 16 kRPM ( $\Omega R_s = 85$  m/s) and under a specific load between 0.35 MPa and 3.1 MPa. The TEHD predictions are consistent with test data, but the discrepancy becomes more pronounced as the bearing load increases. The discrepancy for peak pad surface temperature of the loaded pads reaches a maximum of 10 °C (at  $W/(LD) = 3.1$  MPa). Whereas the shaft speed shows little influence on the discrepancy. The mixing coefficient ( $\lambda$ ) is primarily a function of shaft speed and it decreases with an increase in journal speed. The authors believe the reduction of  $\lambda$  at a high speed is caused by more cold oil entering the pad, more hot oil pushed into the groove due to high centrifugal force, and an enhanced heat transfer in the groove region

due to high fluid velocity. The predicted temperatures for the first unloaded pad downstream of the loaded pads is substantially higher than the test data which casts doubt on the accuracy of assuming an evenly distributed supply oil in the grooves (Eq. (2)). He et al. conclude that the overall pad surface temperature error is mainly caused by the simplified (2D) pad elastic deformations and neglecting both shaft and housing thermal expansions.

In a similar way, Suh and Palazzolo [13] in 2015 modify Eq. (1) and only use a mixing coefficient when the upstream flow is larger than the a portion ( $\lambda = 0.8$ ) of downstream flow (to prevent a zero or negative supply flow). In this case, the temperature at the leading edge is calculated as a weighted average of trailing edge temperature and the lubricant supply temperature,

$$T_{LE} = \lambda T_{TE} + (1 - \lambda) T_{sup} \quad \text{when} \quad \lambda Q_{LE} < Q_{TE} \quad (3)$$

In 2014, Brito et al. [18] introduce a control volume to balance fluid flows and heat fluxes at the groove region for a plain journal bearing that includes: (1) Heat fluxes due to lubricant flow such as supply oil, upstream hot oil, downstream reverse flow (due to high pressure gradient), upstream back flow (due to cavitation); (2) convective heat transfer between the lubricant in the groove and the bounding solids (3); the groove length effect; (4) non-uniform temperature profile at the downstream inlet. Brito et al. observe experimentally a condition in which lubricant exits from one of the grooves (hot oil reflux). The authors introduce an alternative model for a groove that lacks any cold supply lubricant flowing in. In addition to another situation where the hot oil reflux from one of the grooves mixes with the cold oil in the feeding tubes, increasing the overall supply temperature on all the inlet orifices.

Bruto et al. [18] then compare their test data to predictions for a two groove (180° apart) plain journal bearing with a diameter of 50 mm, operating with a shaft speed of 4

kRPM ( $\Omega R_s = 11$  m/s). The test data show an appreciable negative flow rate in one of the grooves (up to 75% of the flow supplied to the other groove) for a range of specific load between 0.2 MPa and 4 MPa. The hot oil reflux occurs even for low specific loads (0.1 MPa) when the applied load angle is such that a feed groove is in the vicinity of a region with high hydrodynamic pressure. In this case the local hydrodynamic pressure overcomes the supply pressure and the hot oil flows out. However in the experimental work, increasing the supply pressure alleviates the issue.

In 2016, Rindi et al. [20] determine a single pressure for the feed groove based on the upstream, downstream, side leakage, and supply flows. The authors do not assume the side leakage flow and supply flow as a fraction of the upstream flow (common practice). Instead, they employ an approximate method suggested by Nicholas [35] to find the two flows as a function of groove, supply, and ambient pressures. This method still requires the cross section area for the flow and an empirical coefficient to calculate the side leakage flow and supply flow. The authors compare the predictions with test data for a 4 pad LBP TPJB with a shaft diameter of 200 mm, operating at a shaft speed of 3800 RPM ( $\Omega R_s = 40$  m/s) and under a specific load of 1.6 MPa. The predicted groove pressure, supply flow rate, and groove temperature have less than 4% discrepancy with the test data.

Some works, such as Refs. [36–40], investigate the fluid mixing in a feeding groove via computational fluid dynamic (CFD) methods. Although computationally expensive, the CFD analysis of a groove region sheds light on the complex fluid mixing phenomena and has the potential to liberate the current models from using empirical coefficients.

In 2004, Kosasih and Tieu [36] use a commercial CFD approach and experimental observations to study the lubricant flow field in plain journal bearing grooves with various geometries and supply conditions. The analysis accounts for flow inertial effects and turbulence, but neglects the convection with the bounding solids. A Particle Image Velocimetry (PIV) system captures the velocity field in the groove region for a plain journal

bearing with a diameter of 80 mm and variable clearances of 0.1, 0.3, and 0.7 mm, operating with a shaft speed of 1800 RPM ( $\Omega R_s = 7.5$  m/s) and a supply flow rate of 1 L/min. The CFD predictions with a  $k - \omega$  turbulent model best predict the location of the recirculation zone. The streamlines show a portion of hot oil that adheres to the journal and is carried over to the downstream pad, and most of the cold oil in the groove recirculates without mixing with the hot oil. In fact, a large portion of supply (cold) oil does not immediately enter the lubricant film. The authors conclude that an increase in supply pressure or circumferentially elongating the groove primarily improve the cooling effect through enlarging the lubricant mixing zone. In fact, increasing the groove length from 25 mm to 75 mm reduces the maximum film temperature by 10%, but does not influence its location. In addition, the shape (square, round, or pyramid) of a groove does not influence the lubricant mixing effectiveness.

In 2014, Uhkoetter et al. [37] for the first time employ a 3D CFD method to analyze the feeding groove region and also construct a large scaled test rig to verify the CFD predictions. The authors use large eddy simulation (LES), a high fidelity yet numerically inexpensive (relative to direct numerical simulation, DNS) method that takes into account the turbulent flow in the groove region. The test rig has an upscaled geometry of the groove region (slightly simplified) and is made of clear acrylic glass. The test rig working fluid is air with a similar Reynolds number as the oil in the actual bearing groove (fully turbulent,  $Re > 1300$ ). The authors calibrate qualitatively the CFD prediction by visualizing the flow in the test rig with fog. Uhkoetter et al. define a *Reynolds ratio* ( $ReR$ ) as the Reynolds number of the film flow divided by the supply flow Reynolds number. The authors vary the groove width while keeping the supply flow rate constant to investigate the influence of Reynolds ratio ( $ReR$ ) on the groove temperature distribution. With a high Reynolds ratio ( $ReR = 63$ : high film velocity) the supply flow forms a recirculation zone against the shaft rotation leading to a homogeneous mixing. With a low Reynolds ratio ( $ReR = 5$ : high

supply jet velocity), however, the supply flow penetrates the boundary layer attached to the shaft and causes an inhomogeneous flow mixing. The authors conclude that while a low  $ReR$  (such as a wider groove, or a lower supply flow velocity) creates a more homogeneous mixing, the inhomogeneous groove mixing is more effective in reducing the maximum film temperature.

### 3.3 Literature review closure

The body of the literature reviewed reveals that a thermally induced pad deformation is a combination of an unwrapping effect on a pad and a thermal growth depending on the pad thickness and arc length as well as the imposed temperature field. Thermal deformations are primarily a function of shaft speed that increases the shear drag power loss within the bearing. For thick pads, these deformations have a more significant influence on bearing performance. Including thermally induced deformations of the pads, shaft, and housing reduces the bearing clearance and therefore increases the bearing stiffness. Furthermore, the effects lead to a slight increase of the maximum pad temperature, while markedly reducing the minimum film thickness and raising the maximum hydrodynamic pressure.

On the other hand, a pressure induced pad deformation gains dominance for a heavily loaded pad through increasing its curvature (unwrapping), especially on a thin pad. Including pressure induced deformations alone reduces the predicted stiffness and damping coefficients. Ultimately, both thermal and pressure induced elastic deformations must be taken into account for an accurate analysis of TPJBs, regardless of the shaft speed or applied load.

The bulk of the lumped parameter models for mixing of the fluids in the feed groove of a TPJB use a single empirical coefficient ( $\lambda$ ) to estimate the film temperature at the leading edge of a pad. Few models implement a full THD analysis or a computational fluid dynamic (CFD) method to analyze this region. A fully analytical or numerical model

requires knowledge of the groove configuration and geometry, end seals, direct lubrication, etc. The complexity of the mentioned methods renders them suitable only for a very detailed analysis in a particular design, not a general predictive tool. Thus, the current work pursues an in-depth analysis of a typical feed groove to develop an experimentally validated improved lumped parameter model for thermal mixing.

## 4 DESCRIPTION OF THE PREDICTION MODEL

Figure 5 shows the geometry of a tilting pad along with the definition of variables used throughout this section. The following explains briefly the physical model to determine the pressure field in a hydrodynamic film and the temperature field in the fluid film and the bounding solids.

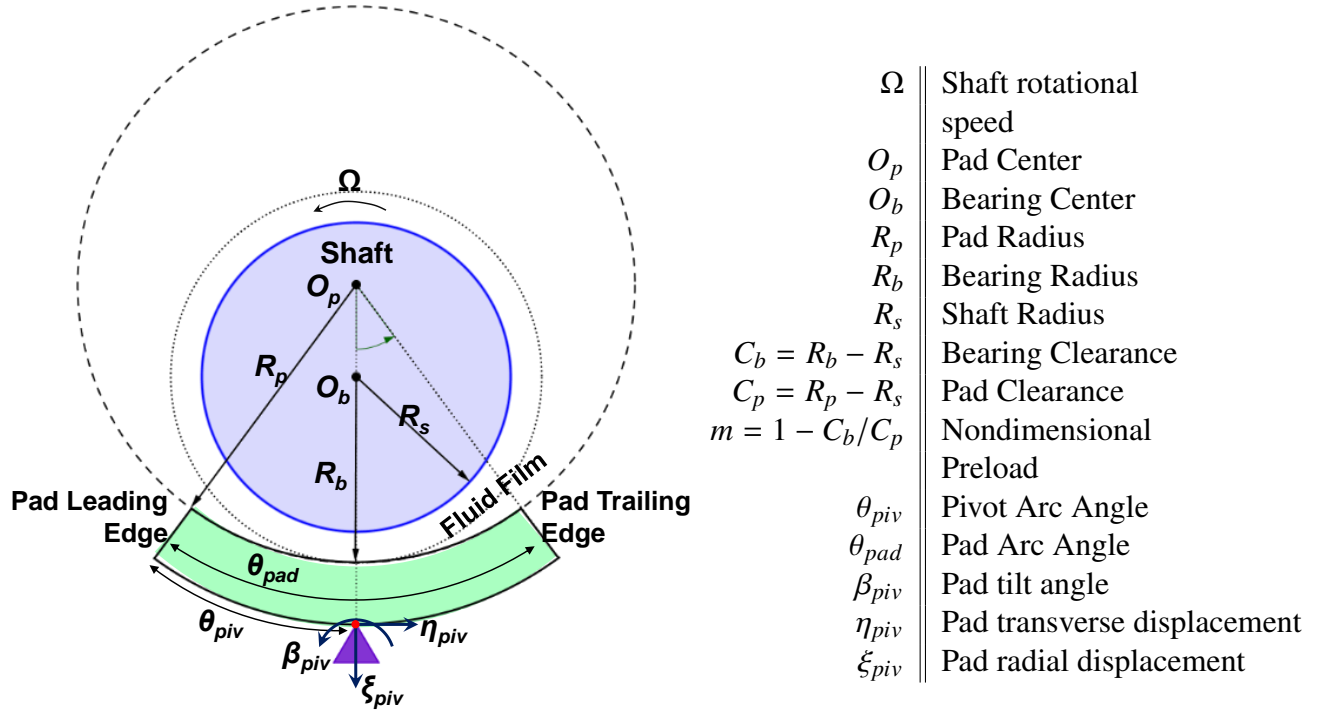


Figure 5: Geometry of one tilting pad and nomenclature.

### 4.1 Reynolds equation

San Andrés and Tao [22] state an extended Reynolds equation governing the generation of the pressure field ( $p$ ) in a TPJB, accounting for temporal fluid inertia. On each pad, this equation is

$$\frac{1}{R_s^2} \frac{\partial}{\partial \theta} \left( \frac{H^3}{\kappa_x \mu} \frac{\partial p}{\partial \theta} \right) + \frac{\partial}{\partial z} \left( \frac{H^3}{\kappa_z \mu} \frac{\partial p}{\partial z} \right) = \frac{\partial H}{\partial t} + \frac{\Omega}{2} \frac{\partial H}{\partial \theta} + \frac{\rho H^2}{\kappa_J \mu} \frac{\partial^2 H}{\partial t^2} \quad (4)$$

where the lubricant viscosity ( $\mu$ ) is a function of the film temperature ( $T_{(\theta)}$ ), and  $(\theta, z)$  are the circumferential and axial coordinates on the plane of the bearing. Above,  $\kappa_x, \kappa_z$  and  $\kappa_J = (\kappa_x + \kappa_z)/2$  are turbulent flow shear parameters which are functions of the film flow Reynolds number ( $Re = \frac{\rho H}{\mu} \sqrt{U^2 + W^2}$ , where  $(U, W)$  are cross-film averaged velocities along circumferential and axial directions) [41]. TPJBs generally operate in a laminar flow condition ( $Re < 1000$ ), for which the shear parameters are  $\kappa_x = \kappa_z = \kappa_J = 12$ .

The film thickness ( $H_{(\theta,z)}$ ) as a function of circumferential ( $\theta$ ) and axial ( $z$ ) coordinates is defined as

$$H_{(\theta,z)} = C_p + \delta_{(\theta,z)} - (\Delta R_s - \Delta R_h) + e_x \cos \theta + e_y \sin \theta + [\xi_{piv} - C_p + C_b] \cos (\theta - \theta_p) + [\eta_{piv} - R_{back} \beta_{piv}] \sin (\theta - \theta_p) \quad (5)$$

where  $e_x, e_y$  are the journal center displacements,  $(\xi_{piv}, \eta_{piv})$  are the pad radial and transverse displacements in pad pivot local coordinates. Above,  $R_{back}$  is the sum of the pad machined radius and pad thickness at the pivot position,  $\beta_{piv}$  is the pad tilt angle, and  $\theta_p$  is the pivot angular position starting from  $x$  axis. The equation accounts for shaft expansion ( $\Delta R_s$ ) and housing expansion ( $\Delta R_h$ ) in the radial direction. The elastic deformation of each pad inner surface ( $\delta_{(\theta,z)}$ ) modifies the film thickness along the radial direction and includes both thermally induced and pressure induced deformations.

## 4.2 Bulk flow energy transport equation

Ref. [41] implements a steady-state bulk flow energy transport equation for a steady state condition and an incompressible fluid. The conservation of energy states that the energy cannot be created or destroyed. Hence, the energy transport (Eq. (6)) balances the energy disposed (LHS) and the energy generated (RHS) in a TPJB. Viscous dissipation generates heat that disposes through convection and diffusion in the fluid film. The



energy transport equation below averages the fluid temperature across the film. The simplification offers a good balance between implementation complexity, quality of results, and calculation time [42].

$$c_p \left[ \frac{\partial (\rho HUT)}{R_s \partial \theta} + \frac{\partial (\rho HWT)}{\partial z} \right] + \Phi = H \frac{\Omega R_s}{2} \frac{\partial p}{R_s \partial \theta} + \frac{\mu}{H} \left[ \kappa_x \left( W^2 + U^2 + \frac{U \Omega R_s}{2} \right) + \kappa_J \Omega R_s \left( \frac{\Omega R_s}{4} - U \right) \right] \quad (6)$$

where  $c_p$  is the fluid specific heat. In a laminar flow condition the shear parameters  $\kappa_x = \kappa_z = \kappa_J = 12$ , therefore Eq. (6) becomes

$$c_p \left[ \frac{\partial (\rho HUT)}{R_s \partial \theta} + \frac{\partial (\rho HWT)}{\partial z} \right] + \Phi = \frac{12\mu}{H} \left( W^2 + U^2 - U \Omega R_s + \frac{\Omega^2 R_s^2}{2} \right) \quad (7)$$

where  $T$  is a bulk flow (primitive) variable for cross-film averaged temperature;  $(U, W)$  represent the circumferential and axial mean flow velocities

$$U = -\frac{H^2}{\kappa_x \mu} \frac{\partial p}{R_s \partial \theta} + \frac{\kappa_J \Omega R_s}{\kappa_x} \quad \text{and} \quad W = -\frac{H^2}{\kappa_z \mu} \frac{\partial p}{\partial z} \quad (8)$$

In Eqs. (6) and (7), the heat flow from the fluid film to a pad and the journal surfaces is

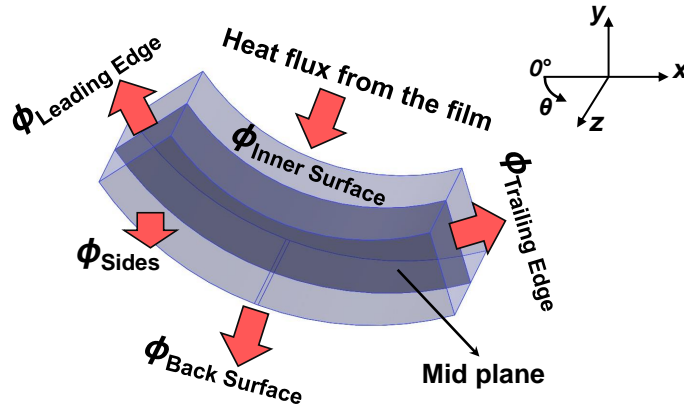
$$\Phi = \underbrace{h_p (T_{(\theta)} - T'_{(R_p, \theta)})}_{\text{heat transfer to pad}} + \underbrace{h_s (T_{(\theta)} - T_s)}_{\text{heat transfer to shaft}} \quad (9)$$

where  $h_p$  is the heat transfer coefficient between the the film and the pad inner surface (at a temperature  $T'_{(R_p, \theta)}$ ).  $h_s$  is the heat transfer coefficient between the film and the shaft surface (at a temperature  $T_s$ ). An empirical correlation by Hausen [43] specifies  $h_p$  and  $h_s$  for thermally developing flow (constant wall temperature). The empirical correlations generate variable convection coefficients ( $h_p, h_s$ ) as a function of the film thickness, shaft

diameter, shaft speed, and pad arc length.

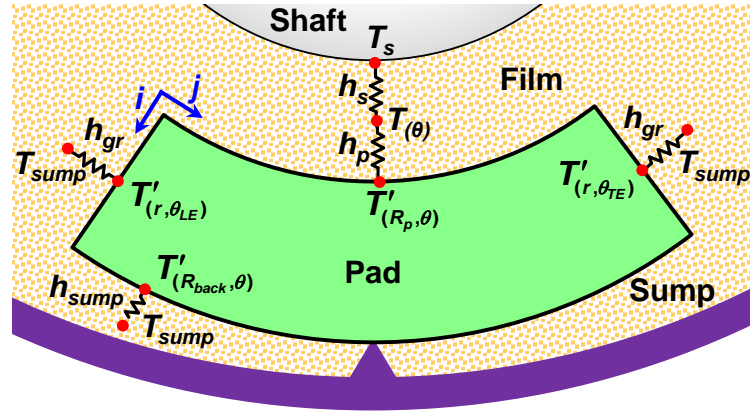
### 4.3 Temperature distribution in a pad

Figure 6 shows the heat flux from the fluid film that enters a pad from its inner surface along with the heat fluxes leaving the pad to the surrounding lubricant. The present work assumes negligible film temperature variations in the axial direction and no axial heat transfer from pad walls ( $\Phi_{sides} = 0$ ). Therefore, the film temperature and the pad temperature field is solved in the bearing mid-plane along the circumferential direction.



**Figure 6: Heat fluxes ( $\Phi$ ) entering and leaving a bearing pad through its surfaces.**

Figure 7 illustrates the boundary conditions for the current thermal model. Resistor-like symbols represent the heat transfer coefficients between the pad and the lubricant around it. Here, a shaft and a single pad are subject to radial heat transfer from the fluid film. The heat flux enters the pad from its inner surface and exits through the pad's back surface, leading edge, and trailing edge to the surrounding oil in the sump and groove regions. The heat transfer across the pad's bounding surfaces is treated by lumped parameter temperatures.



**Figure 7: Thermal model accounting for the heat transfer between the film, pad and journal as well as heat transfer between the pad and surrounding lubricant.**

The flow in the sump region (underneath a pad) is turbulent due to the oil churning, particularly in a bearing with end seals [44]. The heat transfer coefficient for the sump oil is determined from an empirical correlation for turbulent flow in concentric annular ducts by Gnielinski [45]. The temperature of the lubricant in the sump region is reasonably assumed as the oil discharge temperature. The discharge temperature can also be calculated assuming a portion of the total heat generated due to shear power loss is removed by the lubricant [44].

Complexity of the flow in the groove region prohibits determining a convection coefficient for this region by means of analytical or empirical correlations. In the archival literature, the assumed convection coefficients for the groove region vary greatly. Ref. [46] reviews previous studies and finds the heat convection coefficient ranges from 100 W/(m<sup>2</sup> °K) to 2,840 W/(m<sup>2</sup> °K) for a large size tilting pad thrust bearing. Presently, a groove convection coefficient  $h_{gr} = 1750 \text{ W/(m}^2 \text{ °K)}$  is chosen as it best predicts the location of maximum temperature on pad surface (i.e. 75% of the angular location) for several bearing examples considered (Refs. [1, 3, 33]). Note that the chosen convection coefficient at the groove interface ( $h_{gr}$ ) is not universal, i.e. not necessarily applicable to all bearings.

The current thermal model assumes the pad axial sides are adiabatic and the temperature within a pad only varies along the radial and circumferential directions. The equation governing the temperature field in a pad ( $T'_{(r,\theta)}$ ) is written in a cylindrical coordinate system as [47]

$$\frac{1}{r} \frac{\partial}{\partial r} \left( r \frac{\partial T'}{\partial r} \right) + \frac{1}{r^2} \frac{\partial^2 T'}{\partial \theta^2} = 0 \quad (10)$$

The boundary conditions on all sides of a pad are of convection type. The pad inner surface removes heat from the fluid film at a temperature  $T(\theta)$ . The sides and back surfaces of the pad exchange heat with the surrounding oil at the sump temperature ( $T_{sump}$ ) [48]. The heat flow across the boundary surfaces on a pad are:

$$\text{Inner surface: } k_{pad} \frac{\partial T'_{(r,\theta)}}{\partial r} \Big|_{r=R_p} = h_p (T'_{(R_p,\theta)} - T(\theta)) \quad (11)$$

$$\text{Back surface: } k_{pad} \frac{\partial T'_{(r,\theta)}}{\partial r} \Big|_{r=R_{back}} = -h_{back} (T'_{(R_{back},\theta)} - T_{sump}) \quad (12)$$

$$\text{Leading edge groove: } k_{pad} \frac{\partial T'_{(r,\theta)}}{\partial \theta} \Big|_{\theta=\theta_{LE}} = -h_{gr} (T'_{(r,\theta_{LE})} - T_{sump}) \quad (13)$$

$$\text{Trailing edge groove: } k_{pad} \frac{\partial T'_{(r,\theta)}}{\partial \theta} \Big|_{\theta=\theta_{TE}} = -h_{gr} (T'_{(r,\theta_{TE})} - T_{sump}) \quad (14)$$

Figure 8 shows an example of the predicted two dimensional temperature field within the pads as well as the fluid film temperature for a four pad, LBP bearing. The loaded pads (1,2) are hotter and have a larger temperature gradient compared to the unloaded pads (3,4). The location of the maximum temperature for each pad falls around 75% of the pad's angular length, though it depends on the assumed heat transfer coefficient for the grooves. The journal temperature is averaged from film temperature on all pads, and the bearing housing temperature is equal to sump temperature.

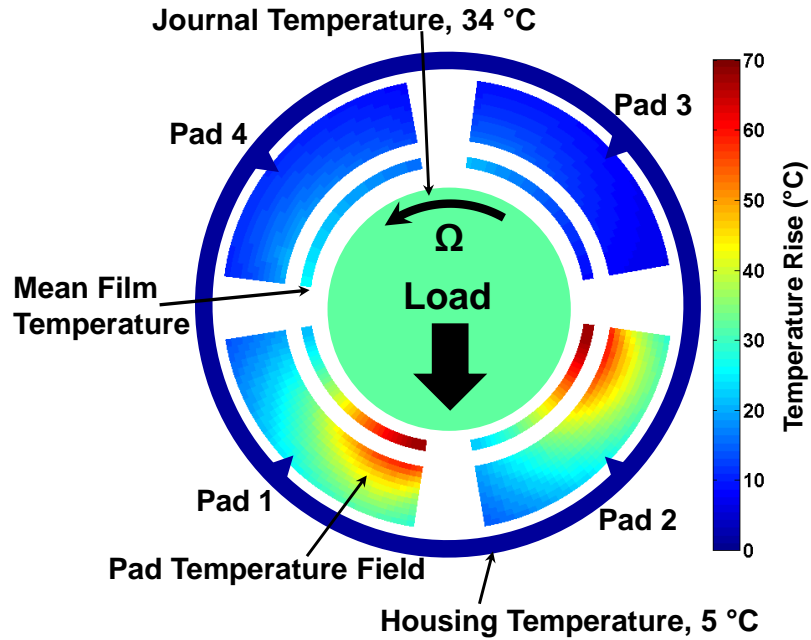


Figure 8: Example of two dimensional temperature rise distribution in the pads and the mean film temperature of a TPJB operating at a shaft speed of 16,000 RPM and under a specific load of 2.9 MPa. (Temperature rise from an oil supply at 49 °C)

#### 4.4 Lubricant mixing at a feed groove

Recent improvements to model the mixing of lubricant in a feed groove include a flow balance based on the lubricant local pressure [20, 49], defining a lower limit for the leading edge film temperature based on the actual supply flow rate [21], developing a full 3D thermohydrodynamic model with no (empirical) mixing coefficients [1], and formulating a detailed control volume energy balance [18].

A major drawback of the simple hot oil carry over model (Eq. (1) page 4, see Refs. [16, 50]) is that it predicts a supply flow only based on the upstream flow ( $Q_{TE}^{i-1}$ ) and downstream ( $Q_{LE}^i$ ) flow adjacent to a groove. Therefore, unless the predicted flow rates are close to actual ones, the simple mixing model predicts an inaccurate leading edge film temperature. In fact, He et al. [21] attribute the error in pad inner surface temperature predictions to the limitations of the thermoelastic deformation model, including 2D pad

deformation with a simplified geometry and not directly modeling the thermal expansion of the housing and shaft. The pressure and thermally induced deformations of the pads, shaft, and housing modify the film thickness, and therefore the flow rates ( $Q_{LE}^i$  and  $Q_{TE}^{i-1}$ ) on each pad. Most predictive tools use simplifying assumptions to model these mechanical and thermal deformations. Thus, the predicted film thickness and supply flow rate may diverge from those during an operation.

Refs. [20, 49] calculate a pressure in each groove that determines its supply flow rate based on a local pressure difference ( $\Delta P = P_{sup} - P_{gr}$ ). The supply flow rate and side leakage flow rate are determined from an orifice flow equation,

$$Q = A C_d \sqrt{\frac{2}{\rho} \Delta P} \quad (15)$$

where  $Q$  is the flow rate,  $A$  is the orifice section area,  $C_d$  is the discharge coefficient with a typical magnitude of 0.61,  $\rho$  is the fluid density, and  $\Delta P$  is the pressure difference across the orifice.

The work [49] predicts that a loaded pad receives about 40% less supply lubricant than an unloaded one. However, the orifice equation has at its source an inviscid fluid (from Bernoulli's equation), and the discharge coefficient ( $C_d$ ) represents deviation from an inviscid fluid for which  $C_d = 1$ . To match prediction with the actual supply flow rate, Conti et al. [49] use a  $C_d = 0.02$ , that clearly shows Eq. (15) fails to model the flow through a feed orifice.

He et al. [51] state “in practice, the total lubricant supply flow rate ( $Q_{sup}^{total}$ ) is usually controlled by the supply pressure and is known before analysis.” The authors suggest that it is reasonable to assume the total supply flow rate distributes evenly among the  $n$  grooves. In other words, each groove collects an identical fraction of the total flow supplied, namely

$$Q_{sup}^i = \frac{Q_{sup}^{total}}{n} \quad (16)$$

However, He et al. [51] also state that Eq. (16) does not always satisfy mass flow continuity condition in a feed groove. For an operation at a large journal eccentricity, as shown in Figure 9, the journal operates near the groove between pad ④ and ①. Here, the inlet film thickness of pad ① reduces and  $Q_{LE}^1 < (Q_{TE}^4 + Q_{sup}^1)$ . In this situation, the authors [51] suggest that this groove acts as a flow restrictor, and receives less fresh lubricant due to a fluid pressure rise within the groove. The authors speculate that if a particular groove receives an excessive supply of oil, a fraction of it immediately displaces outwards as side leakage.

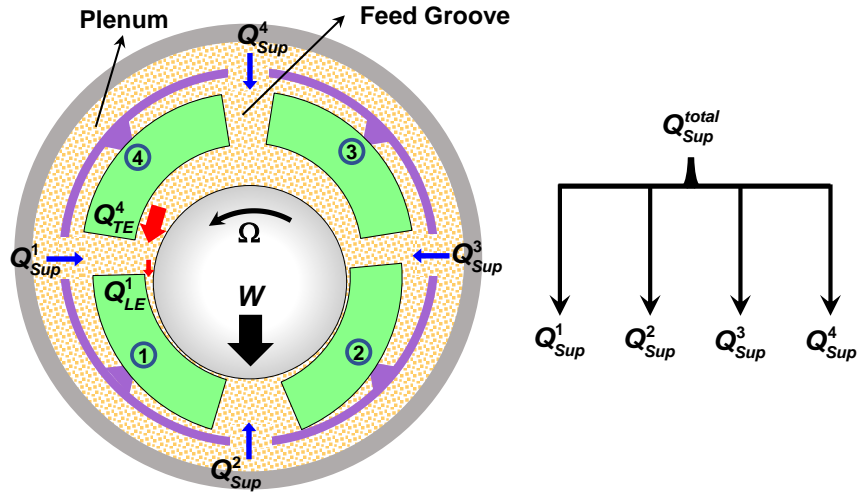


**Figure 9: Left: schematic view of a heavily loaded TPJB operating at a large journal eccentricity. Right: a hydraulic network that allocates the supply flow for each feed groove.**

The right side of Figure 9 shows an idealized representation of the total supplied flow ( $Q_{sup}^{total}$ ) dividing into separate streams ( $Q_{sup}^i$ ). A deep outer groove on the bearing housing OD (plenum) contains the fresh lubricant at the supply temperature and feeds each orifice based on the groove local pressure on the other side of the hole.

Due to the complexity of the flow in the groove region, determining a local pressure

for the groove is not practical. Instead, the current model extends Eq. (16) to account for excessive demand or restriction of individual grooves.

Classical lubrication theory defines circumferential velocity of the fluid film as a superposition of a shear driven flow induced by the motion of the shaft (Couette flow) and a pressure driven flow (Poiseuille flow) [52]. The axial flow only comprises of a pressure driven flow. The circumferential flow at a pad leading and trailing edges is,

$$Q \Big|_{\theta_{LE}, \theta_{TE}} = Q_{shear} + Q_{pressure} = \frac{\Omega R_s L h}{2} \Big|_{\theta_{LE}, \theta_{TE}} + \int_{-L/2}^{L/2} \left( -\frac{h^3}{12\mu R_s} \frac{\partial P}{\partial \theta} \right)_{\theta_{LE}, \theta_{TE}} dz \quad (17)$$

At a pad leading edge, the pressure gradient is positive ( $\partial P / \partial \theta > 0$ ) and hence the pressure driven flow is in the opposite direction of the shaft surface velocity and its shear driven flow. At a pad trailing edge, however, the two effects induce a flow in the same direction ( $\partial P / \partial \theta < 0$ ).

The first step to quantify the restriction or demand of each groove for fresh (cold) lubricant, introduces a *groove demand* ( $C_i$ ) parameter that accounts for the following:<sup>6</sup>

- A pad leading edge shear driven (forward) flow (proportional to film thickness) increases the demand for supply lubricant. The pads with a large leading edge film thickness, as is the case for unloaded pads ③ and ④ (see Figure 9), receive a large flow at their inlet. On the other hand, a large hydrodynamic pressure gradient (on the loaded pads ① and ②) may cause a significant flow in reverse direction that curtails the flow demand.
- At a pad trailing edge the pressure driven flow adds to the shear flow, pushing the flow in the same direction as the shaft surface motion. A large flow leaving from

---

<sup>6</sup>Note the assumptions are only true if all the pads are fully wetted (flooded) and able to maintain a full film throughout every pad.



upstream pad ( $Q_{TE}^{i-1}$ ) may provide an excess amount of flow to fill in the downstream pad leading edge film, and this reduces the demand for additional supply flow. The leading edge flow of pads ① and ② are about the same (see Figure 9), but pad ① receives a large flow from upstream (usually hot), reducing its demand for supply oil. Similarly, the leading edge flow of pads ③ and ④ are about the same, but pad ③ receives a very small flow from upstream which amplifies its need for more supply oil.

The demand parameter ( $C_i$ ) for the  $i^{th}$  groove equals the ratio between the downstream leading edge shear flow rate ( $Q_{shear}^i$ ) that leaves the groove and sum of the trailing edge flow rate ( $Q_{TE}^{i-1}$ ) and the leading edge reverse (pressure driven) flow rate ( $Q_{pressure}^i$ ) which both enter the groove.  $C_i = 1$  if the downstream and upstream flows are equal (i.e. an ideal centered journal and bearing).  $C_i < 1$  for the  $i^{th}$  groove that restricts the supply flow, and  $C_i > 1$  for the  $i^{th}$  groove that demands extra lubricant. The demand parameter at the  $i^{th}$  groove ( $i = 1, \dots, n$ ) is,

$$\begin{aligned}
 C_i &= \frac{Q_{shear}^i}{-Q_{pressure}^i + Q_{TE}^{i-1}} \Big|_{i=1, \dots, n} \\
 &= \frac{\overbrace{\frac{\Omega R_s L h_i}{2} \Big|_{\theta_{LE}}}^{\text{Shear (forward) flow}}}{\underbrace{\int_{-L/2}^{L/2} \left( \frac{h_i^3}{12\mu R_s} \frac{\partial P_i}{\partial \theta} \right) dz}_{\text{Pressure (reverse) flow}} + \underbrace{\int_{-L/2}^{L/2} \left( \frac{-h_{i-1}^3}{12\mu R_s} \frac{\partial P_{i-1}}{\partial \theta} \right) dz + \frac{\Omega R_s L h_{i-1}}{2} \Big|_{\theta_{TE}}}_{\text{Downstream Pad trailing edge flow}}} \quad (18)
 \end{aligned}$$

The second step adds  $C_i|_{i=1, \dots, n}$  to produce a total demand parameter ( $C_{total}$ ). The

available total supply flow ( $Q_{sup}^{total}$ ) meets the total demand by the bearing.

$$C_{total} = \sum_{i=1}^n C_i \quad (19)$$

As the final step, a groove receives a portion of the total supply flow based on its demand ( $C_i$ ) relative to the total demand ( $C_{total}$ ). Here the grooves with a larger demand receive a greater portion of the supply flow. Let  $\alpha_i$  denote a fraction of total flow, the supply flow allocated to each groove is,

$$Q_{sup}^i = \frac{C_i}{C_{total}} Q_{sup}^{total} = \alpha_i Q_{sup}^{total} \quad ; \quad i = 1, \dots, n \quad (20)$$

For a large size five-pad TPJB tested by Hagemann et al. [1], Figure 10 (right side) shows the calculated fraction of total supply flow ( $\alpha_i$ ) for each pad versus shaft speed and specific load. The left side of the graph shows  $\alpha_i$  for a four-pad TPJB<sup>7</sup> tested by Coghlan and Childs [3]. Both bearings operate in a load between pad (LBP) configuration, with the bottom two pads [(1&2) and (3&4)] supporting the applied load. The dashed red line marks equal flow fractions on each pad at  $W/(LD) = 0$  where the demand parameter  $C_i \approx 1$  for all the grooves and hence each receives ( $\alpha_i \approx 1/n$ ) of the total flow.

As the load increases the shaft eccentricity in the load direction becomes larger and a small inlet film thickness restricts the flow for loaded pads (reducing  $\alpha_i$ ); whereas a large film thickness on the unloaded pads requires more lubricant to create a full film (increasing  $\alpha_i$ ). Thus, the difference between the flow fraction for the loaded and unloaded pads grows as the load increases. An increase in shaft speed shifts the journal to a more centered position ( $e_x, e_y \rightarrow 0$ ), and (at a given load) slightly reduces the difference. Notably, Pads ④ on the left side and ② on the right side (although unloaded) receive a small fraction

---

<sup>7</sup>Refer to Table 1 (page 51) and Table 4 (page 66) for a full description of the above bearings.

of the total supply flow which is due to the large upstream flow from pads ③ and ①, respectively.

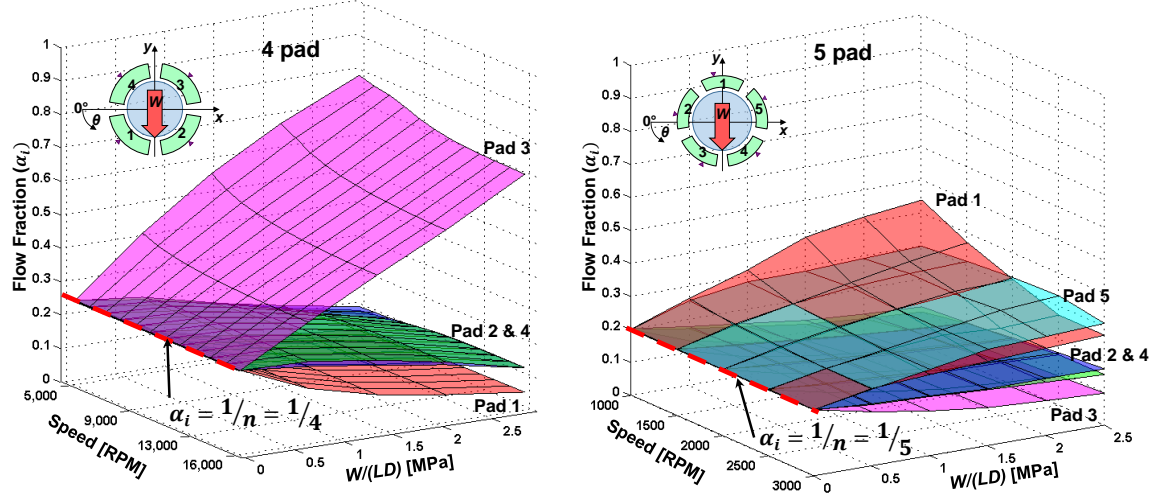


**Figure 10: Predicted fractions of total supply flow ( $\alpha_i$ ) allocated to each groove for a 4 and a 5 pad TPJB with details in Tables 1 and 4. (Dashed red lines specify an even distribution at zero load)**

Figure 11 shows the lubricant flows and heat fluxes entering and exiting the boundaries of a control volume that represents a groove region. Cold lubricant is supplied into the bearing at a known flow rate ( $Q_{sup}^i$ ) and temperature ( $T_{sup}$ ). Hot oil leaving the trailing edge of the upstream pad with a flow rate ( $Q_{TE}^{i-1}$ ) and a temperature ( $T_{TE}^{i-1}$ ), loses some of its heat in the groove region and reaches the leading edge of the downstream pad with a flow rate ( $Q_{LE}^i$ ) and a temperature ( $T_{LE}^i$ ).

Based on the description in Ref. [51], if  $(Q_{TE}^{i-1} + Q_{sup}^i) > Q_{LE}^i$ , the excess oil leaves the groove as a side leakage flow ( $Q_{SL}^i$ ). Conversely, if the sum of the supply flow and upstream flow is not enough to fill in the downstream pad leading edge ( $(Q_{TE}^{i-1} + Q_{sup}^i) < Q_{LE}^i$ ), then to satisfy the continuity, the rest of the needed lubricant is drawn from the churning oil in the groove ( $Q_{gr}^i$ ) [53]. According to the thermal mixing flow model in Ref. [53], for a groove with a non-zero side leakage flow ( $Q_{SL}^i$ ), the groove recirculating flow

$(Q_{gr}^i)$  is zero and vice versa.

$$Q_{SL}^i = Q_{TE}^{i-1} + Q_{sup}^i - Q_{LE}^i \quad \text{if } (Q_{TE}^{i-1} + Q_{sup}^i) > Q_{LE}^i \quad (21a)$$

$$Q_{gr}^i = Q_{LE}^i - Q_{TE}^{i-1} - Q_{sup}^i \quad \text{if } (Q_{TE}^{i-1} + Q_{sup}^i) < Q_{LE}^i \quad (21b)$$

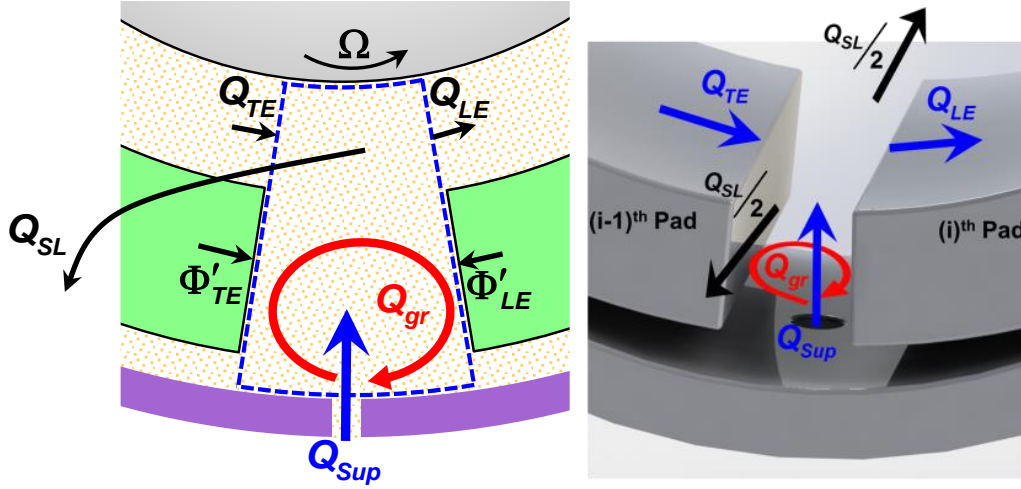


**Figure 11: Mixing in a feed groove region of hot oil leaving an upstream pad ( $Q_{TE}^{i-1}$ ) with a cold supply flow ( $Q_{sup}^i$ ). Including side leakage flow ( $Q_{SL}^i$ ) and groove recirculating flow ( $Q_{gr}^i$ ) as well as heat transfer with the bounding pads ( $\Phi'_{TE}$ ,  $\Phi'_{LE}$ ).**

In the conventional model (Eqs. (1)) reproduced below, first a flow balance between (a portion of) upstream flow ( $\lambda Q_{TE}^{i-1}$ ) and downstream flow ( $Q_{LE}^i$ ) sets the needed supply flow rate ( $Q_{sup}^i$ ) for each groove. Subsequently, a thermal energy balance requires the heat flowing into a downstream pad leading edge (LE) to be equal to sum of thermal energy from a portion of *hot* upstream trailing edge (TE) heat flow and the *cold* supply heat flow. A hot oil carry over coefficient ( $\lambda$ ) specifies the above-mentioned portion of the hot upstream lubricant that reaches the downstream pad, i.e.

$$Q_{LE}^i = Q_{sup}^i + \lambda Q_{TE}^{i-1} \quad (1a)$$

$$\rho c_p (T_{LE}^i Q_{LE}^i) = \rho c_p (Q_{sup}^i T_{sup} + (\lambda Q_{TE}^{i-1}) T_{LE}^{i-1}) \quad (1b)$$

The present model, however, emphasizes on the portion of hot oil that does not reach the next pad and either leaks out from the sides or recirculates within the groove. The temperature of the discharge side leakage flow ( $T_{SL}^i$ ) and churning oil in the groove ( $T_{gr}^i$ ) depend on the upstream oil temperature and flow rate ( $T_{TE}^{i-1}, Q_{TE}^{i-1}$ ) as well as supply temperature and flow rate ( $T_{sup}, Q_{sup}^i$ ).

In a bearing groove, thermal energy (heat) flows mainly by means of fluid motion, i.e. an *advection heat transfer* mechanism. Fluid flow ( $Q$ ) transports energy from one location to another, and the advection heat flow ( $\Phi$ ) is

$$\Phi = \rho c_p Q \Delta T \quad (23)$$

where  $\Delta T$  is the temperature difference and  $\rho c_p Q = c_p \dot{m}$  is thermal capacitance of the fluid flow.

Figure 12 shows two versions of the control volume at a groove, the left control volume refers to a situation where side leakage occur, and the one on the right refers to a condition where oil streams recirculate in the groove. In both, a heat flow ( $\Phi$ ) is transported internally by the mixing of fluids. The left sub control volume (bottom part) assumes that only a portion of the streams that flow into the groove (the hot upstream oil and the cold supply oil stream) carry the thermal energy that is transferred to the side leakage stream. Therefore, the heat flowing into the leading edge section of the downstream pad is omitted.

A *mixing efficiency* parameter ( $0 < C_{gr} < 1$ ) represents the ability of an oil feed groove arrangement to lubricate the downstream pad with fresh (cold) supply oil while discharging the upstream hot oil (displacing it to the sides). Hence,  $C_{gr}$  specifies the portion of the heat that flows from the *hot* upstream section ( $\Phi_{TE,SL}$ ) and the *cold* supply oil ( $\Phi_{sup,SL}$ ). Thermal energy must still be conserved within a sub control volume, thus the sum of two heat flows is nil ( $\Phi_{TE,SL} + \Phi_{sup,SL} = 0$ ).

Recall based on Eq. (21), either the side leakage flow ( $Q_{SL}$ ) or the groove churning flow ( $Q_{gr}$ ) can be present in a groove, but not both. Hence, the right side of Figure 12 also assumes that only a portion of the fluid streams that flow into the groove contribute to transporting thermal energy to the oil stream that churns within the groove and therefore  $\Phi_{TE,gr} + \Phi_{sup,gr} = 0$ .

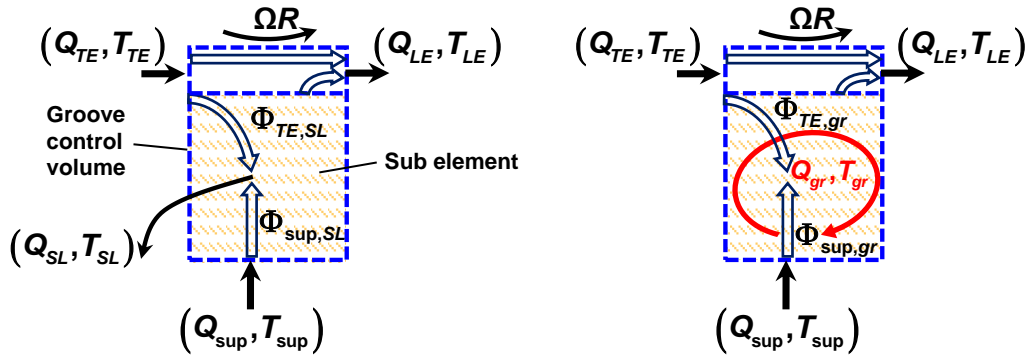


Figure 12: Groove control volume including fluid streams (solid arrows), and heat flows (hollow arrows). *Left:* heat flows from *hot* upstream oil ( $\Phi_{TE,SL}$ ) and the *cold* supply oil ( $\Phi_{sup,SL}$ ) to oil stream that discharges from the groove. *Right:* heat flows from *hot* upstream oil ( $\Phi_{TE,gr}$ ) and the *cold* supply oil ( $\Phi_{sup,gr}$ ) to the oil stream that recirculates within the groove.

Conservation of energy establishes that the sum of the thermal energy transferred between the *hot* upstream oil and the side leakage oil ( $\Phi_{TE,SL}$ ) and that between the side leakage oil and *cold* the supply oil ( $\Phi_{sup,SL}$ ) is equal to zero.

$$\underbrace{C_{gr} \left[ \rho c_p Q_{TE}^{i-1} (T_{TE}^{i-1} - T_{SL}^i) \right]}_{\Phi_{TE,SL} > 0} + \underbrace{(1 - C_{gr}) \left[ \rho c_p Q_{sup}^i (T_{sup} - T_{SL}^i) \right]}_{\Phi_{sup,SL} < 0} = 0 \quad (24)$$

The temperature of side leakage ( $T_{SL}^i$ ) after isolating it from Eq. (24) becomes,

$$T_{SL}^i = \frac{C_{gr} Q_{TE}^{i-1} T_{TE}^{i-1} + (1 - C_{gr}) Q_{sup}^i T_{sup}}{C_{gr} Q_{TE}^{i-1} + (1 - C_{gr}) Q_{sup}^i} \quad (25)$$

Direct lubrication methods such as a leading edge groove reduce hot oil carry over, which

means the side leakage lubricant receives most of thermal energy form hot upstream oil and  $T_{SL}^i$  is closer to the upstream temperature ( $T_{TE}^{i-1}$ ), hence  $C_{gr} \rightarrow 1$ . On the other hand, when the bearing axial ends are sealed (flooded bearing) the hot upstream oil mixes with the cold supply oil before being squeezed out as a side leakage, hence  $C_{gr} \rightarrow 0$ .

In the absence of any side leakage flow, a similar energy balance establishes that sum of the thermal energy transfered between hot upstream trailing edge oil and churning oil in the groove ( $\Phi_{TE,gr}$ ) and that between churning oil and cold supply oil ( $\Phi_{sup,gr}$ ) is zero.

$$\underbrace{(1 - C_{gr}) \left[ \rho c_p Q_{TE}^{i-1} (T_{TE}^{i-1} - T_{gr}^i) \right]}_{\Phi_{TE,gr} > 0} + \underbrace{C_{gr} \left[ \rho c_p Q_{sup}^i (T_{sup} - T_{gr}^i) \right]}_{\Phi_{sup,gr} < 0} = 0 \quad (26)$$

From Eq. (26) above, the temperature of recirculating oil in the groove ( $T_{gr}^i$ ) is

$$T_{gr}^i = \frac{(1 - C_{gr}) Q_{TE}^{i-1} T_{TE}^{i-1} + C_{gr} Q_{sup}^i T_{sup}}{(1 - C_{gr}) Q_{TE}^{i-1} + C_{gr} Q_{sup}^i} \quad (27)$$

The temperature of the churning oil in the groove ( $T_{gr}^i$ ) is closer to  $T_{sup}$  if the majority of the hot upstream oil discharges from the sides ( $C_{gr} \rightarrow 1$ ). However, for a flooded bearing a large portion of upstream oil recirculates in the groove, increasing  $T_{gr}^i$  to a magnitude close to  $T_{LE}^i$  ( $C_{gr} \rightarrow 0$ ). In other words, the larger the side leakage temperature ( $T_{SL}^i$ ), the smaller the groove temperature ( $T_{gr}^i$ ) and vice versa. Therefore, the groove temperature ( $T_{gr}^i$ ) is the counterpart of the side leakage temperature ( $T_{SL}^i$ ),

Some heat is also transfered from the trailing edge and the leading edge walls of the adjacent pads to the oil that is recirculating in the groove. The heat flows ( $\Phi_{TE}$ ,  $\Phi_{LE}$ ) are obtained from integrating the convective heat fluxes across the respective fluid-solid

boundary,

$$\Phi'_{LE} = h_{gr}L \int_{R_{back}}^{R_p} (T'(r, \theta_{LE}) - T_{sump}) dr \quad (28)$$

$$\Phi'_{TE} = h_{gr}L \int_{R_{back}}^{R_p} (T'(r, \theta_{TE}) - T_{sump}) dr \quad (29)$$

where  $L$  is a pad axial length,  $h_{gr}$  is the convection coefficient of the lubricant in the groove.

An energy balance method takes into account all the aforementioned heat fluxes to determine the film temperature at the leading edge of the downstream pad ( $T_{LE}^i$ ). The approach is energy conservative, namely at the  $i^{th}$  groove

$$\underbrace{\rho c_p \left( Q_{TE}^{i-1} T_{TE}^{i-1} + Q_{sup}^i T_{sup} + Q_{gr}^i T_{gr}^i \right)}_{\text{Energy in}} + \Phi'_{TE} + \Phi'_{LE} = \underbrace{\rho c_p \left( Q_{LE}^i T_{LE}^i + Q_{SL}^i T_{SL}^i \right)}_{\text{Energy out}} \quad (30)$$

Above,  $\rho$  and  $c_p$  are the density and specific heat of the lubricant. Finally, from Eq. (30) the  $i^{th}$  pad leading edge temperature ( $T_{LE}^i$ ) is

$$T_{LE}^i = \frac{Q_{TE}^{i-1} T_{TE}^{i-1} + Q_{sup}^i T_{sup} - Q_{SL}^i T_{SL}^i + Q_{gr}^i T_{gr}^i + \frac{\Phi'_{TE} + \Phi'_{LE}}{\rho c_p}}{Q_{LE}^i} \quad (31)$$

#### 4.5 Elastic pad thermally induced deformation

Deformation of bearing components alters the film thickness and influences the bearing static and dynamic load performance. These deformations consist of a mechanical deformation due to hydrodynamic pressure and a thermally induced deformation due to temperature rise on the pads, shaft, and bearing housing. San Andrés and Li [23] modeled pad mechanical deformation using a three-dimensional finite element structure. The



current work extends their model to include thermally induced deformations of a pad in TPJBs.

Here, analytical methods are derived which closely approximate a three-dimensional FEM for thermally induced deformation of a pad. The major assumptions for the derivation are: a negligible thermally induced stresses in the pad, and the total radial deformation is superimposed (calculated separately) for the axial and circumferential cross sections.

Unlike mechanical deformation produced by the hydrodynamic pressure field on a pad, the thermal deformation depends on the boundary conditions of temperature and heat flow surrounding a pad and that greatly affect the pad ensuing deformed shape. However, the following analytical solution is less sensitive to the uncertainties with the existing two dimensional temperature field ( $T'_{(r,\theta)}$ ) in a pad (such as the assumed magnitude for  $h_{gr}$ ). The circumferentially averaged temperatures at the pad inner surface ( $T_p$ ) and back of the pad ( $T_{back}$ ) are

$$T_p = \frac{1}{\theta_{pad}} \int_{\theta_{LE}}^{\theta_{TE}} T'_{(R_p,\theta)} d\theta \quad (32)$$

$$T_{back} = \frac{1}{\theta_{pad}} \int_{\theta_{LE}}^{\theta_{TE}} T'_{(R_{back},\theta)} d\theta \quad (33)$$

The above temperatures create an equivalent radial temperature field in the pad, suitable for the following analytical method. With the averaged temperature on the pad inner surface ( $T_p$ ) and back surface ( $T_{back}$ ), an equivalent radial temperature distribution  $\bar{T}_{(r)}$  within the pad is defined as,

$$\bar{T}_{(r)} = \frac{T_p - T_{back}}{\ln\left(\frac{R_p}{R_{back}}\right)} \ln\left(\frac{r}{R_p}\right) + T_p \quad (34)$$

The corresponding temperature rise ( $\Delta\bar{T}$ ) from the reference temperature ( $T_{ref}$ ) is defined

by

$$\Delta\bar{T} = a \ln\left(\frac{r}{R_p}\right) + b \quad \text{where} \quad a = \frac{T_p - T_{back}}{\ln\left(\frac{R_p}{R_{back}}\right)}, \quad \text{and} \quad b = T_p - T_{ref} \quad (35)$$

The total strain at each point of a heated body consists of two parts. The first part is a uniform expansion proportional to the temperature rise ( $\Delta\bar{T}$ ). This expansion is identical in all directions for an isotropic body, arising only a normal strain and no shearing strain. The normal strain in any direction equals to ( $\alpha \times \Delta\bar{T}$ ), with  $\alpha$  as the material coefficient of thermal expansion. The second part consists of the strains that maintain the continuity of the body as well as those that arise because of external mechanical loads [54].

A curved beam of constant rectangular cross section models the pad subject to the radial temperature distribution across its thickness. Figure 13 shows the local polar coordinate system defined for a pad. The local angle ( $\hat{\theta}$ ) is similar to the angle used for the bearing cylindrical coordinates ( $\theta$ ), except that it starts from the pivot location on each pad ( $\hat{\theta} = \theta - \theta_{piv}^i$ ).

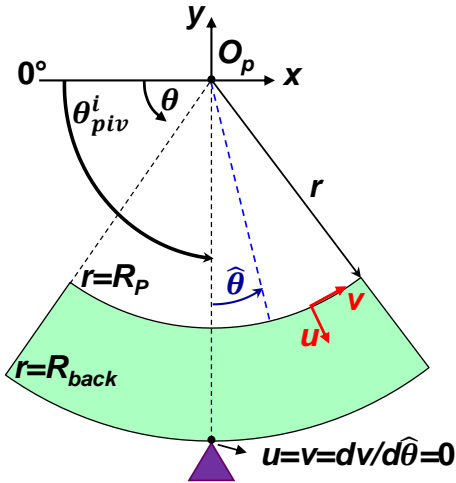


**Figure 13: Definition of a pad local coordinate system and deformations ( $u$ ,  $v$ ) along radial and circumferential directions.**

Let  $u$  and  $v$  be the deformation of a body in the radial and circumferential directions,

respectively. Timoshenko and Goodier [55] define the strain components  $(\epsilon_r, \epsilon_{\hat{\theta}}, \gamma_{r\hat{\theta}})$  in polar coordinates as,<sup>8</sup>

$$\epsilon_r = \frac{\partial u}{\partial r} \quad (36a)$$

$$\epsilon_{\hat{\theta}} = \frac{u}{r} + \frac{\partial v}{r\partial\hat{\theta}} \quad (36b)$$

$$\gamma_{r\hat{\theta}} = \frac{\partial u}{r\partial\hat{\theta}} + \frac{\partial v}{\partial r} - \frac{v}{r} \quad (36c)$$

These expressions for the strain component can be substituted into the generalized equations of Hooke's law for plane stress<sup>9</sup> as,

$$\epsilon_r = \frac{1}{E}(\sigma_r - \nu\sigma_{\hat{\theta}}) + \alpha\Delta\bar{T} \quad (37a)$$

$$\epsilon_{\hat{\theta}} = \frac{1}{E}(\sigma_{\hat{\theta}} - \nu\sigma_r) + \alpha\Delta\bar{T} \quad (37b)$$

$$\gamma_{r\hat{\theta}} = \frac{1}{G}\tau_{r\hat{\theta}} \quad (37c)$$

Note that no shearing stress arises due to a change in temperature.

As explained in detail in Appendix A, the magnitude of strain due to thermal stress terms  $(\sigma_r, \sigma_{\hat{\theta}}, \tau_{r\hat{\theta}})$  in Eq. (37) is negligible compared to the strain due to thermal expansion term  $(\alpha\Delta\bar{T})$ . Thus, neglecting the strain terms induced by internal thermal stresses, Eq. (37) reduces to,

$$\epsilon_r = \alpha\Delta\bar{T} \quad (38a)$$

$$\epsilon_{\hat{\theta}} = \alpha\Delta\bar{T} \quad (38b)$$

$$\gamma_{r\hat{\theta}} = 0 \quad (38c)$$

<sup>8</sup>This section follows the general method to find the displacements for symmetrical stress distribution in Ref. [55], page 77.

<sup>9</sup>This method holds for both plane stress and plane strain assumptions since the thermal stresses are neglected.

Substituting the radial and circumferential strains from Eq. (38) into Eq. (36) and integrating yields,

$$u_{(r,\hat{\theta})} = \int \epsilon_r dr + f_{1(\hat{\theta})} = \alpha r \left( a \ln \left( \frac{r}{R_p} \right) - a + b \right) + f_{1(\hat{\theta})} \quad (39a)$$

$$v_{(r,\hat{\theta})} = \int (r\epsilon_{\hat{\theta}} - u) d\hat{\theta} + f_{2(r)} = \alpha ar\hat{\theta} - \int f_{1(\hat{\theta})} d\hat{\theta} + f_{2(r)} \quad (39b)$$

in which  $f_{1(\hat{\theta})}$  is a function of  $\hat{\theta}$  only, and  $f_{2(r)}$  is a function of  $r$  only. Substituting Eq. (39) into Eq. (36c) and noting that  $\gamma_{r\hat{\theta}}$  is nil, then,

$$\frac{df_{2(r)}}{dr} - \frac{1}{r} f_{2(r)} = -\frac{1}{r} \frac{df_{1(\hat{\theta})}}{d\hat{\theta}} - \frac{1}{r} \int f_{1(\hat{\theta})} d\hat{\theta} \quad (40)$$

The above equation can only be obtained for symmetrical stresses<sup>10</sup>. For a non-symmetric stress distribution (i.e. a point load at one end) terms that are function of both  $r$  and  $\hat{\theta}$  would not cancel out and the following method, namely separation of variables, cannot be used. In the current method the stresses are zero and hence symmetric.

Since  $f_{1(\hat{\theta})}$  and  $f_{2(r)}$  are respectively functions of  $r$  and  $\hat{\theta}$  only, Eq. (40) is written as,

$$\frac{df_{2(r)}}{dr} - \frac{1}{r} f_{2(r)} = A_0 \quad (41a)$$

$$-\frac{1}{r} \frac{df_{1(\hat{\theta})}}{d\hat{\theta}} - \frac{1}{r} \int f_{1(\hat{\theta})} d\hat{\theta} = A_0 \quad (41b)$$

Solving the ordinary differential equations above yields,

$$f_{2(r)} = A_0 (\ln r + A_1) r \quad (42a)$$

$$f_{1(\hat{\theta})} = A_0 + A_2 \sin \hat{\theta} + A_3 \cos \hat{\theta} \quad (42b)$$

---

<sup>10</sup>Both  $\sigma_r$  and  $\sigma_{\theta}$  must be independent of  $\theta$ , and only a function of  $r$ .

where the end conditions of the curved beam determine the constants  $A_0, A_1, A_2,$  and  $A_3$ . By representing the pivot as a fixed point, one can use a local polar coordinate for each pad with  $\hat{\theta} = 0$  at the pivot. Thus, the boundary conditions become

$$\text{at the pivot } \hat{\theta} = 0 \text{ and } r = R_{back}: u = v = \frac{\partial v}{\partial r} = 0 \text{ (no deformation)}$$

Applying these boundary conditions to Eq. (39), the constants become

$$A_3 = \alpha R_{back} \left[ a \ln \left( \frac{R_{back}}{R_p} \right) - a + b \right], \text{ and } A_0 = A_1 = A_2 = 0$$

Hence, the radial and circumferential displacements  $(u, v)$  of a pad are

$$u_{(r,\hat{\theta})} = -\alpha \left[ a R_{back} \ln \left( \frac{R_{back}}{R_p} \right) \cos \hat{\theta} - ar \ln \left( \frac{r}{R_p} \right) + (r - R_{back} \cos \hat{\theta})(a - b) \right] \quad (43a)$$

$$v_{(r,\hat{\theta})} = \alpha \left[ a R_{back} \ln \left( \frac{R_{back}}{R_p} \right) \sin \hat{\theta} - R_{back}(a - b) \sin \hat{\theta} + ar \hat{\theta} \right] \quad (43b)$$

where  $a$  and  $b$  are constants specified from the thermal boundary conditions defined in Eq. (35). Recall, the radial deformation of the inner surface at the mid-plane ( $u_{(R_p,\hat{\theta})}$ ) modifies the film thickness.

Figure 14 shows a schematic view of the pad deformation along its length (axial direction). Existing analyses customarily neglect pad thermal warping along the axial direction in a two dimensional deformation analysis. The following explains an approximate method to account for the axial deformation of a pad.

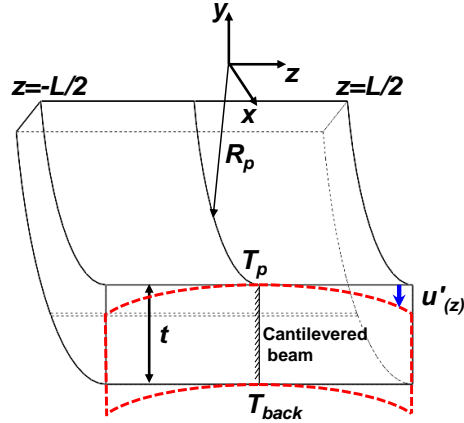


**Figure 14: Definition of an assumed cantilevered beam to approximate pad warping along the axial direction.**

A pad does not have a curvature along the axial ( $z$ ) direction, so it is modeled by an Euler beam, cantilevered at the mid plane, subjected to the stated temperature boundary condition ( $T_p, T_{back}$ ). The assumed Euler beam bends in the axial direction due to the temperature gradient. The assumed beam length is 50% of the pad length ( $L/2$ ). Using a general method in Ref. [56], the axial thermal warping as a function of axial distance ( $z$ ) to the mid-plane becomes,

$$u'_{(z)} = \alpha \frac{T_p - T_{back}}{2t} z^2 \quad \text{for } \frac{-L}{2} < z < \frac{L}{2} \quad (44)$$

Finally, the deflection of the inner surface of the pad ( $\delta_{(\hat{\theta}, z)}$ ) along the radial direction is defined as the superposition of deformation in the circumferential and axial cross sections,

$$\delta_{(\hat{\theta}, z)} = u_{(R_p, \hat{\theta})} + u'_{(z)} \quad (45)$$

Figure 15 shows the radial deformation of a pad inner surface from this method in comparison with the results from a three-dimensional structural FE pad model. The geometry of the pad is taken from Coghlan, Ref. [4]. The inner radius of the pad ( $R_p$ ) is 0.051 m,

the outer radius ( $R_{back}$ ) is 0.07 m, and the pad axial length ( $L$ ) is 0.061 m. The pad material thermal expansion coefficient ( $\alpha$ ) is  $1.3 \times 10^{-5} 1/^\circ\text{C}$ , and the temperature boundary conditions for the inner and back surfaces are respectively  $T_p = 80^\circ\text{C}$ ,  $T_{back} = 72^\circ\text{C}$ . The reference temperature is  $T_{ref} = 21^\circ\text{C}$ . One can observe that the results from the analytical model approximates the three dimensional deformation field closely. However, note that the FEM results are for a pad with a radial temperature distribution, and the deformation due to three-dimensional temperature distribution in the pad might differ slightly.

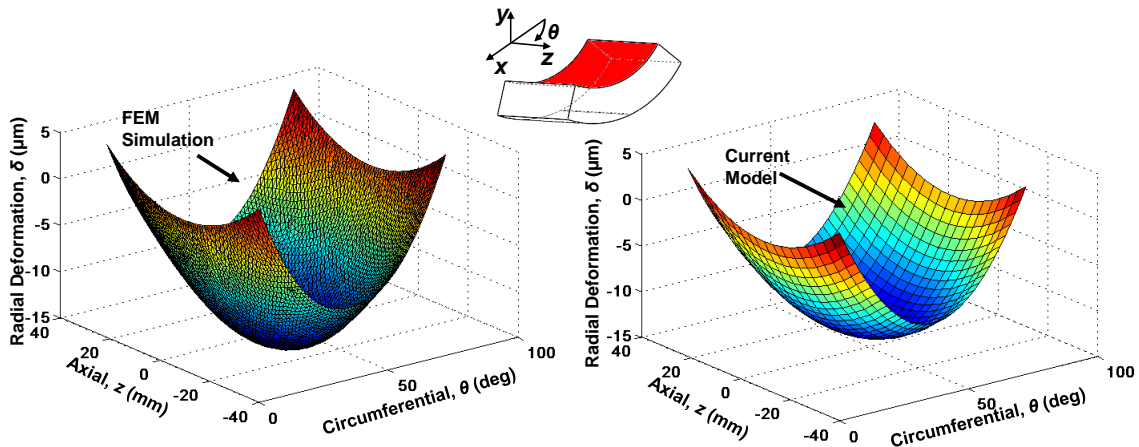


**Figure 15: Pad inner surface thermally induced deformation. Comparison of results from the current analytical method (right) versus 3D FEM (left). Reference geometry taken from Ref. [3]**

#### 4.6 Shaft expansion and housing expansion

Accurate modeling of the shaft thermally induced deformation requires the solution of the temperature field for the entire shaft structure. Similarly, the bearing housing installation type and the operating conditions determine the temperature field in the bearing housing. Therefore, the thermal expansion of shaft OD and housing ID is modeled using

a simple one-dimensional formula, i.e.,

$$\Delta R_s = \alpha_s R_s (T_s - T_{ref}) \quad (46a)$$

$$\Delta R_h = \alpha_h R_h (T_h - T_{ref}) \quad (46b)$$

where  $\alpha_s$  and  $\alpha_h$  are the shaft and housing material thermal expansion coefficient. Above, the subscripts  $s$  and  $h$  denote shaft OD and housing ID, respectively.

The shaft temperature is either imposed or calculated as the average of film temperature throughout the bearing. The temperature measurements from Coghlan [4] show that the housing temperature is very close to the oil discharge temperature. Presently, the model takes the sump (discharge) temperature as the housing temperature ( $T_{sump}$ ).

Contrary to the shaft that only expands outward, the housing expansion or contraction depends on its installation condition. If the housing is free (such as in some test rigs), it expands outward. Alas for most practical cases, the housing contracts as it is firmly affixed or press inserted into a pedestal, for example.

#### 4.7 Hot clearance estimation

A geometric model estimates the change in the pad clearance and bearing clearance due to both mechanical and thermally induced deformations. After the calculation of pad deformations a new origin ( $O'_p$ ) is found for the deformed pad. New pad clearance is based on new pad radius ( $R'_p$ ) and expansion of the shaft and bearing housing.

Figure 16 (left) shows the circumcenter of a triangle<sup>11</sup> on a pad inner surface formed by the leading edge, pivot location, and trailing edge points. Each side of this triangle is a chord of the circumcircle. Figure 16 (right) shows the thermally induced deformed

---

<sup>11</sup>The point at which the perpendicular bisectors of the sides of a triangle intersect and which is equidistant from the three vertices. The perpendicular bisector of a segment is a line that is perpendicular to the segment, and intersects with the midpoint of the segment.



shape of a pad. The model finds the midpoint of the line segments that connect the trailing edge and leading edge to the pivot. Then it determines the slopes of these segments, and the slopes of their perpendicular bisectors. This gives enough information to state the geometric relation of the two perpendicular bisectors. The intersection of these lines is the deformed pad arc center, and the new pad radius ( $R'_p$ ) is calculated with respect to this point.

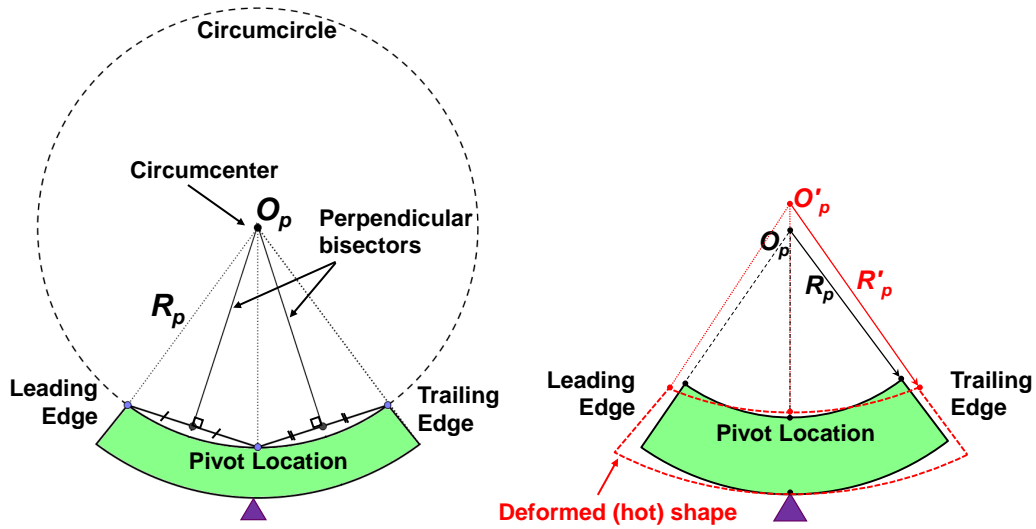


Figure 16: *Left:* Circumcenter of a pad, *Right:* Thermal deformation of a pad, includes the effects of thermal expansion and warping.

The new bearing radius ( $R'_b$ ) is the difference between the deformed pivot location on the inner surface and the bearing origin. New pad and bearing clearances with the contributions of the pad, shaft, and housing deformations are

$$C'_p = R'_p - R_s - \Delta R_s + \Delta R_h \quad (47a)$$

$$C'_b = R'_b - R_s - \Delta R_s + \Delta R_h \quad (47b)$$

Thus the new preload becomes,

$$m' = \frac{C'_p - C'_b}{C'_p} = \frac{R'_p - R'_b}{R'_p - R_s - \Delta R_s + \Delta R_h} \quad (48)$$

Note that the pad clearances calculated from this method are larger than the actual deformed shape clearance because of the assumption that deformed pad inner surface remains circular. To calculate the film thickness (Eq. (5)) the deformation field of the pad surface ( $\delta_{(\hat{\theta}, z)}$ ) and changes in shaft and housing radius ( $\Delta R_s, \Delta R_h$ ) are used separately.

## 5 COMPARISON OF PREDICTIONS AGAINST TEST DATA

### 5.1 Large TPJB operating at a high surface speed and heavy load

Hagemann et al. [1] use a rig designed to test large size journal bearings for steam turbines. The maximum bearing diameter is 500 mm (0.5 m) and its length is 500 mm. The drive power (1.2 MW) enables operation with a shaft speed up to 4,000 RPM ( $\Omega R_s = 105$  m/s). Spray bars deliver fresh (cold) lubricant to a test bearing. Two sealing baffles with a clearance of 1 mm ( $C/R_s = 0.004$ ) at the axial ends of the bearing reduce the required supply flow rate to induce a flooded condition [1]. During the tests, the hollow rotating shaft with two piezoelectric pressure sensors and two capacitive displacement sensors is shifted axially to record the film thickness and pressure distribution over the full extent of the pad surfaces.

Table 1 outlines the geometry, lubricant properties, and operating conditions of one test bearing. Figure 17 shows a schematic view of the bearing and the load direction. For this test bearing, the length to diameter ( $L/D$ )=0.7 and pad clearance to radius ratio ( $C_p/R_s$ )=0.0012. Rocker back pivots, arched in the axial direction, enable the pads to also roll axially and reduce the influence of misalignment. Ref. [2] does not provide the pivot stiffness, however based on the geometry, the pivot stiffness is approximated using Hertz contact theory for a cylinder on a cylinder. The maximum applied load on the bearing is 1 MN. The specific load ( $W/(LD)$ ) ranges between 1 MPa and 2.5 MPa. Also, the large diameter of the rotor gives a surface speed between 13 m/s and 79 m/s for shaft speeds from 500 RPM to 3,000 RPM.

The measurements along with the predictions from a computational model in Refs. [1, 2] are compared against the predictions obtained from the current model. Unless otherwise noted, the following predictions are obtained accounting for the thermally and pressure induced deformation of the bearing components (TEHD model).

**Table 1: Characteristics of a test TPJB. From Hagemann et al. [1]**

<b>Bearing properties</b>	
Load orientation	LBP
Number of pads	5
Shaft diameter [mm]	500
Pad thickness [mm]	72.5
Bearing axial length [mm]	350
Pad arc length	56°
Pivot offset	0.6
Pad clearance [ $\mu\text{m}$ ]	300
Preload	0.23
Pad mass* [kg]	55.9
Pad moment of inertia about pivot point* [ $\text{kg}\cdot\text{m}^2$ ]	0.44
Pivot Stiffness* [N/m]	Hertz ( $\sim 3 \text{ GN/m}$ )
<b>Operating condition</b>	
Load [kN]	175–438
Specific Load $W/(LD)$ [MPa]	1–2.5
Shaft rotational speed [RPM]	500–3000
Shaft surface speed $\Omega R$ [m/s]	13–79
Lubricant supply temperature [ $^{\circ}\text{C}$ ]	50
Lubricant flow rate [L/min]	210 / 420
<b>Fluid properties</b>	
Lubricant	ISO VG32
Viscosity at supply temperature* [mPa·s]	22.4
Viscosity temperature coefficient* [ $1/^{\circ}\text{C}$ ]	0.0297
Density [ $\text{kg}/\text{m}^3$ ]	844
Specific heat capacity [kJ/(kg·K)]	2.17
Thermal conductivity [W/(m·K)]	0.13
Lubricant supply method	Spray-bar, Flooded
<b>Thermal properties</b>	
Pad and journal thermal conductivity [W/(m·K)]	45
Sump temperature [ $^{\circ}\text{C}$ ]	65
Housing direction of expansion*	Outwards
Groove efficiency, $C_{gr}$ (assumed for flooded)	0.2

\*Assumed based on the data in Ref. [1].

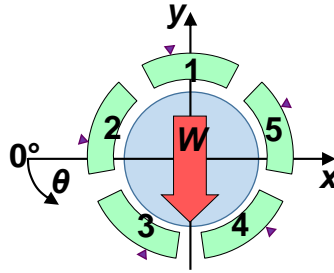


**Figure 17: Schematic view of a five-pad TPJB in Ref. [1].**

Figure 18 shows the pad surface temperature rise relative to the supply temperature ( $50^{\circ}\text{C}$ ) versus angle ( $\theta$ ). The measured pad temperatures are recorded using thermocouples located 5 mm behind the pad inner surface [1]. The novel thermal mixing flow model deliver results that are in good agreement with the test data, in particular for the unloaded pads.

The current model improves the simple (conventional) model (Eq. (1), page 4) predictions up to  $17^{\circ}\text{C}$  by accounting for the reduced supply flow rate in the test. The groove efficiency ( $C_{gr}$ ) is selected<sup>12</sup> as 0.2 since the bearing is flooded and a large portion of hot oil upstream of each groove presumably churns in the groove. Hence, the temperature of the recirculating lubricant in the groove ( $T_{gr}$ ) is closer to the upstream temperature ( $T_{TE}$ ) than to the oil supply temperature ( $T_{sup}$ ).

<sup>12</sup>Refer to Eqs. (25) and (27) (page 37) for description of the groove efficiency parameter.

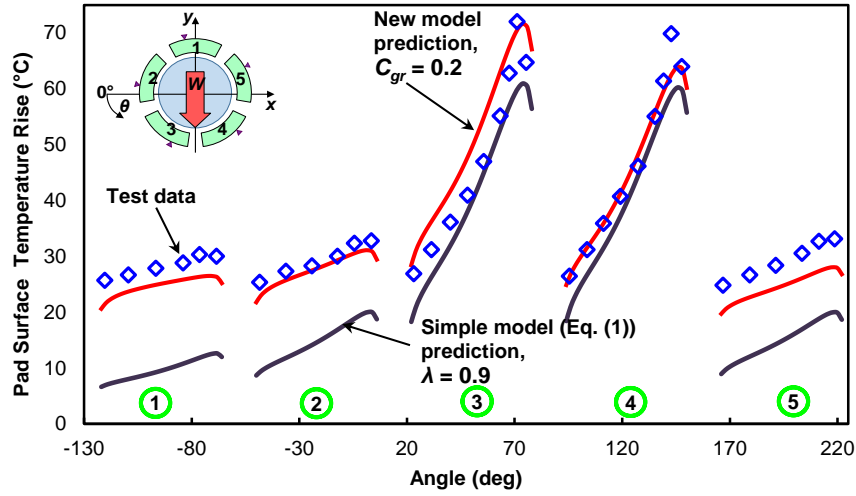


**Figure 18: Pads' surface temperature rise versus circumferential location. Predictions from current and old mixing models compared against test data in Ref. [1]. (Spray Bar, Flooded,  $T_{sup}= 50^{\circ}\text{C}$ ,  $N=3000$  RPM,  $W/(LD)=2.5$  MPa, and  $C_{gr}=0.2$ )**

Table 2 compares the predicted flow rates from the current and simple (early) thermal mixing models. The amount of flow needed to make up for the difference between the downstream flow ( $Q_{LE}$ ) and the upstream flow ( $Q_{TE}$ ) in the two models is almost the same<sup>13</sup>.

**Table 2: Flow rates [L/min] in the feeding grooves of the bearing in Ref. [1]. Predictions from current model and simple (early) model. (Spray Bar, Flooded,  $N=3000$  RPM, and  $W/(LD)=2.5$  MPa,  $\lambda=0.9$ ,  $C_{gr}=0.2$ )**

Pad	$Q_{TE}^{i-1}$ $Q_{LE}^i$ (L/min)		$\alpha_i$	Current Model $Q_{sup}^i$ $Q_{SL}^i$ $Q_{gr}^i$ (L/min)			Simple Model $Q_{sup}^i$ (L/min)
	1	177		468	0.24	102	0
2	253	294	0.15	62	21	0	76
3	171	112	0.11	45	105	0	0
4	44	123	0.19	81	2	0	83
5	53	299	0.31	129	0	116	254
Total:			1.0	420 (L/min)=Test			713 (L/min)

<sup>13</sup>The predicted  $Q_{LE}$ ,  $Q_{TE}$  are only slightly different in the two models which is due to an altered viscosity from different predicted film temperatures.

The simple (early) model assumes make up flow only contains supply (fresh) lubricant ( $Q_{sup}$ ). The current model adds the churning oil in the groove ( $Q_{gr}$ ) and side leakage flow ( $Q_{SL}$ ) to the components of the make up flow.

$$\text{Current model:} \quad Q_{LE} - Q_{TE} = Q_{sup} - Q_{SL} + Q_{gr} \quad (49a)$$

$$\text{Simple model:} \quad Q_{LE} - \lambda Q_{TE} = Q_{sup} \quad (49b)$$

The simple (early) model predicts  $Q_{sup}^{total} = 713$  L/min, 70% larger than the actual flow rate during the operation that is equal to 420 L/min [1]. The present model allocates a percentage of the actual flow rate (420 L/min) to each groove based on the approximate flow fraction ( $\alpha_i$ ) from Eq. (20). The rest of the lubricant required to fill in the pad inlet film thickness is drawn from recirculating lubricant in the groove ( $Q_{gr}, T_{gr}$ ).

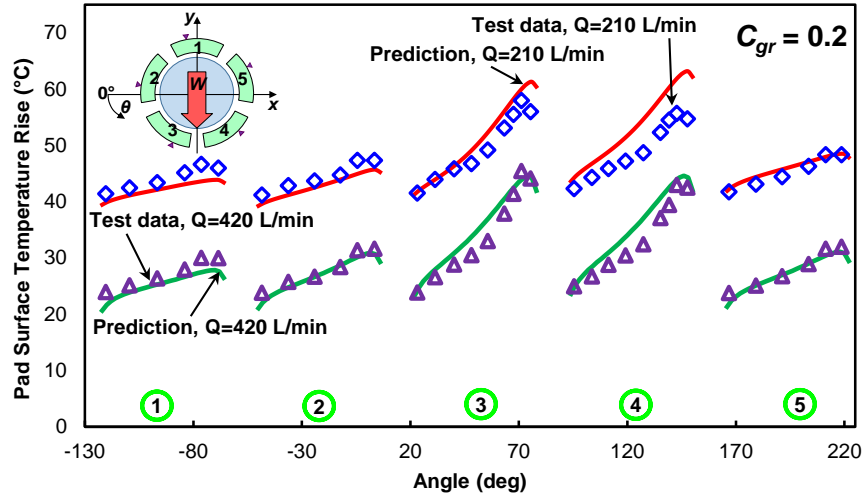
Nicholas et al. [57] state that in a flooded TPJB design with a pressurized housing (not evacuated) “any additional oil that may be required is simply drawn from the captured oil inside of the bearing housing”. Since the example bearing is flooded, a significant portion of the lubricant that leaves each *pad* (side or axially) is not immediately forced out of the bearing. Instead, it recirculates in the housing and provides the additional fluid required to fill in the film ( $Q_{gr}$ )<sup>14</sup>. Note that the simple model predicts a nil draw of supply lubricant for pad ③, whereas the novel model predicts a significant side leakage flow ( $Q_{SL}$ ) that discharges sideways off the groove.

Figure 19 shows the predicted pad inner surface temperature for two supply flow rates with operation at a shaft speed of 3,000 RPM and under a specific load of 1 MPa. Reducing the total supply flow rate means that more lubricant would be drawn from the grooves (larger  $Q_{gr}$ ). While this is the case for a flooded bearing, excessive reduction in supply

---

<sup>14</sup>A flooded bearing requires less total (overall) supply oil compared to an evacuated one, since in an evacuated bearing all required lubricant must be solely supplied by the feed orifices (no recirculating flow). [57]

flow in an evacuated bearing induces oil starvation due to a lower availability of excess oil in the housing [57]. Note specifically the leading edge temperature for all of the examples and which correlates well with the test data.



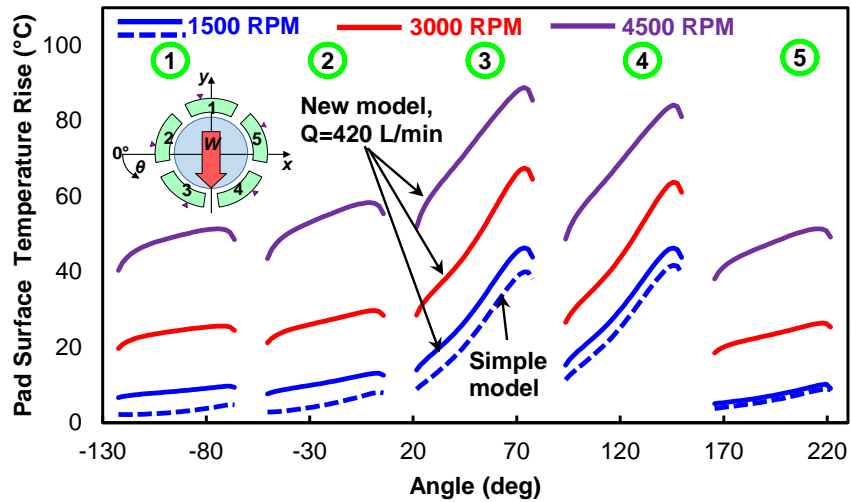
**Figure 19: Pads' surface temperature rise versus circumferential location for two supply flow rates (210 L/min and 420 L/min). Predictions compared against test data in Ref. [1]. (Spray Bar, Flooded,  $T_{sup}= 50^{\circ}\text{C}$ ,  $N=3000$  RPM,  $W/(LD)=1$  MPa,  $C_{gr}=0.2$ )**

Figure 20 compares temperatures predicted from the two thermal mixing models for operation at three shaft speeds. The predictions from the present mixing model keep the total supply flow rate constant ( $Q_{sup}^{total} = 420$  L/min), whereas the early thermal mixing model predicts  $Q_{sup}^{total} \approx 700, 1100, \text{ and } 1650$  L/min respectively for  $N = 1500, 3000, \text{ and } 4500$  RPM. The predicted temperatures from the simple model are within  $10^{\circ}\text{C}$  of each other and only one for  $N = 1500$  RPM is shown. The predictions from the current model show a substantial increase in pad surface temperature with an increase in shaft speed.

The current model predictions for  $N = 3000$  RPM are compared with test data shown in Figure 18. For a higher speed ( $N = 4500$  RPM), however, the results may not be accurate since the amount of required groove flow ( $Q_{gr}$ ) becomes very large and there may not be enough lubricant left (churning) in the bearing housing to provide it. In this situation, the full arc extent of the pads would not be lubricated which could induce oil



starvation in one or more pads.



**Figure 20: Pads' surface temperature rise versus angle for operation at three shaft speeds. (Spray Bar, Flooded,  $T_{sup}= 50\text{ }^{\circ}\text{C}$ ,  $N=1500, 3000, 4500\text{ RPM}$ ,  $W/(LD)=2.5\text{ MPa}$ ,  $C_{gr}=0.2$ , and  $\lambda=0.8$ )**

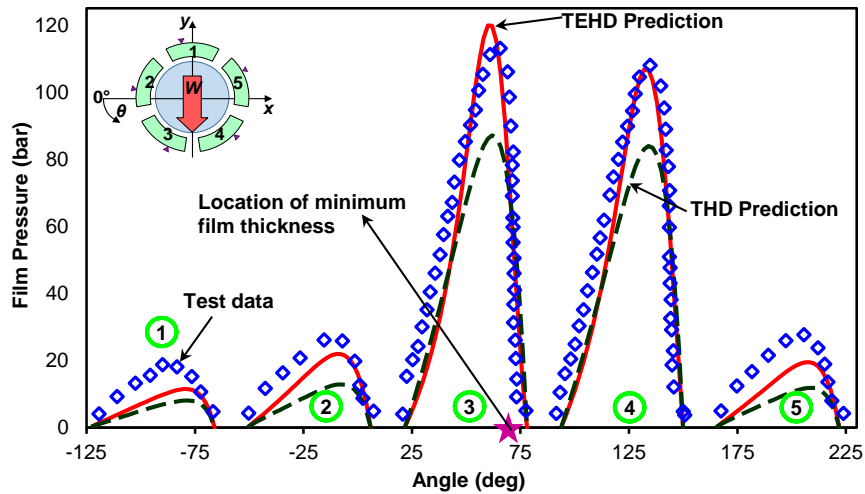
Table 3 compares the journal eccentricity along the load direction ( $-e_y$ ) obtained with the novel thermal mixing model for both TEHD and THD model predictions<sup>15</sup>. The predicted journal eccentricity ( $e_x$ ) in the orthogonal direction and the journal attitude angle ( $\phi = \tan^{-1}(e_x/e_y)$ ) are insignificant thus not shown. Hagemann et al. [1] do not report the test data for these parameters. The predicted journal eccentricity in the load direction delivered by the TEHD analysis is 25% to 30% smaller than that from the THD analysis. The difference decreases as the load increases since the eccentricity grows to nearly reach the cold (machined) pad clearance (300  $\mu\text{m}$ ).

<sup>15</sup>In the following figures, 'TEHD' denotes thermoelastohydrodynamic, and 'THD' notation represents thermohydrodynamic analysis, that neglects both the thermally and mechanically induced deformation in the bearing components. Both analyses include pivot flexibility.

**Table 3: TEHD and THD predictions for journal eccentricity in the load direction ( $-e_y$ ) for four specific loads. ( $N=3000$  RPM,  $C_{gr}=0.2$ )**

	$W/(LD)$ [MPa]	1	1.5	2	2.5
THD	$-e_y$ [ $\mu\text{m}$ ]	158	215	261	290
TEHD	$-e_y$ [ $\mu\text{m}$ ]	112	151	186	216

Figure 21 shows the hydrodynamic pressure in the mid-plane of the bearing. The TEHD analysis, including thermal and mechanical deformations, shows very good agreement with the measurements in Ref. [1]. Neglecting the thermally induced deformation leads to under-predicting the pressure field, in particular its peak magnitude. Note the peak pressure TEHD prediction is<sup>16</sup> 5% larger than the measured magnitude, whereas the THD prediction is 27% smaller. The predicted hydrodynamic pressure shows a similar discrepancy with the test data for the lightly loaded pads (1, 2, 5).



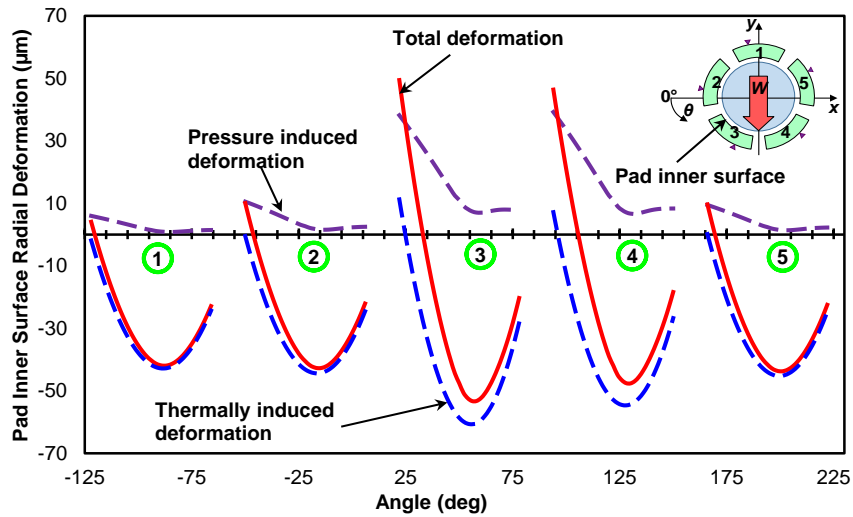
**Figure 21: TEHD and THD predictions for mid-plane film pressure compared against test data in Ref. [1]. Star symbol (★) shows the location of minimum film thickness. ( $N=3000$  RPM,  $W/(LD)=2.5$  MPa)**

Figure 22 shows the predicted thermal and pressure induced mechanical deformations (in the radial direction) on the bearing pads. The total deformation adds to the film thick-

<sup>16</sup>The percentage of prediction difference compared to measured magnitudes throughout this work is calculated from: %Difference=(Measured-Predicted)/Measured.

ness and modifies the performance of the TPJB. Observe that the thermal deformations are generally negative, which means the pads expand toward the center of the bearing, but they could be either positive or negative with a smaller absolute magnitude at the leading and trailing edges (due to the thermal warping of the pad). For a typical pad, the thermal expansion and warping are closely related to the pad thickness and arc length. For an identical temperature gradient, thick and short pads tend to expand more, whereas slender and long pads predominantly warp.

In Figure 22, pressure induced (surface) deformations are always positive due to the opening up of the pad curvature. For the highest loaded pads (3, 4) the pressure induced deformation is considerable, and the maximum total deformation is slightly more than 20% of the cold pad clearance ( $C_p = 300 \mu\text{m}$ ). Recall, the pivot offset (0.6) causes an asymmetry in the deformations, with their minimum located at the pivot location.



**Figure 22: Predicted pads' inner surface deformation along the radial direction. Positive magnitude denotes (outward) expansion, while negative magnitude denotes (inward) contraction. ( $N=3000$  RPM,  $W/(LD)=2.5$  MPa)**

Figure 23 shows the film thickness at the mid-plane of the bearing. The TEHD model including the thermal expansion of the pads, shaft, and bearing housing delivers a smaller film thickness compared to that from the THD model. TEHD predictions have a slightly

better agreement with test data for the minimum film thickness, about 10  $\mu\text{m}$ . However, the THD predictions do not accurately predict the slope of the film thickness with a significant difference (up to 45%) at the leading edge of the loaded pads (3, 4). This is directly due to the pressure induced deformation (opening up) of these pads (due to the applied load).

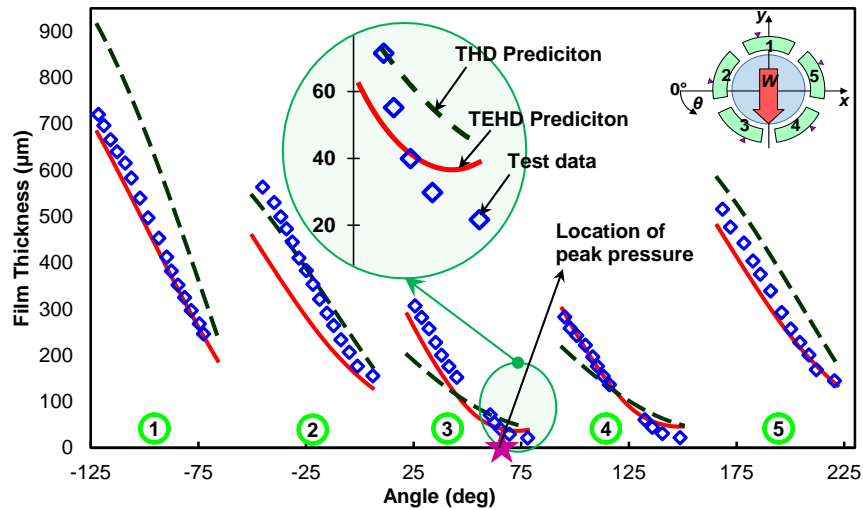


**Figure 23: TEHD and THD predictions for mid-plane film thickness compared against test data in Ref. [1]. Star symbol (★) shows the location of peak pressure. ( $N=3000$  RPM,  $W/(LD)=2.5$  MPa)**

Figure 24 shows the axial variation of the film pressure at the circumferential location where the peak hydrodynamic pressure on pad (3) occurs. Including the thermally induced deformation causes a considerable increase in peak film pressure, and a better agreement with test data. The peak pressure develops shortly before the minimum film thickness, at  $\theta = 62^\circ$  on pad 3 (see ★ in Figure 21)

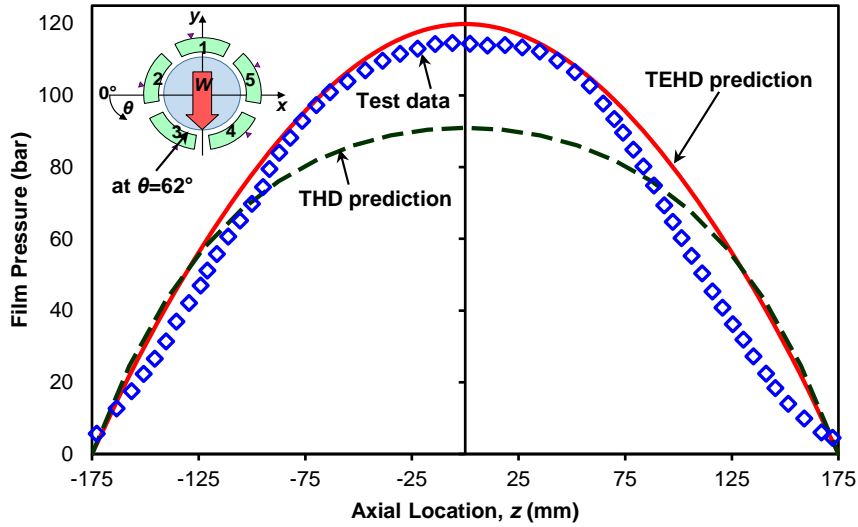


**Figure 24: Predicted and measured film pressure at the circumferential location of peak pressure ( $\theta=62^\circ$ , see Figure 21). TEHD and THD predictions compared against test data in Ref. [1]. ( $N=3000$  RPM,  $W/(LD)=2.5$ )**

Figure 25 shows the axial variation of the oil film at its minimum thickness location, shortly downstream of the peak pressure location ( $\theta=74^\circ$ , see ★ in Figure 23). While prior research typically neglects the axial deformation of a pad, the test data show that this deformation is significant. Modeling the axial deformations with a cantilevered beam approximates the actual deformations with accuracy. Note also that the axial arch of the test bearing pivots contributes to the axial deformation of the pads.

The predicted film thickness at  $z = \pm 1/2L$  is about  $25 \mu\text{m}$  lower than the measured magnitude which is about 8% of the cold pad clearance ( $300 \mu\text{m}$ ). However, the axially averaged film thickness from the test data ( $49 \mu\text{m}$ ) is very close to the one from the predictions ( $44 \mu\text{m}$ ) which explains the accurate hydrodynamic pressure predictions.

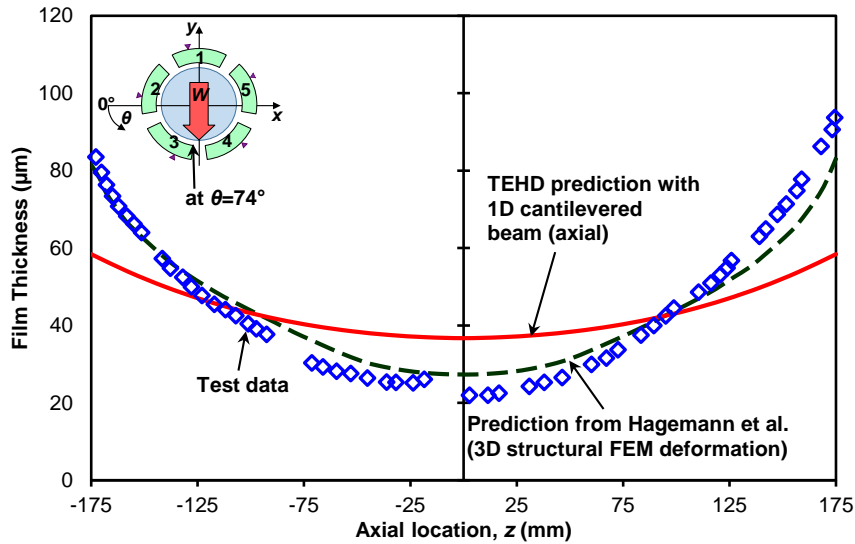


**Figure 25: Predicted and measured film thickness in the circumferential location of the minimum film thickness ( $\theta=74^\circ$ , see Figure 23). Measured results in Ref. [1]. ( $N=3000$  RPM,  $W/(LD)=2.5$  MPa)**

Kukla et al. [2] perform tests in which two shakers (attached to the test rig) induce a harmonic force at a frequency close to shaft speed during operation. The authors then identify (and estimate) the bearing dynamic force coefficients by post-processing the measured hydrodynamic film pressure field on the pads. Ref. [2] uses a  $[K, C]$  model to describe the dynamic force coefficients of the TPJB, thus the predictions shown are reduced at a frequency equal to the shaft speed (synchronous). Kukla et al. state that the above procedure is well-established for fixed pad bearings, but its applicability to TPJBs is unclear [2].

Kukla et al. [2] do not provide a measured pivot stiffness, and only state that “due to the small elliptical area of the contact between the pad and the liner [housing], the pivot is very flexible.” Presently, the pivot stiffness is calculated based on Hertzian contact stress formula (see Ref. [58]) for a cylinder on cylinder arrangement, assuming (based on geometry in Ref. [2]) that the axial arc on the back of a pad limits the contact length to 10% of the pad’s axial length. Note the calculated pivot stiffness depends on load, but it is about 3 GN/m (for  $W/(LD) = 2.5$  MPa) and smaller than the predicted bearing direct

stiffnesses with rigid pivots (about 4 GN/m to 9 GN/m). Hence the resulting predicted dynamic coefficients rely heavily on the assumed pivot stiffness. See Ref. [22] for a detailed analysis of pivot flexibility effect on the rotordynamic force coefficients of a TPJB.

Figure 26 shows the predicted<sup>17</sup> direct stiffness coefficients for the test bearing compared to the measurements and predictions in Ref. [2]. Predicted cross-coupled stiffnesses from the current model are much smaller compared to the measured magnitudes and not shown. The direct stiffnesses ( $K_{xx}$ ,  $K_{yy}$ ) depend on the applied load; which for a given shaft speed they increase with an increase in load.

The current predictions and those from Ref. [2] are greater than the measured stiffness coefficients. The prediction and measurements show the bearing is stiffer in the static load direction, or  $K_{yy} > K_{xx}$ . Unlike the predictions, the test data show that stiffnesses reduce substantially for  $N = 3,000$  RPM compared to  $N = 1,500$  RPM. The stiffness orthotropy (difference between  $K_{yy}$  and  $K_{xx}$ ) in the test data increases when rotor speed increases from  $N = 1,500$  to  $3,000$  RPM. The current model and Ref. [2], however, predict that the direct stiffness orthotropy reduces for the high shaft speed (3,000 RPM).

The agreement of the current TEHD predictions and the measured bearing stiffness in the load direction ( $K_{yy}$ ) is very good. The maximum difference is less than 20% for operation at 1,500 and 3,000 RPM. In the orthogonal direction, the difference for  $K_{xx}$  is up to 17% for  $N = 1,500$  RPM. However, at the high speed (3,000 RPM) the predicted  $K_{xx}$  is twice the test data. Notably, an increase in shaft speed increases the estimated  $K_{yy}$  from test data, however sharply drops  $K_{xx}$  about 40%. This means shifting from an operation at  $N = 1500$  RPM to  $N = 3000$  RPM, the bearing stiffens along the load direction while it softens in the orthogonal direction.

---

<sup>17</sup>Accounting for thermoelastic deformations (TEHD) and using the novel thermal mixing model.

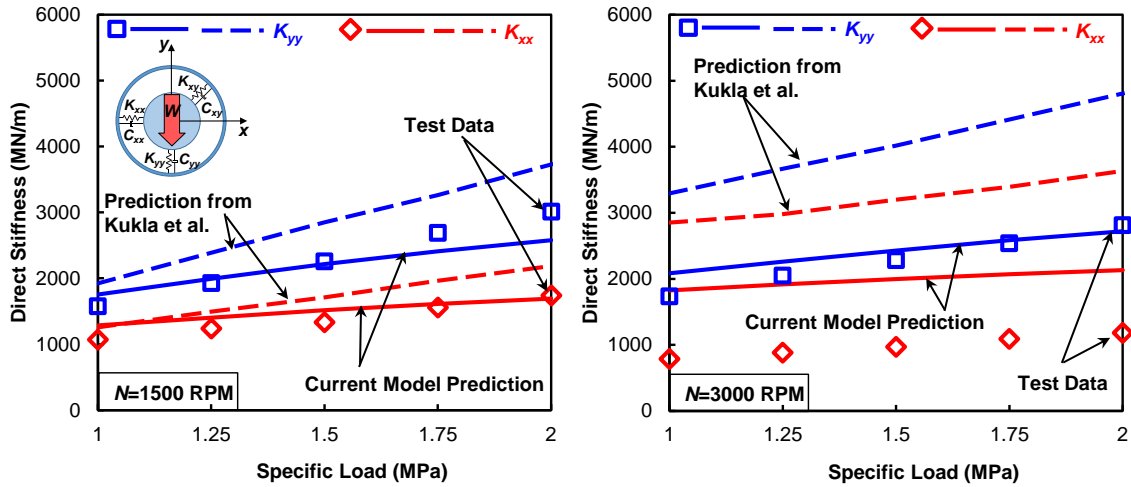
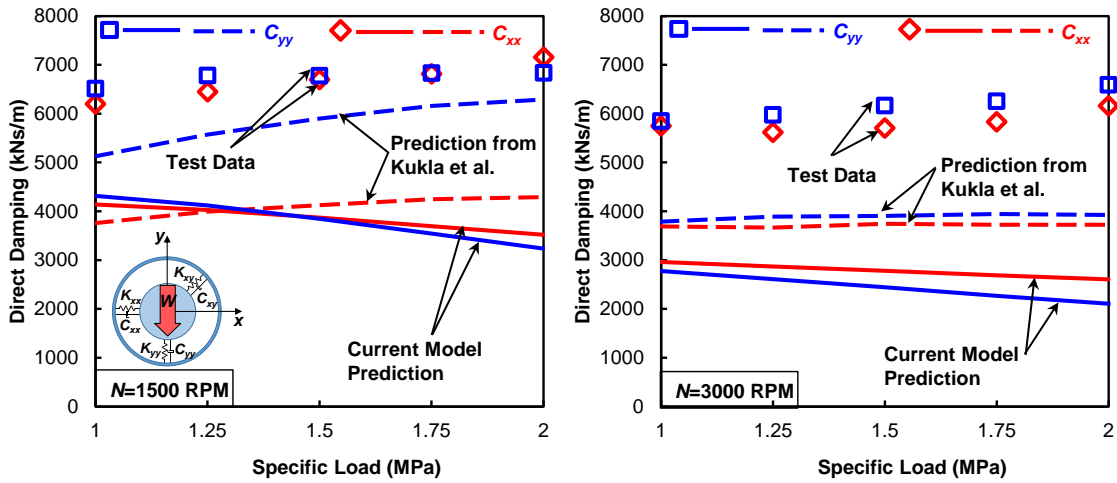


Figure 26: Direct stiffness coefficients ( $K_{yy}$ ,  $K_{xx}$ ) versus specific load for operation at two shaft speeds. TEHD prediction and test data in Ref. [2]. (Synchronous excitation; *Left*:  $N=1500$  RPM, *Right*:  $N=3000$  RPM)

Figure 27 shows the predicted direct damping coefficients ( $C_{xx}$ ,  $C_{yy}$ ) compared to the test data and predictions in Ref. [2]. Predicted cross coupled terms are one order of magnitude smaller than the test data and not shown. The predicted  $C_{xx}$ ,  $C_{yy}$  are consistently smaller than the estimated ones from test data. Contrary to the test data and predictions in Ref. [2], the current model predicts that the damping coefficients decrease with an increase in applied load. The current predictions have a considerable discrepancy with the test data; between 33% and 53% for  $N = 1,500$  RPM and between 48% and 68% for  $N = 3,000$  RPM. The flexible pivot with a stiffness smaller than the film stiffness is likely accountable for the significant reduction in the predicted bearing damping.





**Figure 27: Direct damping coefficients ( $C_{yy}$ ,  $C_{xx}$ ) for operation at two shaft speeds. Prediction and test data from Ref. [2]. (Synchronous excitation; *Left*:  $N=1500$  RPM, *Right*:  $N=3000$  RPM)**

The results above (Figures 26 and 27) are of interest due to the large deviation between the predictions and the test results. Kukla et al. [2] believe that no fundamental error occurred in their analysis or test procedure (although their predicted dynamic force coefficients do not correlate with their test data). The authors state the key problem in the test procedure is neglecting the pad inertia effects in determining the rotordynamic coefficients (assuming the fluid film force is always equal to the external force applied by the shakers). Based on the available geometry in Ref. [2], the pad mass and moment of inertia are notably large, respectively 55.9 kg and 0.44 kg·m<sup>2</sup>. Kukla et al. [2] also believe that neglecting the axial shifting of the shaft in the support bearings and its dynamic behavior may be responsible for the discrepancies.

## 5.2 Spherical seat TPJB under heavy specific load and high speed

Coghlan and Childs [3–5] conduct an extensive test program to study the effects of various lubrication (oil feed) configurations on the static and dynamic force performance of a spherical seat TPJB. Table 4 shows the characteristics of the test bearing in Ref. [4]. Figure 28 shows a schematic view of the bearing and the load direction.

The authors perform measurements for various lubrication delivery configurations,

1. Flooded single-orifice (SO), labyrinth end seals with nominal clearance of 170  $\mu\text{m}$
2. Evacuated leading edge groove (LEG), no end seals
3. Evacuated spray-bar (SB), no end seals
4. Evacuated spray-bar blocker (SBB), no end seals

Coghlan and Childs measure pad surface temperature (embedded in the babbitt layer), journal eccentricity, hot bearing clearances, and a complex stiffness for each feeding arrangement and for operation with a shaft speed ranging from 7,000 RPM and 16,000 RPM ( $\Omega R_s = 85\text{m/s}$ ), and under a specific load, 0.7 MPa to 2.9 MPa. The authors then curve fit a frequency independent ( $[K, C, M]$ ) model to the complex stiffness (impedance) data to determine the stiffness ( $K$ ), damping ( $C$ ), and virtual mass ( $M$ ) of the bearing in the load ( $y$ ), orthogonal ( $x$ ) directions.

The following predictions pertain to a TPJB with spray bars (SB) to deliver the supply oil and pad retainers instead of end seals to evacuate the housing from recirculating lubricant. Buffer seals prevent oil axial leakage from the test bearing into the adjacent support bearing chambers and guide it to oil outlet pipes. The authors selected (based on industrial practice) the location to measure the maximum temperature at 75% of the pad arc length. All thermocouples are type J with a measurement error of  $\pm 1.1$   $^{\circ}\text{C}$ .

**Table 4: Characteristics of a TPJB tested by Coghlan and Childs [4]**

<b>Bearing properties</b>	
Load orientation	LBP
Number of pads	4
Shaft diameter [mm]	101.59
Pad thickness [mm]	19
Bearing axial length [mm]	61
Pad arc length	72°
Pivot offset	0.5
Pad clearance (cold)[ $\mu\text{m}$ ]	134
Preload (cold)	0.3
Pad mass* [kg]	0.6
Pad moment of inertia about pivot point* [ $\text{kg}\cdot\text{m}^2$ ]	$4.6 \times 10^{-4}$
Pivot Stiffness [N/m]	$4.12 \times 10^8$
<b>Operating condition</b>	
Load [kN]	4.3 - 17.7
Specific Load $W/(LD)$ [MPa]	0.7–2.9
Shaft rotational speed [RPM]	7000–16000
Shaft surface speed $\Omega R$ [m/s]	38–85
Lubricant supply temperature [ $^{\circ}\text{C}$ ]	49
Lubricant flow rate [L/min]	38 (Flooded) / 42 (Evacuated)
<b>Fluid properties</b>	
Lubricant	ISO VG46
Viscosity at supply temperature [mPa·s]	25.6
Viscosity temperature coefficient [ $1/^{\circ}\text{C}$ ]	0.0431
Density [ $\text{kg}/\text{m}^3$ ]	843.5
Specific heat capacity [ $\text{kJ}/(\text{kg}\cdot\text{K})$ ]	2.084
Thermal conductivity [ $\text{W}/(\text{m}\cdot\text{K})$ ]	0.1243
<b>Thermal properties</b>	
Pad and journal thermal conductivity [ $\text{W}/(\text{m}\cdot\text{K})$ ]	52
Sump temperature [ $^{\circ}\text{C}$ ]	51–64
Housing direction of expansion*	Outwards
Shaft thermal expansion coefficient [ $1/^{\circ}\text{C}$ ]	$1.23 \times 10^{-5}$
Pad thermal expansion coefficient [ $1/^{\circ}\text{C}$ ]	$1.30 \times 10^{-5}$

\*Assumed based on the available data in Ref. [4].

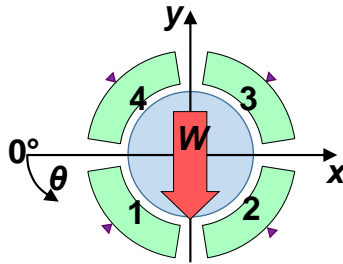


**Figure 28: Schematic view of a four-pad TPJB in Ref. [4]**

Figure 29 shows the pad surface temperature for an operation at 7,000 RPM shaft speed and under three specific loads (along  $y$  direction). Following the bearing provider recommendation, the flow rate is fixed at 42 L/min suitable for the highest shaft speed (16,000 RPM) during all the test operating conditions. Hence, the bearing is likely over-flooded at 7,000 RPM causing substantial amounts of fresh lubricant to axially discharge from the groove. A groove efficiency  $C_{gr} = 0.6$  delivers pad surface temperature predictions conforming with the test data for the TPJB equipped with spray bars. Since the known supply flow rate is utilized to obtain the predictions using novel mixing model, a constant  $C_{gr}$  provides accurate pad surface temperatures.

The agreement between the predictions (TEHD) and the measurements is remarkable and the largest temperature difference is not greater than 3 °C for all three specific loads. As expected, the loaded pads are hotter for operation with a large specific load (2.9 MPa). Conversely, the unloaded pads (③, ④) are hotter when operating with a *small* specific load (0.7 MPa). This phenomenon appears both in measurements and predictions. For (loaded) pads ① and ②, the predicted temperatures are generally close to the measurements; conversely, the measured temperatures on (unloaded) pads ③ and ④ are higher than the predictions.

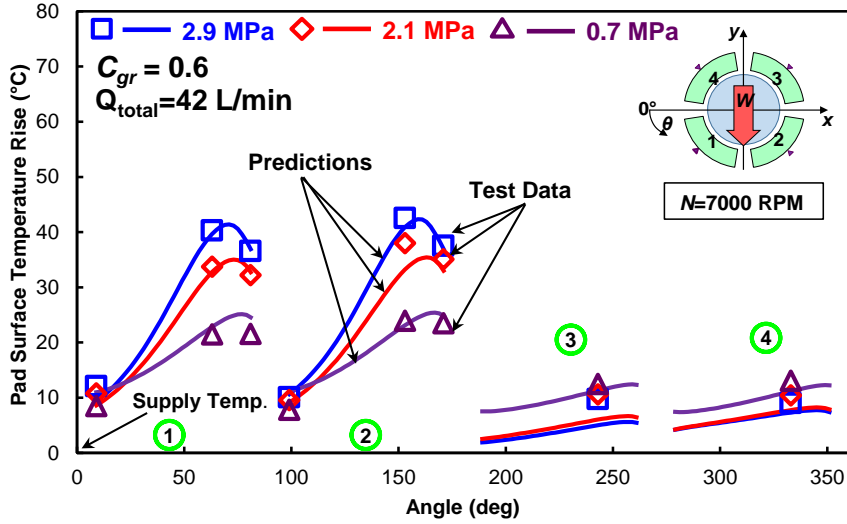


Figure 29: Pads' surface temperature rise versus circumferential location. Predictions compared against test data in Ref. [3]. (Spray Bar, Evacuated,  $T_{sup}= 49^{\circ}\text{C}$ ,  $N=7,000$  RPM,  $W/(LD)=2.9, 2.1, 0.7$  MPa, and  $C_{gr}=0.6$ )

Table 5 shows the predicted flows in the groove region (Eq. (49)) from the current and simple (conventional) thermal mixing models for an operation at a low speed ( $N = 7,000$  RPM) and a low specific load ( $W/(LD) = 0.7$  MPa). Note the large amounts of side leakage flow ( $Q_{SL}$ ) and absence of groove flow ( $Q_{gr}$ ) predicted by the current model. The conventional thermal mixing model predicts  $Q_{sup}^{total} = 19$  L/min since it does not account for the excessive supplied oil (42 L/min). The current model sets  $Q_{sup}^{total} = 42$  L/min, and calculates the amount of extra supplied oil that leaves the groove as a side leakage ( $Q_{SL}$ ).

Nicholas et al. [57] suggest that in an evacuated bearing, depending on the efficiency<sup>18</sup> of the lubricant supply mechanism, some oil escapes the bearing directly without ever lubricating the pads. The temperature of the side leakage flow ( $T_{SL}$ ) is therefore predicted from a weighted average between hot upstream flow and supply flow temperatures adjusted by the groove efficiency parameter ( $C_{gr}$ ).

<sup>18</sup>This is the word used in Ref. [57], and it is not related to the groove efficiency parameter ( $C_{gr}$ ) in this work.

**Table 5: Flow rates [L/min] in the feeding grooves of the bearing in Ref. [3]. Predictions from current model and simple (early) model. (Spray Bar, Evacuated,  $W/(LD)=0.7$  MPa,  $N=7000$  RPM,  $C_{gr}=0.6$ ,  $\lambda=0.8$ )**

Pad	$Q_{TE}^{i-1}$ $Q_{LE}^i$ (L/min)		$\alpha_i$	Current Model $Q_{sup}^i$ $Q_{SL}^i$ $Q_{gr}^i$ (L/min)			Simple Model $Q_{sup}^i$ (L/min)
	1	7.0		6.2	0.14	5.8	6.7
2	3.5	6.2	0.23	9.7	7.0	0	3.4
3	3.5	10.6	0.41	17.2	10.1	0	8.7
4	7.1	10.6	0.22	9.4	5.8	0	5.3
Total:			1.0	42 (L/min)=Test			19 (L/min)

Figure 30 shows the pad surface temperature predictions and measurements at a high speed (16,000 RPM) and three specific loads. Here the difference between predictions and test data for the loaded pads (1,2) does not exceed 4 °C. The predicted temperatures for the unloaded pads have a slightly larger discrepancy with the test data, up to 10 °C. Since the bearing operates in an evacuated condition, it is likely that the unloaded pads are not fully wetted. Yet the predictions are based on the assumption that each pad has a continuous fluid film.

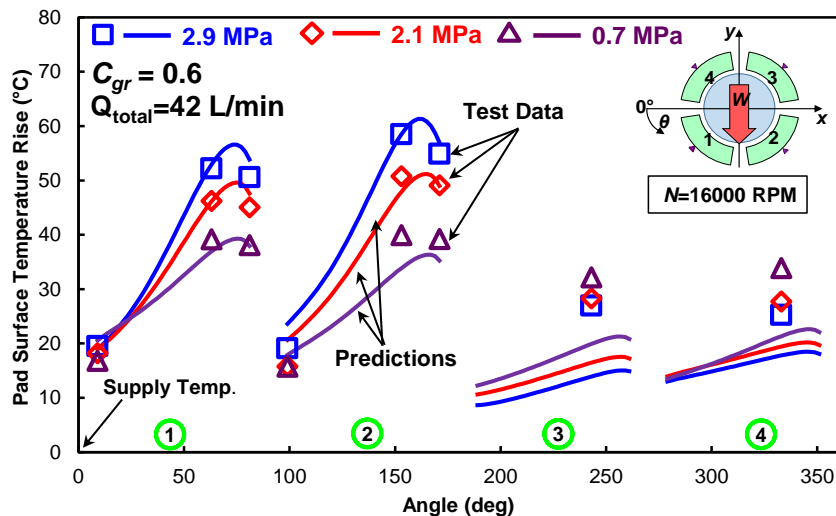
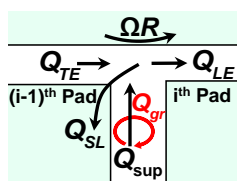


**Figure 30: Pads' surface temperature rise versus circumferential location. Predictions compared against test data in Ref. [3]. (Spray Bar, Evacuated,  $T_{sup}= 49$  °C,  $N=16,000$  RPM,  $W/(LD)=2.9, 2.1, 0.7$  MPa, and  $C_{gr}=0.6$ )**

Table 6 shows the predicted flows in the groove region (Eq. (49)) from the current and simple (old) thermal mixing models for an operation at a high speed ( $N = 16,000$  RPM) and high specific load ( $W/(LD) = 2.9$  MPa). The simple model predicts a total supply flow  $Q_{sup}^{total} = 48$  L/min slightly larger than the actual test condition (42 L/min). For the first pad,  $Q_{TE}^{i-1} > Q_{LE}^i$ , thus the simple model predicts a nil supply flow rate.

Conceivably a portion of the extra lubricant coming from the upstream unloaded pad ④ axially discharges as a side leakage and does not enter pad ①. The novel thermal mixing model predicts the large side leakage flow ( $Q_{SL}^1 = 14.6$  L/min). On the other hand, a large magnitude of groove flow ( $Q_{gr}^4 = 4.3$  L/min) for an evacuated bearing is not physically achievable and suggests occurrence of oil starvation. In this situation the available supply flow (5.7 L/min) is not enough to create a full film at the pad ④ leading edge; thus a full film develops further along the pad arc length. See Ref. [59] for details on a flow starvation model that uses an effective pad arc (wetted) length.

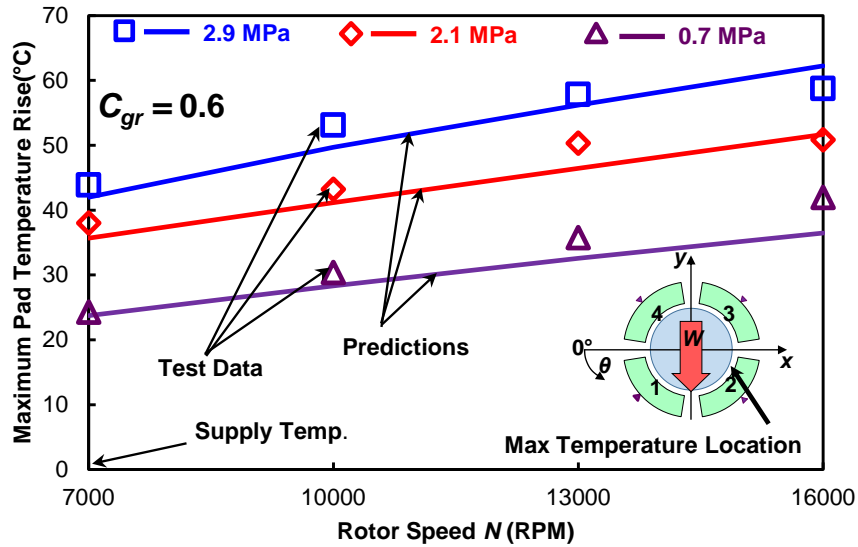
**Table 6: Flow rates [L/min] in the feeding grooves of the bearing in Ref. [3]. Predictions from current model and simple (early) model. (Spray Bar, Evacuated,  $W/(LD)=2.9$  MPa,  $N=16000$  RPM,  $C_{gr}=0.6$ ,  $\lambda=0.8$ )**



Pad	$Q_{TE}^{i-1}$ $Q_{LE}^i$ (L/min)		$\alpha_i$	Current Model (L/min)			Simple Model (L/min)
	$Q_{sup}^i$	$Q_{SL}^i$		$Q_{gr}^i$	$Q_{sup}^i$		
1	22.6	10.3	0.06	2.4	14.6	0	0
2	3.9	9.7	0.14	6.0	0.3	0	7.1
3	3.4	31.2	0.66	28.0	0.1	0	27.8
4	22.8	32.7	0.14	5.7	0	4.3	13.3
Total:			1.0	42 (L/min)=Test			48 (L/min)

Figure 31 compares the maximum predicted pad ② surface temperature to the measured one for various test operating conditions. A fixed groove efficiency parameter ( $C_{gr} = 0.6$ ) delivers predicted temperatures that best fit the test data for all operating conditions with a maximum discrepancy up to 4 °C. The ability to accurately predict the

temperatures with a single  $C_{gr}$  is a notable improvement over the simple thermal mixing model in which the hot oil carry over factor ( $\lambda$ ) needs to be tailored for each operation (in particular shaft speed). Note that during the tests reported in Ref. [4], the total supply flow rate is kept constant for all operating conditions.



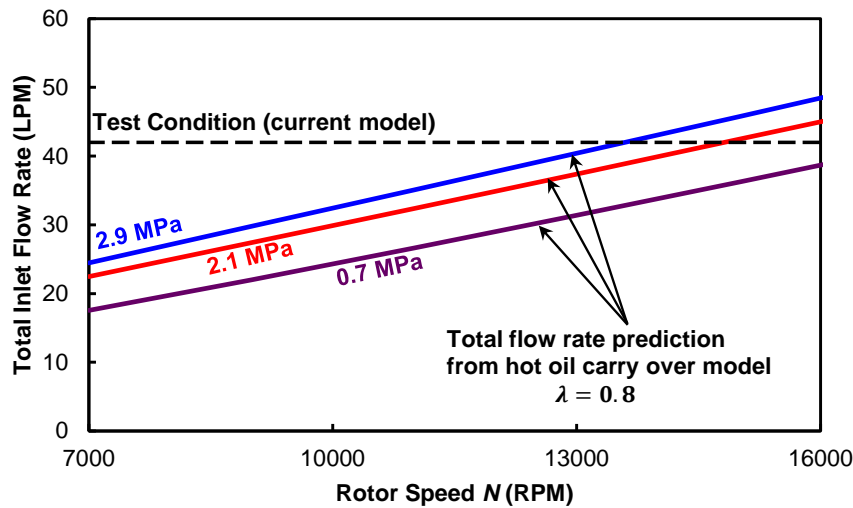
**Figure 31: Maximum inner surface temperature on pad 2 versus shaft speed at operation with three specific loads. Current predictions and test data in Ref. [4]. ( $W/(LD)=2.9, 2.1, 0.7$  MPa,  $C_{gr}=0.6$ )**

Figure 32 shows the predicted total supply flow rate from the simple (early) model with a fixed hot oil carry over factor ( $\lambda = 0.8$ ) versus shaft speed for three specific loads. For most operating conditions, the predicted total supply flow rate is less than the actual one. During the tests, the excess supply flow likely discharges axially outside from the bearing grooves and does not lubricate the pads. However, it contributes to reducing the temperature of the hot oil that travels across each groove. Since the simple (early) model does not account for side leakage flow, a smaller<sup>19</sup>  $\lambda$  must be selected for low shaft speeds to fit the predicted temperatures to the test data. The present thermal mixing model, as shown in Figure 31, delivers accurate film temperatures for a range of operating conditions

<sup>19</sup>From Eq. (1a)  $Q_{sup} = Q_{LE} - \lambda Q_{TE}$ : a decrease in  $\lambda$  increases the predicted supply flow rate.



with a fixed total supply flow rate using a constant  $C_{gr}$ .



**Figure 32: Predicted flow rate versus shaft speed at operation with three specific loads. Constant flow rate in tests [4] for spray-bar with evacuated housing. ( $W/(LD)=2.9, 2.1, 0.7$  MPa)**

Figure 33 compares the predicted pad surface temperature and test data for the other three lubricant delivery methods, namely leading edge groove (LEG), spray bar blocker (SBB), single orifice (SO). The influence of a feeding arrangement on the overall temperature of the film and bounding solids is not limited to the leading edge temperature of the pads. A feeding arrangement alters the temperature generation in the film, the convection coefficients on the pad surfaces, the pressure boundary condition at a pad's leading edge, the turbulence intensity of the supply flow, etc. [48]. However, by selecting an efficiency parameter ( $C_{gr}$ ) appropriate for the feeding arrangement one can fairly predict the overall film temperature for various delivery methods<sup>20</sup>.

Predicted temperatures with  $C_{gr} = 0.9$  and  $0.5$  correlate best with the test data for LEG and SBB lubricant delivery methods, respectively. A spray bar blocker design includes an scraper to remove a layer of the upstream hot oil and displace it out of bearing more

<sup>20</sup>Refer to Table 7 (page 87) for a recommended range of groove efficiency parameter ( $C_{gr}$ ) applicable to various lubricant feeding arrangements.

effectively compared to a conventional spray bar. However, in Ref. [3] the measured peak temperature of each pad with a SBB feeding configuration is higher than that with a SB configuration. Coghlan [3] explains “the SBB attempts to scrape away the hot oil and in doing so seems to back-up the hot oil onto the upstream pad increasing trailing edge temperatures [sic].”

The bearing with a single orifice feeding arrangement is flooded (with end-seals) and receives a  $Q_{sup}^{total} = 38$  L/min during the tests. Predicted temperatures with a  $C_{gr} = 0.2$  match the maximum pad temperature, but show about a 10 °C discrepancy with the test data for the leading edge temperature of pad ②. In fact, the measurements in Ref. [3] consistently suggest that the pad leading edge temperature in a SO configuration is lower than that of SB and SBB (not LEG), alas the maximum measured temperature in SO configuration is always the largest.

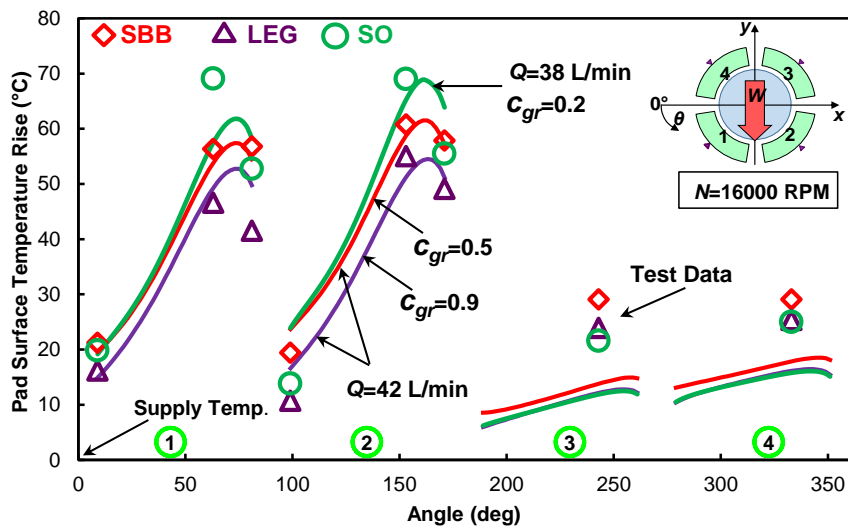


**Figure 33: Pads’ surface temperature rise versus circumferential location for three lubricant delivery methods. Predictions compared against test data in Ref. [3]. (SBB=Spray Bar Blocker, LEG=Leading Edge Groove, SO=Single Orifice,  $T_{sup}= 49^{\circ}\text{C}$ ,  $N=16,000$  RPM,  $W/(LD)=2.9$  MPa)**

Figure 34 shows the predicted journal eccentricity in the load ( $-y$ ) and orthogonal ( $x$ ) directions compared to the measurements in Ref. [4]. Coghlan and Childs [4] introduce a

novel method to measure the journal eccentricity by defining a *hot* bearing center. The new hot bearing center is the origin of a circle that best fits the measured bearing clearances for each pad immediately after an operational shut down. The conventional definition of the hot bearing center is the position of the journal with a zero applied static load, and which is also used in the current predictive model.

The TEHD predictions follow the trend of the test data but with a more or less constant difference which is likely due to the unconventional definition of the bearing center (origin) for the test data. In the load direction ( $-e_y$ ), the agreement between prediction and test data worsens by increasing the specific load. Predicted journal eccentricities from the TEHD analysis (solid lines) are about 25% smaller than the predictions from the THD analysis (dashed lines), and correlate better with the test data. The maximum difference between TEHD predictions and test data is 12, 29, and 37  $\mu\text{m}$  for specific loads of  $W/(LD) = 0.7$ , 2.1, and 2.9 MPa, respectively.

The predicted journal eccentricity in the orthogonal direction ( $e_x$ ) does not exceed 3  $\mu\text{m}$  while the measured ones range between 3  $\mu\text{m}$  and 20  $\mu\text{m}$ . Coghlan [3] states the significant measured orthogonal eccentricity indicates that the tilt motion of the pads is impeded by (an unknown) friction between a pad and its spherical seat pivot.

Ref. [3] reports an uncertainty of 0.1  $\mu\text{m}$  or less for the measured journal eccentricities, which is likely the accuracy of the sensors. However, the actual uncertainty should be larger as the measured eccentricity magnitudes are very small. In addition, uncertainty may also arise from other sources such as proximator accuracy, measurement accuracy, and the accuracy the hot bearing center measurement [60].

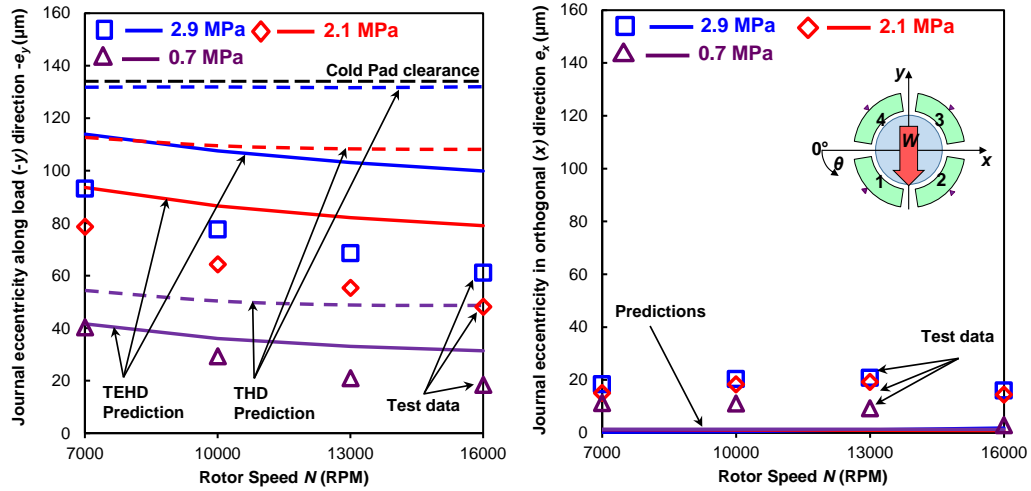


**Figure 34: Journal eccentricities ( $-e_y, e_x$ ) versus rotor speed and operation with three specific loads. Predictions and test data in Ref. [4].**

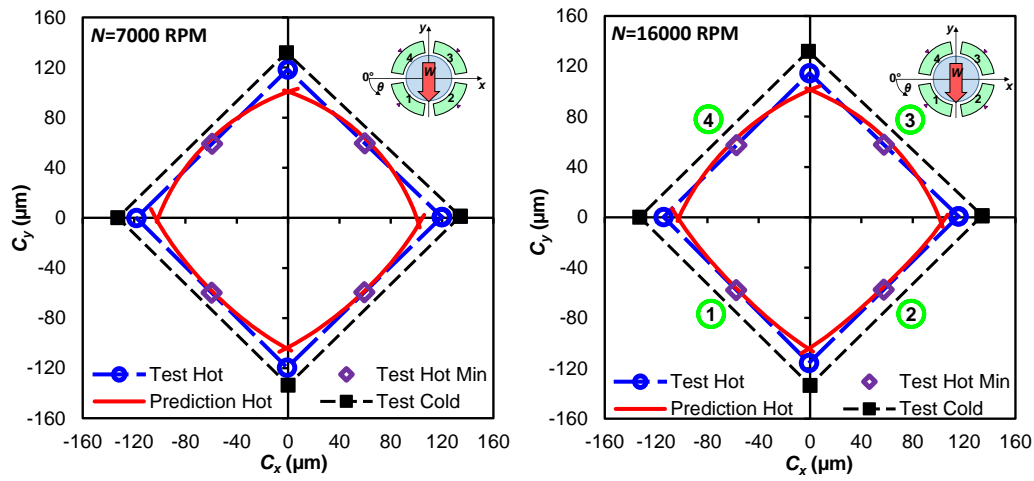
Coghlan and Childs [4] measure the hot bearing clearance by rolling the shaft on the pads immediately after the rotor stops spinning from a rapid deceleration at a constant or steady speed. The predicted hot clearances in the  $x, y$  directions ( $C_x, C_y$ ) corresponding to zero load pad origins ( $O_{p,x}, O_{p,y}$ ) are defined as,

$$C_x = O_{p,x} + \left( R_p + u_{(R_p, \theta)} - R_s - \Delta R_s + \Delta R_h \right) \cos \theta \quad (50a)$$

$$C_y = O_{p,y} + \left( R_p + u_{(R_p, \theta)} - R_s - \Delta R_s + \Delta R_h \right) \sin \theta \quad (50b)$$

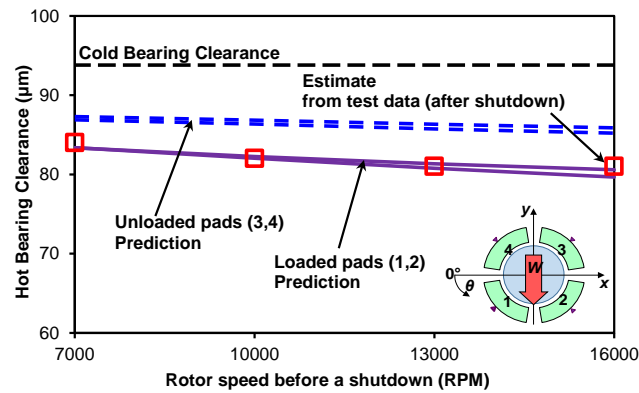
Figure 35 shows the predicted hot clearance on each pad surface (only accounting for thermal deformation) and measured points from Ref. [4]. The agreement between prediction and test data is satisfactory. The clearance of the test bearing has a square shape, the midpoint of each side shows the minimum clearance (bearing clearance). Observe that the predicted minimum clearance is slightly smaller than the measurement for the loaded pads. Since the loaded pads get hotter than unloaded pads during operation (and likely remain hotter immediately after shutdown) they have a more pronounced expansion compared to the unloaded pads. The expansion of the pads towards the center of the

bearing along with expansion of the journal reduce the bearing clearance.



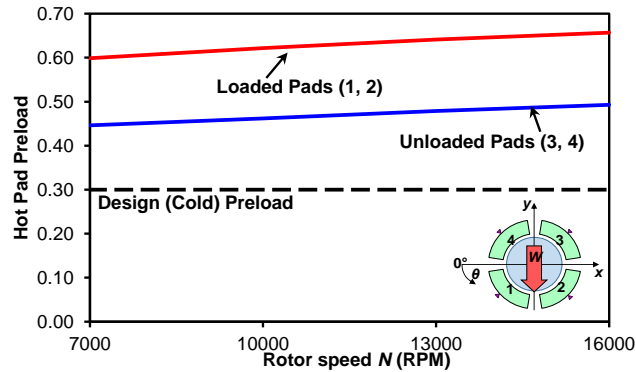
**Figure 35: Predicted hot clearance in x, y coordinate system compared to test data in Ref. [4]. ( $W/(LD)=2.9$  MPa; Left:  $N=7000$ , Right:  $N=16000$ )**

Figure 36 shows the predicted hot bearing clearance for each pad versus shaft speed compared to measured estimates from Ref. [3]. The hydrodynamic pressure induces pad deformation only when the bearing is carrying a load applied via a spinning shaft. The hot bearing clearance is measured at a zero load and estimated from a circle that best fits the minimum clearance of each pad. Hence, predictions include only thermally induced pad deformations. The predictions show a good agreement with test data, with a maximum difference of 5%.



**Figure 36: Estimated hot bearing clearance versus rotor speed before a shutdown for the bearing in Ref. [4]. Predictions only include thermal deformations. ( $W/(LD)=2.9$  MPa)**

Figure 37 shows the predicted increase in preload ( $m = (C_p - C_b)/C_p$ ) of the pads during an operation. Predictions account for both thermally and pressure induced deformations of the pads, thermal expansion of the shaft and the bearing housing (in the outward direction). The bearing clearance ( $C_b$ ) of each pad decreases due to the thermal expansion of both the pad and the shaft. A high hydrodynamic pressure and temperature acting on the loaded pads (3,4) induce a warping effect that increases their curvature and pad clearance ( $C_p$ ). The pad clearance of the unloaded pads does not increase as much. Hence, the preload for loaded pads (1, 2) increases by about 100%, and about 50% for the unloaded pads (3, 4).



**Figure 37: Predicted hot pad preload versus shaft speed for an operation under a specific load of 2.9 MPa**

Coghlan and Childs [5] use a frequency independent ( $[K, C, M]$ ) model to extract the bearing static stiffness  $[K]$ , damping  $[C]$ , and virtual mass  $[M]$  coefficients from curve fits to the experimentally derived complex stiffnesses  $[Z]$ . The imaginary part of the complex stiffness is approximately linear and the slope defines the bearing damping, i.e.  $\Im(Z) \Rightarrow \omega C$ . Whereas the magnitude of complex stiffness real part at zero excitation frequency is the bearing stiffness and a quadratic curvature represents the bearing virtual mass, i.e.  $\Re(Z) \Rightarrow K - \omega^2 M$ . The bearing complex stiffness (impedance) is identified over an excitation frequency range between 10 to 250 Hz. See Ref. [5] for details on the test and

parameter identification procedure.

$$\Re(Z) \Rightarrow K - \omega^2 M, \text{ and } \Im(Z) \Rightarrow \omega C \quad (51)$$

Figures 38 and 39 compare the real and imaginary parts of the measured complex stiffness against the THD and TEHD predictions for operations at two shaft speed (7000 RPM and 16000 RPM) and under three specific loads,  $W/(LD)=0.7, 2.1, 2.9$  MPa. The right side of the Figures show the real part of the bearing direct complex stiffnesses ( $\Re(Z)$ ), and the left part shows the imaginary part of the bearing direct complex stiffness ( $\Im(Z)$ ) versus excitation frequency.

The predicted  $\Re(Z)$ , shows a good agreement with test data for the shown operating conditions. The predicted  $\Im(Z)$  follows the test data closely at  $N = 7000$  RPM, but the agreement reduces as either the shaft speed or the static load increase. The predictions are identical in the load ( $y$ ) or orthogonal ( $x$ ) directions. However, both the imaginary and real parts of the test data are larger along the load direction, and the difference increases as the specific load increase. Since the predictions are the same along the  $x$  and  $y$  directions, and under-predict the test data, they correlate best with the real and imaginary parts of  $Z_{xx}$ .

The TEHD model improves the correlation between the predicted  $\Re(Z)$  and test data, in particular at the high speed ( $N = 16000$  RPM). The imaginary part of the complex stiffness, however, has a slightly lower slope in the TEHD predictions compared to the THD ones. Both models predict accurately the curvature of the  $\Re(Z)$ .

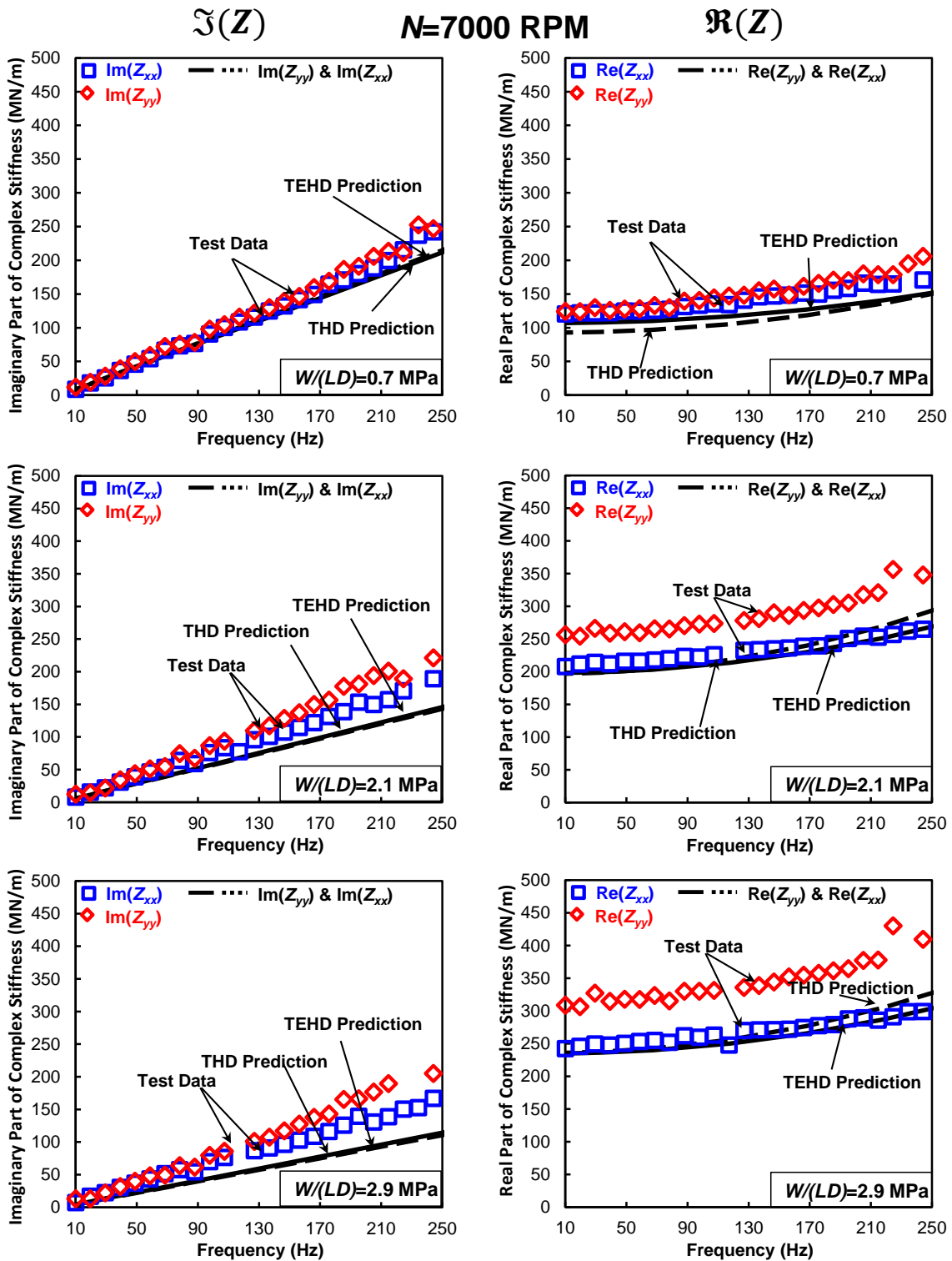


Figure 38: Imaginary (left) and Real (right) parts of bearing complex dynamic stiffness versus excitation frequency for operation at three specific loads. TEHD and THD predictions compared to measurements in Ref. [5] for operation of  $N=7000$ , and  $W/(LD)=0.7, 2.1$ , and  $2.9$  MPa



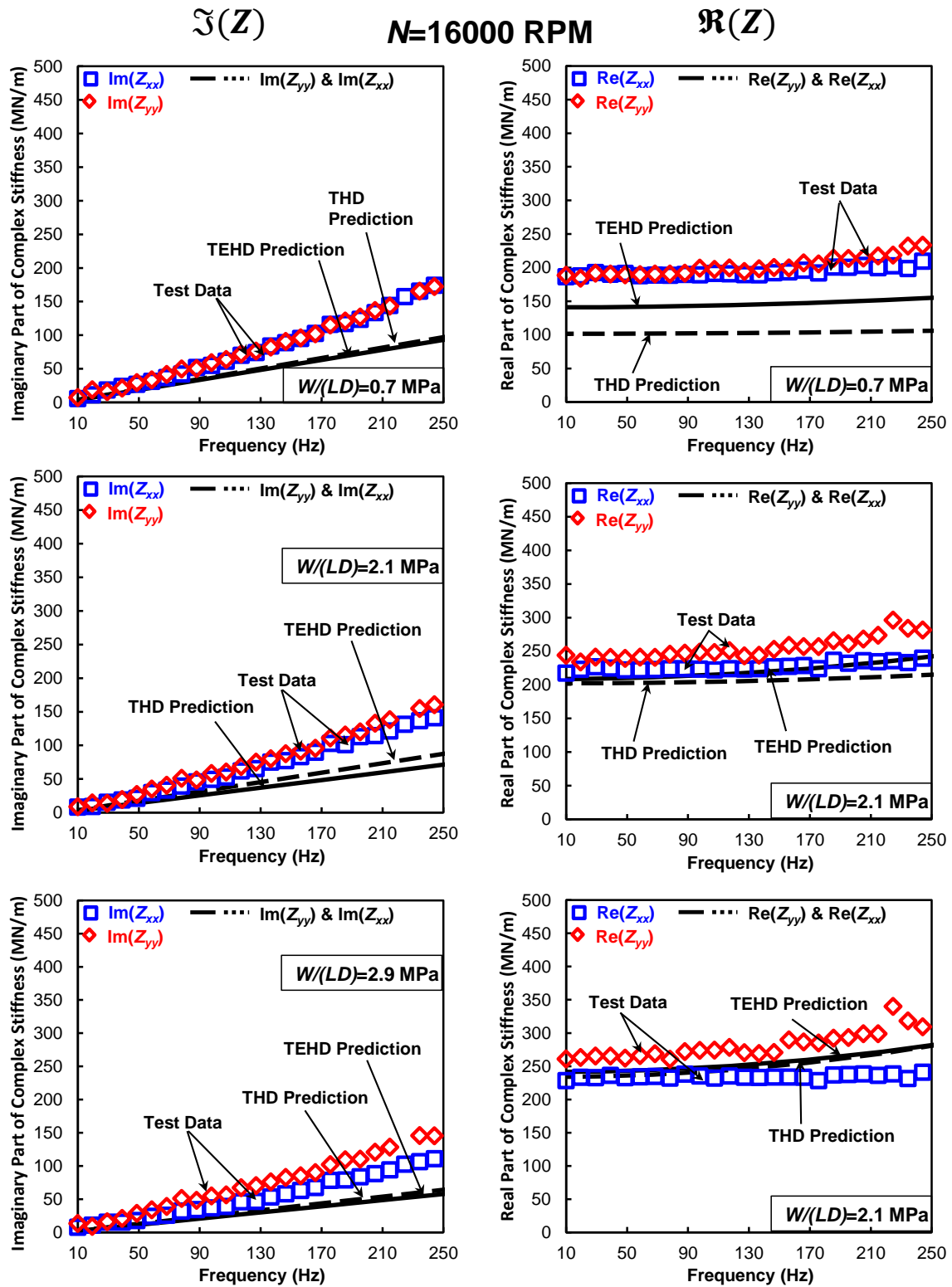


Figure 39: Imaginary (left) and Real (right) parts of bearing complex dynamic stiffness versus excitation frequency for operation at various specific loads. TEHD and THD predictions compared to measurements in Ref. [5] for operation of  $N=16000$ , and  $W/(LD)=0.7, 2.1$ , and  $2.9$  MPa

Figures 40 to 42 show the measured and predicted bearing direct force coefficients (stiffness, damping, and virtual mass) with a  $[K, C, M]$  model (Eq. (51)) that best fits the real and imaginary parts of the complex stiffness. The rotordynamic coefficients are presented for an operation at a shaft speed ranging between 7000 RPM and 10000 RPM and under a specific load ranging from 0.7 MPa to 2.9 MPa. The uncertainty associated with the measured direct stiffness and damping are 2% and 5% of the coefficient magnitude, respectively. The predicted cross-coupled force coefficients are very small and not shown. The predictions include a linear pivot stiffness of 412 MN/m, as reported in Ref. [3], and which is in the same order of magnitude as the predicted film stiffness with a rigid pivot assumption (150 MN/m to 700 MN/m).

Figure 40 shows that the bearing stiffnesses ( $K_{xx}, K_{yy}$ ) increase with an increase in the static load at a given shaft speed. On the other hand, an increase in shaft speed reduces the bearing direct stiffnesses at a constant specific load. The current models (THD and TEHD) predict isotropic direct stiffnesses ( $K_{xx} = K_{yy}$ ) for the bearing, but the test data show stiffness orthotropy ( $K_{yy} > K_{xx}$ ) which is not expected for a LBP configuration with identical pads. Also the stiffness orthotropy in the test data increases with an increase in specific load.

Figure 40 illustrates an aspect of importance for rotordynamic analysis; accounting for thermoelastic deformation of the TPJB elements. Observe that at the (low) shaft speed of 7000 RPM, the TEHD predictions are similar to the THD predictions, but the difference enlarges as the shaft speed increases and the bearing operates at higher temperatures. The difference between TEHD and THD models is most pronounced at a low specific load (0.7 MPa) where the thermally induced deformation is dominant and the thermal expansion of the bearing components reduces the film thickness to make the bearing stiffer. On the other hand, at a high specific load (2.9 MPa), the pressure induced pad deformation is dominant, and the elastic increase in pad curvature slightly increases the film thickness, to offset the

stiffness increase from the thermal effects.

TEHD predictions for  $K_{yy}$ ,  $K_{xx}$  are in a good agreement with the measurements with a maximum difference not exceeding 25%, with an average difference of 17% along the load direction ( $y$ ) and 8% in the orthogonal direction ( $x$ ). Including thermally and pressure induced deformations increase the predictions up to 28%, and thus improve the agreement with the test data.

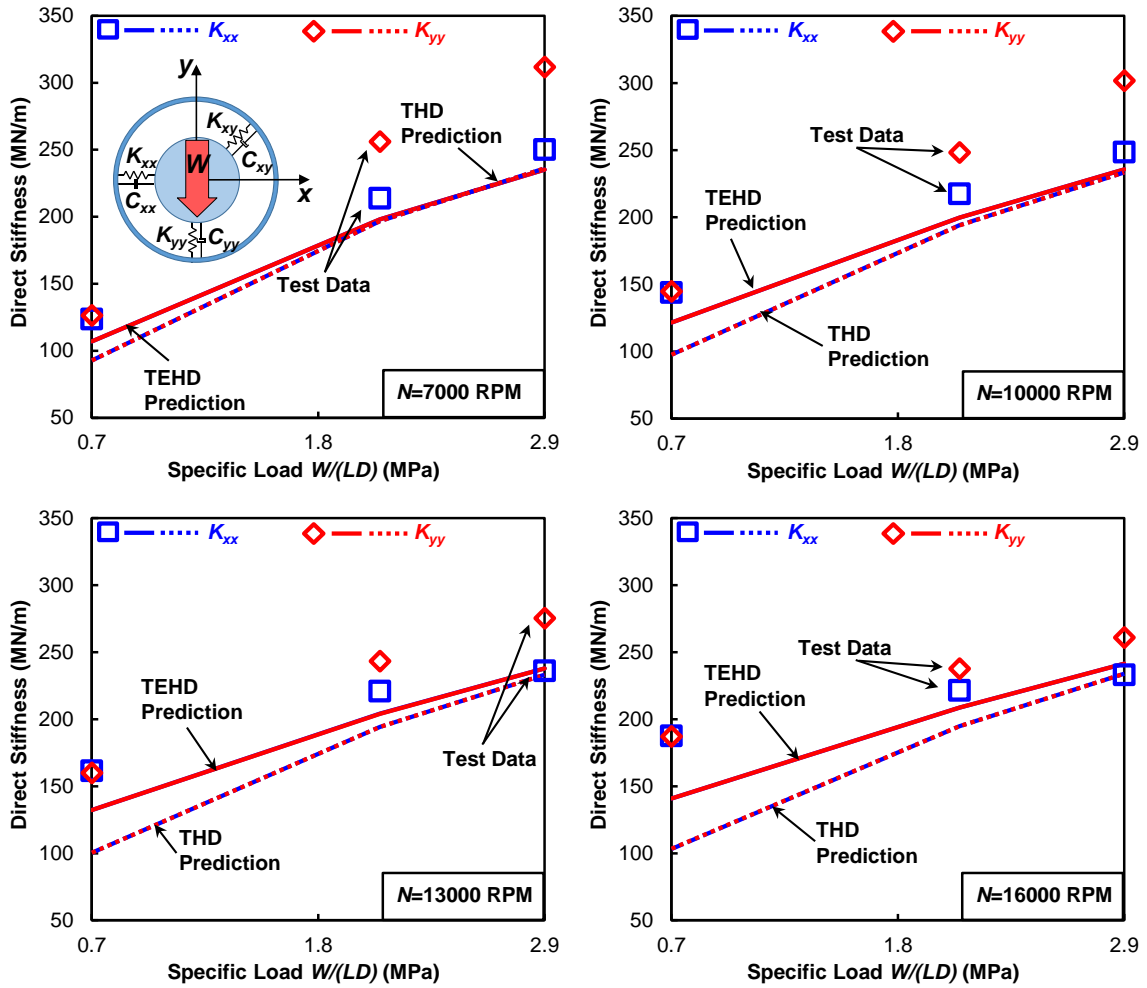


Figure 40: Direct stiffness coefficients ( $K_{yy}$ ,  $K_{xx}$ ) versus specific load for operation at four shaft speeds. TEHD and THD prediction and test data in Ref. [5]

Figure 41 shows predicted damping coefficients ( $C_{xx}$ ,  $C_{yy}$ ) in comparison with the estimations from the test data. The bearing damping decreases with an increase either

in the static load or the shaft speed. As the shaft speed or specific load increase, the predicted damping coefficients decline more rapidly compared to test data. Compared to the stiffnesses, the predicted  $(C_{xx}, C_{yy})$  show a consistent large discrepancy with the measurements. Also, the predicted damping from the TEHD model is slightly (up to 2%) smaller than the THD predictions. The maximum difference between TEHD predictions and test data is 59% and 45% for  $C_{yy}$  and  $C_{xx}$ , respectively. The average difference is 25% in the load direction and 41% in the orthogonal direction with respect to the test data.

Judging from the similar trends in the TEHD predictions and the test data for stiffness and damping coefficients and observing a consistent difference, it is surmised that the pivot stiffness (412 MN/m) used in the predictions is not sufficiently large. The discrepancy between the predicted damping coefficients and the test data is more pronounced than that for the stiffnesses since “Pivot flexibility has a more pronounced effect on reducing the bearing damping coefficients than the stiffness coefficients” [22].

According to Coghlan [3], the pivot stiffness is approximated by fitting a linear curve to force versus displacement data for a single pad in LOP orientation. The range of the applied force to measure pivot stiffness is up to 4750 N. During the tests, however, the applied load on the bearing ranges up to 18000 N. It is not clear if the pivot stiffness remains the same in an operation under a heavy load and high oil temperature. Furthermore, Harris [61] details the complexities associated with measuring the stiffness of a similar spherical seat pivot, such as machining tolerance that makes the pivots non-identical, and the differential thermal growth of a steel ball and its bronze socket.

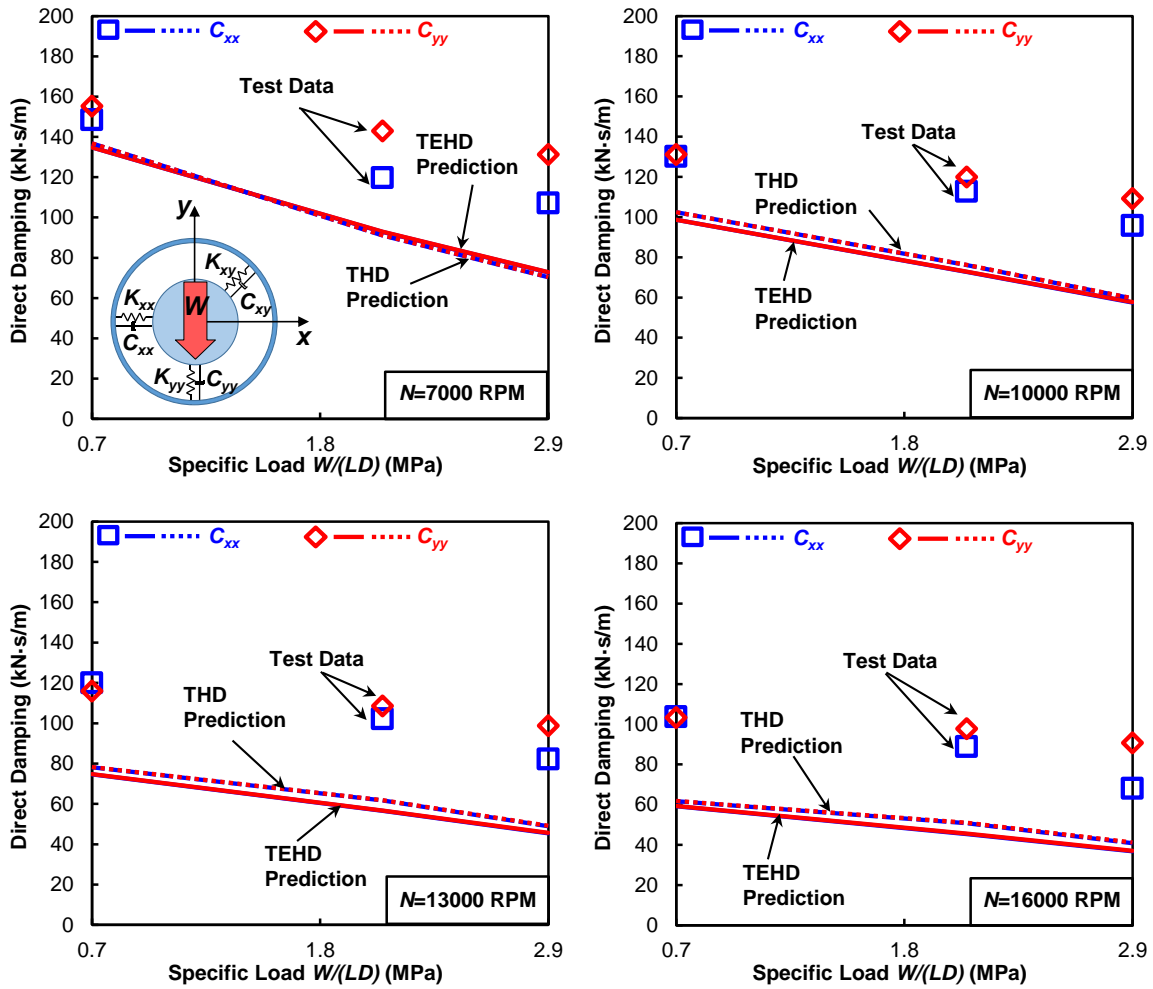


Figure 41: Direct damping coefficients ( $C_{yy}$ ,  $C_{xx}$ ) versus specific load for operation at four shaft speeds. TEHD and THD prediction and test data in Ref. [5]

Figure 42 shows predicted virtual mass coefficients ( $M_{xx}$ ,  $M_{yy}$ ) in comparison with the test force coefficients. A negative virtual mass indicates that the real part of the complex stiffness ( $\Re(Z)$ ) increases with excitation frequency. This ‘stiffening effect’ is common in TPJBs [3]. Unlike the bearing stiffness and damping from the test data, the test identified virtual mass magnitudes carry a significant uncertainty (sometimes up to 50%) associated with them. Hence, one cannot rely on the exact magnitudes of the experimental virtual mass.

The test direct virtual mass term is more negative in the load direction compared to

that in the orthogonal direction ( $M_{yy} < M_{xx}$ ). The predictions show an equal virtual mass in both directions. The TEHD predictions are less negative than the THD ones, and both analyses deliver  $M_{xx}$  and  $M_{yy}$  in fair agreement with the test data.

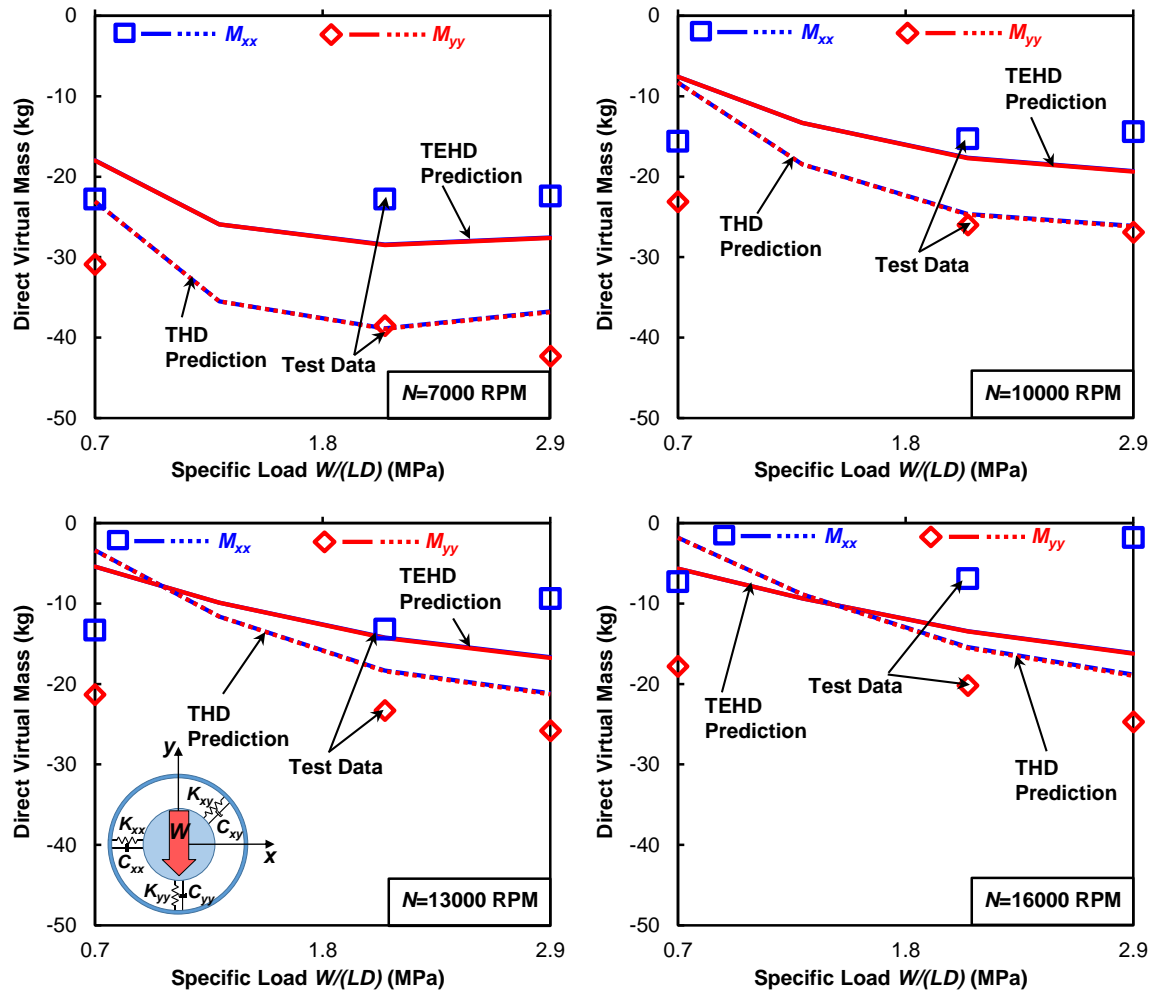


Figure 42: Direct virtual mass coefficients ( $M_{yy}$ ,  $M_{xx}$ ) versus specific load for operation at four shaft speeds. TEHD and THD prediction and test data in Ref. [5]

## 6 CONCLUSION

An accurate characterization of the static load performance in a bearing is paramount to also predict accurate rotordynamic force coefficients. An analysis that couples pressure generation to thermal effects in a bearing requires an accurate prediction of film and pad temperatures. Thus, this work introduces a simple yet effective thermal flow mixing model for the lubricant in a supply groove region that rectifies some limitations associated with a conventional hot oil carry over model (see Ref. [16]).

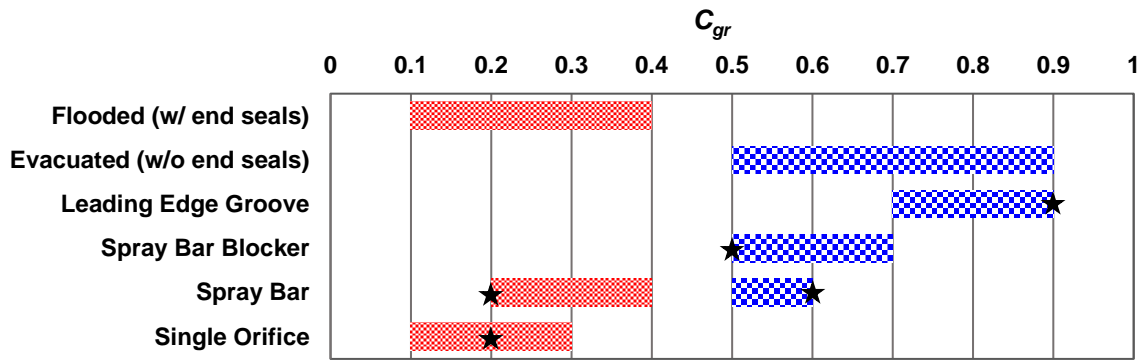
The the hot oil carry over model predicts total flow rate of fresh (cold) lubricant that is supplied to a tilting pad journal bearing (TPJB) during operation, but it may differ with the actual flow. The novel mixing model utilizes a known total flow supply rate and allocates a portion of it to each feeding groove. For instance, Hagemann et al. [1] reduce the total flow rate supplied to a test TPJB by using axial end seals. For this case, a conventional hot oil carry over model over estimates the total flow rate by over 70% which causes a 17 °C under prediction of pad surface temperature even with a large hot oil carry over factor ( $\lambda = 0.9$ ). The novel thermal mixing model improves the accuracy of predicted pad surface temperatures by accounting for the recirculating lubricant in the grooves of a (flooded) bearing.

Furthermore, when a bearing housing is evacuated, considerable amounts of hot lubricant as well as freshly supplied oil discharge axially at the grooves between the pads [57]. The novel mixing model takes into account the axially discharged (side leakage) flow, and utilizes an empirical coefficient ( $C_{gr}$ ) to represent the efficiency of the bearing feeding arrangement.  $0 < C_{gr} < 1$  specifies the contributions of *hot* upstream trailing edge flow and *cold* supply flow in a thermal energy exchange with discharge (side leakage) lubricant and the oil that churns in the groove.

Table 7 shows approximate ranges of the groove mixing efficiency parameter ( $C_{gr}$ ) for

various feeding arrangements and end seal configurations that deliver pad surface temperature prediction which best fit the test data in Refs. [1, 3, 33]. As opposed to the hot oil carry over factor ( $\lambda$ ), and since the known total supply flow is utilized,  $C_{gr}$  does not require modification for each operating condition. The predicted pad surface temperatures using the present thermal mixing model for the bearings in Refs. [1, 3] have less than 5 °C discrepancy with the test data for various operating conditions. Note that the total supply flow rate is known at all instances.

**Table 7: Recommended approximate range of groove efficiency parameter ( $C_{gr}$ ) for various lubrication methods. Symbol ★ marks the  $C_{gr}$  magnitudes discussed in this thesis.**



The present work also implements a method to include thermally induced mechanical deformation of the pads in a bearing. An approach using theory of elasticity for a curved beam subject to a radial temperature gradient derives an equation that predicts the pad thermally induced deformation. The deformation is a function of the temperature difference between the inner and back surfaces, both circumferentially averaged. The method provides good accuracy and a straightforward implementation avoiding an iterative procedure.

With respect to static load test data in Refs. [1, 3], including the thermally induced pad surface deformation improves the film thickness prediction. The film thickness then generates a more accurate hydrodynamic pressure on each pad (about 20% improvement for peak film pressures). Accounting for the thermoelastic deformations in a TEHD analysis



also reduces the predicted journal eccentricity in the load direction about 25%, improving the correlation with test data.

For the example TPJBs studied, thermal expansion of the bearing elements reduce the *bearing clearance* about 20% during its operation, while a hydrodynamic pressure along with a thermal gradient warp the pads and thus increase the *pad clearance*. Therefore, the pads' machined (cold) preload increases during operation. The predictions for the bearing in Ref. [3] show the loaded pads undergo a %100 preload increase (0.3 to 0.6) during an operation under a heavy load (2.9 MPa).

As per the dynamic force coefficients, including the pad thermoelastic deformations enhances the predictions, in particular it improves up to 28% the agreement of bearing direct stiffnesses with the test data in Ref. [3]. For a bearing operating at a high speed and under a low specific load, a pad thermally induced deformation is dominant since it reduces the bearing hot clearance and increases the predicted stiffness. As the applied static load increases, the pressure induced deformation becomes dominant and softens the bearing. The (TEHD) predicted bearing stiffnesses correlate well with the test data from Refs. [2, 3] with an average difference about 20%. The (TEHD) predicted damping coefficients and test data in Ref. [3] show a similar trend, but the predictions underestimate the test coefficients by about 40% which may be due to the magnitude of pivot flexibility used in the predictions.

Future work should further validate the novel thermal mixing model against a wide variety of test data for bearings with various other geometries, number of pads, load orientation (LOP, LBP), lubrication delivery methods, and end-seal configurations. In particular, appropriate magnitudes for the groove efficiency parameter ( $C_{gr}$ ) applicable to a lubricant feeding and/or end seal arrangements must be quantified.

## REFERENCES

- [1] Hagemann, T., Kukla, S., and Schwarze, H., 2013, "Measurement and Prediction of the Static Operating Conditions of a Large Turbine Tilting-Pad Bearing Under High Circumferential Speeds and Heavy Loads," ASME Paper No. GT2013-95004, ASME Turbo Expo 2013: Turbine Technical Conference and Exposition, June 3-7, San Antonio, Texas, USA.
- [2] Kukla, S., Hagemann, T., and Schwarze, H., 2013, "Measurement and Prediction of the Dynamic Characteristics of a Large Turbine Tilting-Pad Bearing Under High Circumferential Speeds," ASME Paper No. GT2013-95074, ASME Turbo Expo 2013: Turbine Technical Conference and Exposition, June 3-7, San Antonio, Texas, USA.
- [3] Coghlan, D. M., 2014, "Static, Rotordynamic, and Thermal Characteristics of a Four Pad Spherical-Seat Tilting Pad Journal Bearing with Four Methods of Directed Lubrication," Masters thesis, Texas A&M University, College Station, TX, USA.
- [4] Coghlan, D. M., and Childs, D. W., 2015, "Characteristics of a Spherical Seat T-PJB With Four Methods of Directed Lubrication: Part 1—Thermal and Static Performance," ASME Paper No. GT2015-42331, ASME Turbo Expo 2015: Turbine Technical Conference and Exposition, June 15-19, Montreal, Canada.
- [5] Coghlan, D. M., and Childs, D. W., 2015, "Characteristics of a Spherical Seat TPJB With Four Methods of Directed Lubrication: Part 2—Rotordynamic Performance," ASME Paper No. GT2015-42336, ASME Turbo Expo 2015: Turbine Technical Conference and Exposition, June 15-19, Montreal, Canada.
- [6] He, M., Cloud, C. H., Byrne, J. M., and Vázquez, J. A., 2015, "Fundamentals of Fluid Film Journal Bearing Operation and Modeling," Proceedings of the 44<sup>th</sup> Turbomachinery Symposium, The Turbomachinery Laboratory, Texas A&M University, September 14-17, Houston, Texas, USA.
- [7] Nicholas, J. C., 2003, "Tilting Pad Journal Bearings With Spray-Bar Blockers and By-Pass Cooling for High Speed, High Load Applications," Proceedings of the 32<sup>nd</sup> Turbomachinery Symposium, The Turbomachinery Laboratory, Texas A&M University, September 21-24, Houston, Texas, USA, p. 27.
- [8] Ettles, C. M., 1980, "The Analysis and Performance of Pivoted Pad Journal Bearings Considering Thermal and Elastic Effects," ASME J. Lubr. Technol., **102**(2), pp. 182–191.
- [9] Brugier, D., and Pascal, M. T., 1989, "Influence of Elastic Deformations of Turbo-Generator Tilting Pad Bearings on the Static Behavior and on the Dynamic Coefficients in Different Designs," ASME J. Tribol., **111**(2), pp. 364–371.

- [10] Fillon, M., Souchet, D., and Frêne, J., 1990, “Influence of Bearing Element Displacements on Thermohydrodynamic Characteristics of Tilting-Pad Journal Bearings,” Proc. Japan International Tribology Conference, October, Nagoya, Japan, pp. 635–640.
- [11] Fillon, M., Bligoud, J. C., and Frene, J., 1992, “Experimental Study of Tilting Pad Journal Bearings—Comparison With Theoretical Thermoelastohydrodynamic Results,” ASME J. Tribol., **114**(3), pp. 579–587.
- [12] Brockwell, K., and Dmochowski, W., 1992, “Thermal Effects in the Tilting Pad Journal Bearings,” J. Phys. D: Appl. Phys., **25**(3), p. 384.
- [13] Suh, J., and Palazzolo, A., 2015, “Three-Dimensional Dynamic Model of TEHD Tilting-Pad Journal Bearing—Part II: Parametric Studies,” ASME J. Tribol., **137**(4), p. 041704.
- [14] Suh, J., and Palazzolo, A., 2015, “Three-Dimensional Dynamic Model of TEHD Tilting-Pad Journal Bearing—Part II: Parametric Studies,” ASME J. Tribol., **137**(4), p. 041704.
- [15] Ettles, C., 1967, “Paper 15: Solutions for Flow in a Bearing Groove,” Proc. IMechE: Part 3L, **182**(14), pp. 120–131.
- [16] Mitsui, J., Hori, Y., and Tanaka, M., 1983, “Thermohydrodynamic Analysis of Cooling Effect of Supply Oil in Circular Journal Bearing,” ASME J. Lubr. Technol., **105**(3), pp. 414–420.
- [17] Heshmat, H., and Pinkus, O., 1986, “Mixing Inlet Temperatures in Hydrodynamic Bearings,” ASME J. Tribol., **108**(2), pp. 231–244.
- [18] Brito, F., Miranda, A., Claro, J. C. P., Teixeira, J., Costa, L., and Fillon, M., 2014, “Thermohydrodynamic Modelling of Journal Bearings Under Varying Load Angle and Negative Groove Flow Rate,” Proc. IMechE Part J: Eng. Tribol., **228**(9), pp. 955–973.
- [19] Brito, F., 2009, “Thermohydrodynamic Performance of Twin Groove Journal Bearings Considering Realistic Lubricant Supply Conditions: A Theoretical and Experimental Study,” PhD thesis, University of Minho, Braga, Portugal.
- [20] Rindi, A., Rossin, S., Conti, R., Frilli, A., Galardi, E., Meli, E., Nocciolini, D., and Pugi, L., 2016, “Efficient Models of Three-Dimensional Tilting Pad Journal Bearings for the Study of the Interactions Between Rotor and Lubricant Supply Plant,” ASME J. Comput. Nonlinear. Dyn., **11**(1), p. 011011.

- [21] He, M., Cloud, C. H., Byrne, J. M., and Vázquez, J. A., 2012, “Steady State Performance Prediction of Directly Lubricated Fluid Film Journal Bearings,” Proceedings of the 41<sup>st</sup> Turbomachinery Symposium, The Turbomachinery Laboratory, Texas A&M University, September 24-27, Houston, Texas, USA.
- [22] San Andrés, L., and Tao, Y., 2013, “The Role of Pivot Stiffness on the Dynamic Force Coefficients of Tilting Pad Journal Bearings,” *ASME J. Eng. Gas Turb. Pow.*, **135**(11), p. 112505.
- [23] San Andrés, L., and Li, Y., 2015, “Effect of Pad Flexibility on the Performance of Tilting Pad Journal Bearings—Benchmarking a Predictive Model,” *ASME J. Eng. Gas Turb. Pow.*, **137**(12), p. 122503.
- [24] San Andrés, L., Tao, Y., and Li, Y., 2015, “Tilting Pad Journal Bearings: On Bridging the Hot Gap Between Experimental Results and Model Predictions,” *ASME J. Eng. Gas Turb. Pow.*, **137**(2), p. 022505.
- [25] Gaines, J. E., and Childs, D. W., 2016, “The Impact of Pad Flexibility on the Rotor-dynamic Coefficients of Tilting-Pad Journal Bearings,” *ASME J. Eng. Gas Turb. Pow.*, **138**(8), p. 082501.
- [26] Nilsson, L., 1978, “The Influence of Bearing Flexibility on the Dynamic Performance of Radial Oil Film Bearings,” Proceedings 5th Leeds-Lyon Symposium on Tribology, October, Lyon, France, pp. 19–22.
- [27] Lund, J. W., and Pedersen, L. B., 1987, “The Influence of Pad Flexibility on the Dynamic Coefficients of a Tilting Pad Journal Bearing,” *ASME J. Tribol.*, **109**(1), pp. 65–70.
- [28] Wilcock, D. F., and Booser, E. R., 1990, “Thermal Behavior in Tilting Pad Journal Bearings,” *STLE Tribol. Trans.*, **33**(2), pp. 247–253.
- [29] Ferron, J., Frene, J., and Boncompain, R., 1983, “A Study of the Thermohydrodynamic Performance of a Plain Journal Bearing Comparison Between Theory and Experiments,” *ASME J. Lubr. Technol.*, **105**(3), pp. 422–428.
- [30] Boncompain, R., Fillon, M., and Frene, J., 1986, “Analysis of Thermal Effects in Hydrodynamic Bearings,” *ASME J. Tribol.*, **108**(2), pp. 219–224.
- [31] Fillon, M., Desbordes, H., Frene, J., and Wai, C. C. H., 1996, “A Global Approach of Thermal Effects Including Pad Deformations in Tilting-Pad Journal Bearings Submitted to Unbalance Load,” *ASME J. Lubr. Technol.*, **118**(1), pp. 169–174.
- [32] Hopf, G., and Schuler, D., 1989, “Investigations on Large Turbine Bearings Working Under Transitional Conditions Between Laminar and Turbulent Flow,” *ASME J. Tribol.*, **111**(4), pp. 628–634.

- [33] Kulhanek, C. D., and Childs, D. W., 2012, “Measured Static and Rotordynamic Coefficient Results for a Rocker-Pivot, Tilting-Pad Bearing With 50 and 60% Offsets,” *ASME J. Eng. Gas Turb. Pow.*, **134**(5), p. 052505.
- [34] Ettles, C., 1969, “Paper 11: Hot Oil Carry-Over in Thrust Bearings,” *Proc. IMechE: Part 3L*, **184**(12), pp. 75–81.
- [35] Nicholas, J. C., 1994, “Tilting Pad Bearing Design,” Proceedings of the 23<sup>rd</sup> Turbomachinery Symposium, The Turbomachinery Laboratory, Texas A&M University, September 13-16, Houston, Texas, USA.
- [36] Kosasih, P., and Tieu, A., 2004, “An Investigation Into the Thermal Mixing in Journal Bearings,” *Proc. IMechE Part J: J. Eng. Tribol.*, **218**(5), pp. 379–389.
- [37] Uhkoetter, S., aus der Wiesche, S., and Joos, F., 2014, “Detailed CFD Modeling of the Mixing Behavior in Oil Supply Pockets of Heavy Duty Gas and Steam Turbine Journal Bearings,” ASME Paper No. GT2014-25074, ASME Turbo Expo 2014: Turbine Technical Conference and Exposition, June 16-20, Dusseldorf, Germany.
- [38] Uhkoetter, S., aus der Wiesche, S., and Joos, F., 2013, “Investigation of Flow and Mixing Phenomena in an Oil Supply Pocket of a Heavy Duty Gas Turbine Journal Bearing,” ASME Paper No. GT2013-94364, ASME Turbo Expo 2013: Turbine Technical Conference and Exposition, June 3-7, San Antonio, Texas, USA.
- [39] Grzegorz, R., and Michal, W., 2007, “CFD Analysis of the Lubricant Flow in the Supply Groove of a Hydrodynamic Thrust Bearing Pad,” ASME Paper No. IJTC2007-44304, ASME/STLE 2007 International Joint Tribology Conference, October 22-24, San Diego, California, USA, pp. 307–309.
- [40] Keogh, P., Gomiciaga, R., and Khonsari, M., 1997, “CFD Based Design Techniques for Thermal Prediction in a Generic Two-Axial Groove Hydrodynamic Journal Bearing,” *ASME J. Tribol.*, **119**(3), pp. 428–435.
- [41] San Andrés, L., 2012, Modern Lubrication Theory, Notes 10: Thermohydrodynamic Bulk-Flow Model in Thin Film Lubrication, <http://hdl.handle.net/1969.1/93250> [Online; accessed July 2016].
- [42] Varela, A. C., Fillon, M., and Santos, I. F., 2012, “On the Simplifications for the Thermal Modeling of Tilting-Pad Journal Bearings Under Thermoelastohydrodynamic Regime,” ASME Paper No. GT2012-68329, ASME Turbo Expo 2012: Turbine Technical Conference and Exposition, June 11-15, Copenhagen, Denmark, American Society of Mechanical Engineers, pp. 823–835.
- [43] Hausen, H., 1959, “Neue Gleichungen Für Die Wärmeübertragung Bei Freier Und Erzwungener Strömung,” *Allg. Wärmetech*, **9**(4), p. 5.

- [44] Branagan, L., and L, B., 1988, “Thermal Analysis of Fixed and Tilting Pad Journal Bearings Including Crossfilm Viscosity Variations and Deformations,” PhD thesis, University of Virginia, Charlottesville, VA, USA.
- [45] Gnielinski, V., 2009, “Heat Transfer Coefficients for Turbulent Flow in Concentric Annular Ducts,” *Heat Transfer Eng.*, **30**(6), pp. 431–436.
- [46] Wodtke, M., Fillon, M., Schubert, A., and Wasilczuk, M., 2013, “Study of the Influence of Heat Convection Coefficient on Predicted Performance of a Large Tilting-Pad Thrust Bearing,” *ASME J. Tribol.*, **135**(2), p. 021702.
- [47] Knight, J. D., 1990, “Prediction of Temperatures in Tilting Pad Journal Bearings,” *STLE Tribol. Trans.*, **33**(2), pp. 185–192.
- [48] He, M., 2003, “Thermoelastohydrodynamic Analysis of Fluid Film Journal Bearings,” PhD thesis, University of Virginia, Charlottesville, VA, USA.
- [49] Conti, R., Frilli, A., Meli, E., Nocciolini, D., Panconi, S., Pugi, L., Rindi, A., and Rossin, S., 2016, “Development and Validation of an Efficient TEHD Model of Tilting Pad Journal Bearings,” ASME Paper No. GT2016-57401, ASME Turbo Expo 2016: Turbomachinery Technical Conference and Exposition, June 13-17, Seoul, South Korea.
- [50] Pinkus, O., 1990, *Thermal Aspects of Fluid Film Tribology*, ASME Press, pp. 188-197.
- [51] He, M., Allaire, P., Barrett, L., and Nicholas, J., 2005, “Thermohydrodynamic Modeling of Leading-Edge Groove Bearings Under Starvation Condition,” *Trib. Trans.*, **48**(3), pp. 362–369.
- [52] San Andrés, L., 2012, *Modern Lubrication Theory, Notes 2: Derivation of the Classical Reynolds Equation for Thin Film Flows*, <http://hdl.handle.net/1969.1/93242> [Online; accessed July 2016].
- [53] Ha, H. C., Kim, H. J., and Kim, K. W., 1995, “Inlet Pressure Effects on the Thermohydrodynamic Performance of a Large Tilting Pad Journal Bearing,” *ASME J. Tribol.*, **117**(1), pp. 160–165.
- [54] Boley, B. A., and Weiner, J. H., 1960, *Theory of Thermal Stresses*, John Wiley and Sons Inc., pp. 244-249.
- [55] Timoshenko, S. P., and Goodier, J. N., 1970, *Theory of Elasticity*, third ed. McGraw-Hill, pp. 75-80.
- [56] Hetnarski, R. B., Eslami, M. R., and Gladwell, G., 2009, *Thermal Stresses: Advanced Theory and Applications*, Vol. 41 Springer, pp. 227-231.

- [57] Nicholas, J. C., Elliott, G., Shoup, T. P., and Martin, E., 2008, “Tilting Pad Journal Bearing Starvation Effects,” Proceedings of the 37<sup>th</sup> Turbomachinery Symposium, The Turbomachinery Laboratory, Texas A&M University, September 15-18, Houston, Texas, USA, pp. 8–11.
- [58] Kirk, R., and Reedy, S., 1988, “Evaluation of Pivot Stiffness for Typical Tilting-Pad Journal Bearing Designs,” ASME J. Vib., Acoust., Stress, and Reliab, **110**(2), pp. 165–171.
- [59] San Andrés, L., and Koo, B., 2016, “A Flow Starvation Model for Tilting Pad Journal Bearings and Evaluation of Frequency Response Functions—Steps Towards Understanding the Onset of SSV Hash,” Final Project Report to Hitachi Research Laboratory, Hitachi Ltd., TEES # 32525/C6060/ME.
- [60] Wygant, K. D., Flack, R. D., and Barrett, L. E., 1999, “Influence of Pad Pivot Friction on Tilting-Pad Journal Bearing Measurements—Part I: Steady Operating Position,” Trib. Trans., **42**(1), pp. 210–215.
- [61] Harris, J. M., 2008, “Static Characteristics and Rotordynamic Coefficients of a Four-Pad Tilting-Pad Journal Bearing With Ball-in-Socket Pivots in Load-Between-Pad Configuration,” Masters thesis, Texas A&M University, College Station, TX, USA.
- [62] Boley, B. A., and Barrekette, E. S., 1958, “Thermal Stresses in Curved Beams,” J. Aerosp. Sci., **25**(210), pp. 627–630.
- [63] Tao, Y., 2012, “A Novel Computational Model for Tilting Pad Journal Bearings With Soft Pivot Stiffnesses,” Masters thesis, Texas A&M University, College Station, TX, USA.
- [64] Li, Y., 2015, “A Computational Model for Tiltingpad Journal Bearings With Pad Flexibility,” Masters thesis, Texas A&M University, College Station, TX, USA.
- [65] San Andrés, L., and Li, Y., 2016, “A FE model for Static Load in Tilting Pad Journal Bearings With Pad Flexibility,” Research Progress Report to the Texas A&M University Turbomachinery Research Consortium, TRC-B&C-02-2014, May, College Station, Texas, USA.
- [66] Timoshenko, S., 1925, “Analysis of Bi-Metal Thermostats,” JOSA, **11**(3), pp. 233–255.

**APPENDIX A**  
**THERMAL STRESSES**

This section explains the calculation of thermal stresses and justifies why these stresses do not have a significant role on the deformed shape of the pad. Unlike the strength of materials theory that assumes plane sections must remain plane, the method by Boley and Barrekette [62] calculates the thermal stresses for a one-dimensional temperature distribution  $\bar{T}(r)$  using theory of elasticity with no simplifying assumption. The method in Ref. [62] was applied to an arbitrary curved beam with various slenderness ratios ( $L/D$ ) and temperature boundary conditions. The resultant stresses were compared against those from a commercial FE simulation with a similar radial temperature distribution.

Consider a curved beam of rectangular cross section and with constant properties, under a temperature  $\bar{T}$  varying only in the radial direction. Thermal stress in local radial ( $\sigma_r$ ) and circumferential ( $\sigma_{\hat{\theta}}$ ) from theory of elasticity is [62]

$$\sigma_r = \frac{A_1}{r^2} + \frac{A_2}{R_p^2} (2 \ln (r/R_p) + 1) + 2 \frac{A_3}{R_p^2} - \frac{E\alpha}{r^2} \int_{R_p}^r \bar{T} r dr \quad (\text{A.1a})$$

$$\sigma_{\hat{\theta}} = -\frac{A_1}{r^2} + \frac{A_2}{R_p^2} (2 \ln (r/R_p) + 3) + 2 \frac{A_3}{R_p^2} - E\alpha \left[ \bar{T} - (1/r^2) \int_{R_p}^r \bar{T} r dr \right] \quad (\text{A.1b})$$



Let  $r_0 = R_{back}/R_p$ , in Eq. (A.1) the constants  $N, A_1, A_2, A_3$  are specified as [62]

$$N = 4r_0^2(\ln r_0)^2 - (r_0^2 - 1)^2 \quad (\text{A.2a})$$

$$A_1 = \frac{E\alpha}{N} \left( [2r_0^2 \ln(r_0)[2 \ln(r_0) - 1] + r_0^2 - 1] \int_{R_p}^{R_{back}} \bar{T} r dr - 4r_0^2 \ln(r_0) \int_{R_p}^{R_{back}} \bar{T} r \ln(r/R_p) dr \right) \quad (\text{A.2b})$$

$$A_2 = \frac{E\alpha}{N} \left( [2r_0^2 \ln(r_0) - r_0^2 + 1] \int_{R_p}^{R_{back}} \bar{T} r dr - 2[r_0^2 - 1] \int_{R_p}^{R_{back}} \bar{T} r \ln(r/R_p) dr \right) \quad (\text{A.2c})$$

$$A_3 = \frac{E\alpha}{N} \left( -2r_0^2 [\ln(r_0)]^2 \int_{R_p}^{R_{back}} \bar{T} r dr + [2r_0^2 \ln(r_0) + r_0^2 - 1] \int_{R_p}^{R_{back}} \bar{T} r \ln(r/R_p) dr \right) \quad (\text{A.2d})$$

For the following Figures, the geometry and temperature boundary conditions are the same as those used for Figure 15. The inner radius of the pad ( $R_p$ ) is 0.051 m, the outer radius ( $R_{back}$ ) is 0.07 m. The pad thermal expansion coefficient ( $\alpha$ ) is  $1.3 \times 10^{-5} 1/^\circ\text{C}$ , and temperature boundary conditions for inner and outer surfaces are respectively  $T_p = 80^\circ\text{C}, T_{back} = 72^\circ\text{C}$ .

Figure 43 shows the radial and circumferential stresses due to the temperature gradient across the thickness for the test pad in Ref. [4]. Note that circumferential stresses are much larger than the radial stresses.

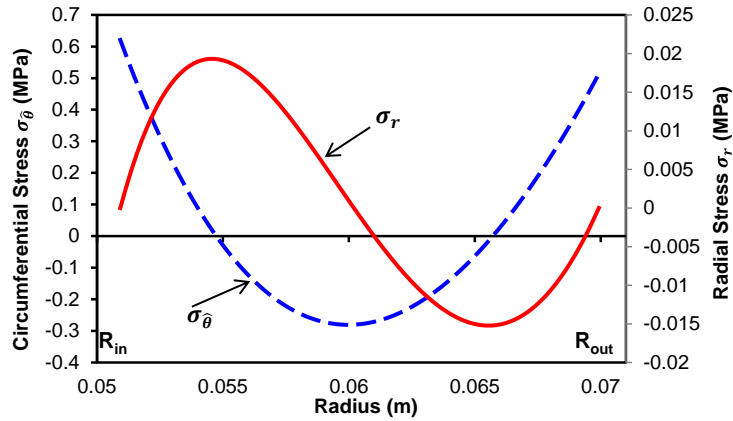


**Figure 43: Thermally induced stress along the circumferential and radial direction for a test pad in Ref. [4].**

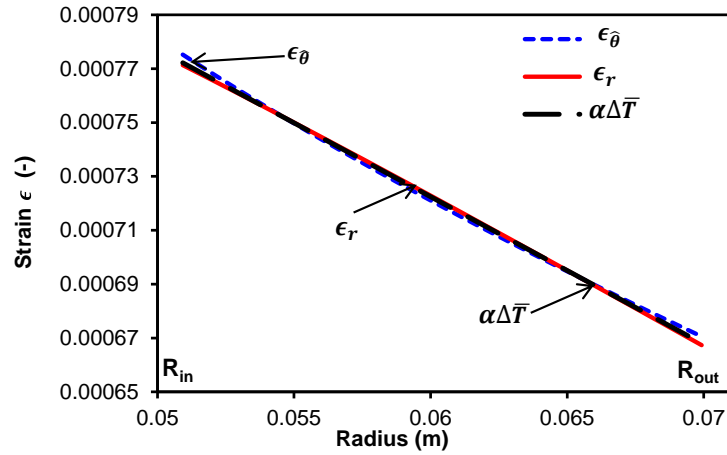
The strains from the generalized Hooke's law read,

$$\epsilon_r = \frac{-\nu \sigma_{\hat{\theta}} + \sigma_r}{E} + \alpha \Delta \bar{T} \quad (\text{A.3a})$$

$$\epsilon_{\hat{\theta}} = \frac{-\nu \sigma_r + \sigma_{\hat{\theta}}}{E} + \alpha \Delta \bar{T} \quad (\text{A.3b})$$

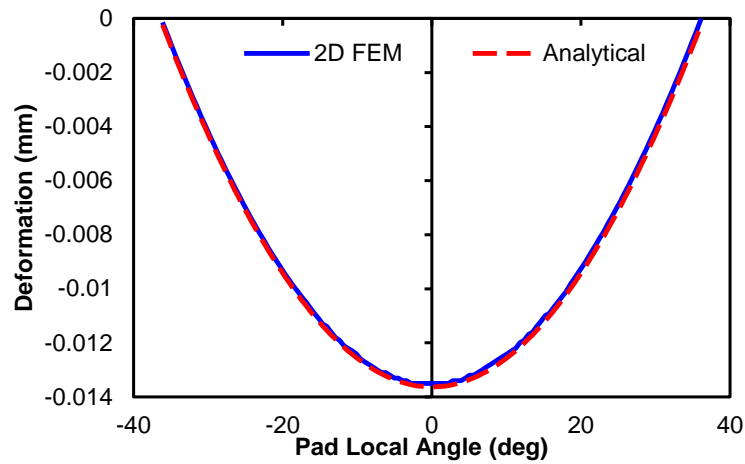
For the steel pads, the elasticity modulus is very large, so the first term on the right hand side of Eq. (A.3) which is due to the thermal stresses is negligible. For the example test bearing in Ref. [4], elasticity modulus ( $E$ ) is  $2.05 \times 10^{11}$ , so on the right hand side, the order of magnitude for the first term is  $10^{-7}$ , while for the second term it is  $10^{-4}$ .

Figure 44 shows that the thermal stress contribution to strains in radial and circumferential directions are negligible, and justifies neglecting the stress terms, allowing the use of the separation of variables method in section 4.5.



**Figure 44: Comparison of thermal strain with and without considering thermally induced stress along the circumferential and radial direction for a test pad in Ref. [4].**

Figure 45 illustrates the pad inner surface deformation along the radial direction versus pad local angle ( $\hat{\theta}$ ), and compares the current method result to 2D FEM. The deformation from the current method is almost identical to the FEM result which includes the thermal stress. This justifies the accuracy of the assumption to neglect the stresses.



**Figure 45: Pad inner surface deformation along the radial direction versus pad local angle ( $\hat{\theta}$ ). Current method results compared to 2D FEM for a test pad in Ref. [4].**

## APPENDIX B

### XLTPJB® GRAPHICAL USER INTERFACE

This appendix briefly explains the XLTPJB’s graphical user interface (Excel GUI) in which the user inputs the bearing geometry, fluid properties, operating conditions, etc., and also runs the Fortran code. After execution, the GUI updates with predicted performance data and charts. Refs. [63, 64] as well as Section 2 of this report provide a detailed explanation on the physical model to obtain the GUI predictions.

Figure 46 shows the “Main TPJB” spreadsheet where the user inputs required parameters for calculating the bearing static and dynamic load performance. After selecting the analysis type and the inputs, user clicks “Run Code” to perform the analysis. The other tabs of the GUI output and visualize additional predictions.

In the “Main TPJB” spreadsheet, each input parameter has an explanation comment in the respective cell. Below lists a brief introduction for each section and their inputs.

- **Bearing geometry:** dimension of the bearing, shaft, and pad; use “Nomenclature” sheet.
- **Fluid Properties:**
  - Viscosity at supply temperature ( $\mu_{sup}$ ): dynamic viscosity of the lubricant at the supply temperature ( $T_{sup}$ ).
  - Viscosity temperature coefficient ( $\alpha_v$ ): used to calculate fluid viscosity as a function of temperature ( $T$ ). Recall,

$$\mu(T) = \mu_{sup} e^{\alpha_v(T_{sup}-T)}$$

Input  $\alpha_v = 0$  for an isoviscous analysis, i.e. constant fluid viscosity.

- Density, specific heat, and thermal conductivity of the lubricant are not a function of pressure or temperature.
  - Ambient pressure is the pressure boundary condition at the axial sides and trailing edge of a pad (default= 0 bar).
  - Supply pressure is the pressure boundary condition at the leading edge of a pad. It is not necessarily as large as the pressure of the flow fed to the bearing.
  - Cavitation pressure is the pressure below which the fluid cavitates and does not generate hydrodynamic pressure (default= 0 bar).
  - Supply temperature ( $T_{sup}$ ): temperature of the fresh lubricant fed to the bearing. The predictions show temperature rise with reference to this temperature.
- **Fluid inertia:** an option to include or to neglect temporal fluid inertia effects in solving the Reynolds equation (default=include).
  - **Frequency analysis option:**
    - Synchronous: the predictions are calculated using excitation displacements synchronous with shaft rotation speed (1X). Using this option, user can get charts with fixed speed and varying load, or fixed load and varying speed (bottom of the sheet).
    - Non-Synchronous: the predictions are calculated for a set of excitation frequencies and the complex stiffness is calculated for the frequency range (bottom of the sheet). Refer to “K-C-M Model” sheet to find the frequency independent rotordynamic coefficients that best fit the predicted complex stiffness.

**XL\_TPJB © Thermo-elasto-hydrodynamic (TEHD) Predictive Tool for Tilting Pad Journal Bearings**  
 Version 1.4, Copyright 2017 by Texas A&M University. All rights reserved. Dr. Luis San Andres, Behzad Abdollahi, Yingkun Li, Yujiao Tao (TRC Project, 2010 - 2017)

**Title:** 4 Pad-LBP-Spherical Seat  
**Code updates:** Color Key & Drop down

**Unit System:** SI

<b>Bearing geometry</b>	
Rotor Diameter	0.1016 m
Bearing Axial Length	0.0610 m
Number of pads on bearing	4
Pad leading edge	9.00 degrees
Pad thickness	0.0190 m

<b>Fluid properties</b>	
Ambient pressure	0.00 bar
Supply pressure	2.00 bar
Cavitation pressure	0.00 bar
Supply temperature	48.9 °C
Viscosity at supply temp.	2.56E-01 centi-Poise
Density	843.5 kg/m3
Specific Heat	2084.7 J/(kg °C)
Thermal conductivity	0.12 W/(m °C)
Viscosity temperature coef.	0.0431 1/°C

<b>Fluid inertia option</b>	Include fluid inertia eff
Frequency analysis type	Synchronous
Shaft speed	1000 RPM

<b>Thermal analysis type</b>	Adiabatic journal - no conduction
Known sump temperature	58 °C
Pad thermal conductivity	51.9 W/(m °C)
Reynolds number in the back	5000
Housing inner Diameter	0.1448 m
Groove convection Coefficient	1750 W/(m2 °C)

<b>Pad inlet taper</b>	
Inlet taper angle	0 degrees
Inlet taper arc length	0 degrees

**Select Analysis Type**  
 X-journal eccentricity ratio: 0.010  
 Y-journal eccentricity ratio: 0.300

**Guess an initial eccentricity relative to cold clearance**  
 Vary load: [dropdown]

<b>Pad option</b>	Equal pads
<b>Analysis Model</b>	THD

<b>Pad Number</b>	1	2	3	4	5
<b>Preload</b>	0.24	0.5	0.5	0.5	0.5
<b>Pivot offset</b>					
<b>Pad arc length</b>		72			
<b>Pad Clearance</b>		1.66E-04			

**Run Code**

<b>Flexibility and thermoelastic deformations</b>	
Pad deformation	Pressure and thermal deformations
Shaft and housing	Fluid shaft rigid housing
Shaft thermal expansion coefficient	23.0 1/°C
Pad thermal expansion coefficient	2.1E-05 1/°C
Housing thermal expansion coefficient	1.3E-05 1/°C
Pad flexibility	Approximate method
Pad's material elastic Modulus	2.07E+11 N/m*2

<b>Pad liner compliance</b>	Account for liner deformation
Elastic modulus	5.20E+10 N/m*2
Poisson's ratio	0.3
Depth (thickness)	2.00E-03 m
Thermal expansion coefficient	2.40E-05 1/°C
Thermal conductivity	27 W/(m °C)

<b>Bearing type</b>	Tilting pad bearing
Pad mass	6.85E-01 kg
Moment of inertia about pivot	4.39E-04 kg m^2
Mass center location	1.31E-02 m
Pad thickness at the pivot	1.90E-02 m

<b>Pivot type</b>	User-defined load/deflection fur	
a0	a1	a2
a3	a4	a5
<b>Material loss factor</b>	0	

<b>Groove lubricant mixing</b>	Hot Oil Carry Over
Hot Oil Carry Over Factor	0.8
Hot Oil Carry Over Rate	0.8

**Fluid inertia eff**: Synchronous

**Shaft speed**: 1000 RPM

**Thermal analysis type**: Adiabatic journal - no conduction

**Known sump temperature**: 58 °C

**Pad thermal conductivity**: 51.9 W/(m °C)

**Reynolds number in the back**: 5000

**Housing inner Diameter**: 0.1448 m

**Groove convection Coefficient**: 1750 W/(m2 °C)

**Pad inlet taper**: Inlet taper angle: 0 degrees, Inlet taper arc length: 0 degrees

**Diagram**: A circular diagram showing a journal with four pads. The pads are numbered 1, 2, 3, and 4 in a clockwise direction starting from the top. A red arrow labeled 'W' points from the journal towards the pads, representing the load. The diagram also shows the coordinate system with X and Y axes and an angle theta.

**Text**: See Tab Nomenclature for definition of all geometrical variables

Figure 46: XLTPJB® graphical user interface (GUI) parameter input form.

- **Thermal analysis type:**

- Heat convection model by Haussen (default=4, refer to “Nomenclature” sheet).
- Calculate journal temperature: the journal temperature equals the average film temperature (default option). Net (total) heat transfer between fluid film and journal is nil.
- Adiabatic journal: no heat transfer to (or from) the journal.
- Known journal temperature.
- Adiabatic bearing: no heat transfer to the pads.
- Known sump temperature (default option): known temperature of discharge oil. Discharge temperature is a good substitute for (difficult to measure) oil temperature in the sump region (between back of a pad and the bearing housing).

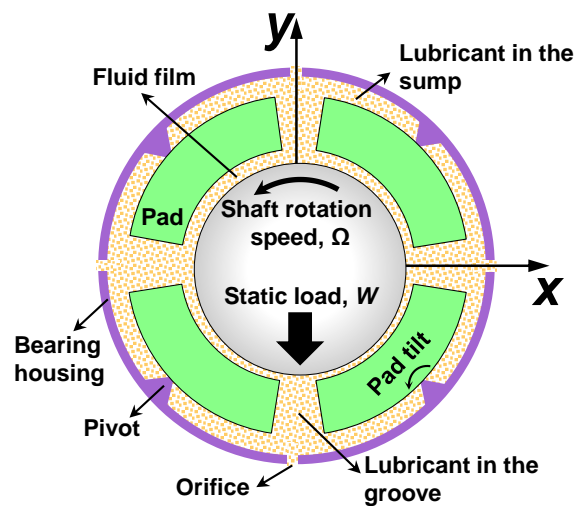


**Figure 47: Schematic view of a 4 pad TPJB and description of its components.**

- Calculate sump temperature ( $T_{sump}$ ): will find the sump temperature by assuming that a portion ( $\epsilon$ ) of the dissipated heat in the bearing is carried away

by the lubricant. Specify this portion in “% of heat carried by the oil” cell (default<0.4).

$$T_{sump} = T_{sup} + \epsilon \frac{\text{power loss}}{\text{total oil flow rate}} \frac{1}{\rho c_p}$$

- Reynolds number in the back and housing inner diameter are used to calculate heat convection coefficients in the sump region behind the pads based on the model in Ref. [45]. The flow in the back is highly turbulent so the input (assumed) Reynolds number must be larger than 2,300 (default=5,000).
- Groove heat convection coefficient: assumed heat convection coefficient at the bearing supply grooves. (default=1,750 W/m<sup>2</sup> °C)
- **Pad inlet taper:** leave blank unless the pads have a taper. If pads are tapered, refer to “Nomenclature” sheet.
- **Select Analysis Type:**
  - Vary load: determines an equilibrium journal eccentricity based on the input load and speed (default option). The user must input an initial guess for eccentricity to start the calculations. If you leave the cells blank and click “Run Code”, the code generates a guess based on the short length bearing model.
  - Vary (journal) eccentricity: determines the performance parameters at the user input shaft eccentricity ( $x, y$ ) components at the bottom of the sheet.
- **Pad option:**
  - Equal pads: enter the pad dimensions for up to 20 identical pads (default).
  - Unequal pads: enter each pad dimensions (up to 6) separately.
- **Bearing type:**



- Tilting pad bearing: frequency independent force coefficients (KCM) require the pad physical inertia parameters (mass, moment of inertia, etc.) in this section (according to the “Nomenclature” sheet).
- Rigid pad bearing: fixed geometry pads with no rotation.

- **Analysis Model:**

- THD (thermo-hydro-dynamic): analysis without including pressure or thermally induced pad surface deformations. The user is encouraged to calculate predictions with this option first, and subsequently conduct an elaborate TEHD analysis.
- TEHD (thermos-elasto-hydro-dynamic): unlocks the pad deformation section (top right of the sheet) and includes the thermoelastic deformation of the bearing elements (pad, shaft, housing).

- **Mechanical flexibility and thermoelastic deformations of pads, shaft, and housing:**

- Pad elastic deformations: select which pad deformations to include in the analysis (pressure induced, thermally induced, or both).
- Shaft and housing: determines the thermal expansion and its direction for shaft and housing. (default option= rigid shaft, rigid housing)
- **Pad flexibility:** pressure induced pad elastic deformation.

- \* 3D FEM: to include the pressure deformations the user needs to generate a pad stiffness matrix (lower\_K.txt) and include it in the same folder as the GUI file. See Ref. [65], page 53, for instructions to obtain the lower triangular stiffness matrix.

- \* Approximate method: calculates the pressure induced deformation of the pad based on a curved beam model [64]. This option does not require an additional (input) file.
- **Thermal induced deformation only:** does not require any additional files. However, the thermal analysis option cannot be “adiabatic pads” since the deformation is a function of the radial temperature field in the pads.
- **Pivot type:** Refer to “Nomenclature” sheet for details on pivot option input from Hertz contact stress theory. Highly recommended to use user-defined load deflection option (when available).
- **Groove lubricant (thermal) mixing:**
  - Hot oil carry over: uses a simple empirical parameter between 0 and 1 to specify the amount of upstream hot oil that reaches downstream pad (default option, typically  $\approx 0.8$ ).
  - Improved model<sup>21</sup>: use only when the total supply flow rate is known. The mixing coefficient is about 0.5 to 0.8 for evacuated bearings with direct lubrication arrangements such as LEG, spray bar, etc. It is lower ( $\approx 0.4$ ) for flooded conventional bearings.
- **Pad liner compliance:** if implemented, it accounts for the thermoelastic deformations of pad’s inner surface liner such as Babbitt (white metal), PTFE, PEEK, etc (default= neglect). The user inputs the material properties and depth (thickness) of the liner.

Figure 48 shows geometry parameters of a pad and a liner.  $E$  is the material elastic modulus and  $\alpha$  is the thermal expansion coefficient. Below, subscript 1 refers to the liner layer,

---

<sup>21</sup>Refer to section 4.4 in this report for description of the improved model.

and subscript 2 refers to the pad metal backing.

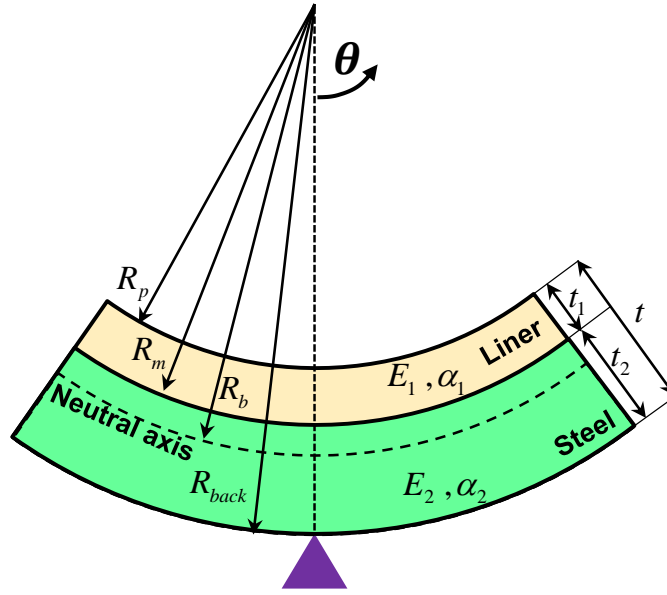


Figure 48: Geometry and material characteristics of a pad with a liner.

Ref. [64] reports the radial mechanical deformation ( $u(\theta)$ ) for a bimetallic curved beam under a uniform pressure  $\bar{P}$  as,

$$u(\theta) = \frac{6\bar{P}LR_{eq}^4}{E_{eq}(Lt^3)} [(\cos \theta - 2) \cos \theta + 1] \quad (\text{B.1})$$

where,

$$E_{eq} = \frac{E_1 t_1 \left(\frac{t_1}{2} - R_b\right) + E_2 t_2 \left(\frac{t_2}{2} - R_b\right)}{t \left(\frac{t}{2} - R_{eq}\right)} \quad (\text{B.2})$$

$$R_{eq} = \frac{t}{\ln(R_{back}/R_p)} \quad (\text{B.3})$$

$$R_b = \frac{E_1 t_1 + E_2 t_2}{E_1 \ln(R_m/R_p) + E_2 \ln(R_{back}/R_m)} \quad (\text{B.4})$$

Timoshenko [66] calculates the curvature (radius) of thermal warping for a bi-material

beam subject to a uniform temperature rise  $\Delta T$  as,

$$\kappa = t \frac{\left( 3(1+m)^2 + (mn+1) \left( m^2 + \frac{1}{mn} \right) \right)}{6(\alpha_1 - \alpha_2)(\Delta T)(1+m)^2} \quad (\text{B.5})$$

where  $m = t_2/t_1$  and  $n = E_2/E_1$ . The curvature ( $\kappa$ ) along with additional thermal expansion of the liner material is added to the pad surface thermally induced deformation.